1-1-2013

Multi-Physicochemical Modeling of Solid Oxide Fuel Cells and Electrolyzer Cells

YUANYUAN XIE
University of South Carolina

Multi-Physicochemical Modeling of Solid Oxide Fuel Cells and Electrolyzer Cells

by

Yuanyuan Xie

Bachelor of Mechanical Engineering
Hefei University of Technology, 2005

Master of Mechanical Engineering
University of Science and Technology of China, 2008

Submitted in Partial Fulfillment of the Requirements

For the Degree of Doctor of Philosophy in

Mechanical Engineering

College of Engineering and Computing

University of South Carolina

2013

Accepted by:

Xingjian Xue, Major Professor

Kenneth Reifsnider, Committee Member

Tony Reynolds, Committee Member

Andreas Heyden, Committee Member

Lacy Ford, Vice Provost and Dean of Graduate Studies

ACKNOWLEDGEMENTS

I wish to express my deep gratitude to my advisor Prof. Xingjian Xue, for offering me this opportunity and his continuous and patient guidance throughout my graduate studies. He helped me whenever I encountered difficulties, and encouraged me with much kindness throughout my studies. I also would like to extend gratitude to my committee members, Prof. Ken Reifsnider, Prof. Tony Reynolds, and Prof. Andreas Heyden for their valuable suggestions and important support.

Furthermore, I am thankful to my lab-mates, for their constructive discussions and peer interactions as well as the precious friendship. I am also grateful to my friends in the Department of Mechanical Engineering, who gave me a lot of help when I first came to the university.

Last but not least, I would like to acknowledge my parent who constantly care about me and always concern my problems. Without their endless love and encouragement, I would not have completed this study.

ABSTRACT

Multi-physicochemical models are developed for solid oxide fuel cells and electrolysis cells. The models describe the complicated transport processes of charge (electron/ion) conservation, mass/species conservation, momentum conservation, and energy conservation. Transport processes are coherently coupled with chemical reforming processes, surface elementary reaction processes, as well as electro-oxidation processes of both hydrogen and carbon monoxide. The models are validated with experimental data and utilized for fundamental mechanism studies of SOFCs fueled with different type of fuels, such as hydrogen, hydrocarbon, e.g., methane, H_2S, and their mixtures. The fundamental mechanisms associated with syngas generation using electrolysis cell are also extensively investigated using the developed model.

The simulation results of SOFCs show that that the Nernst potential E_{H2} shows a strong correlation with the cell voltage, increasing with increasing the cell voltage. The E_{CO} shows a weak dependence on the cell voltage, especially at the anode/electrolyte interface. Suitable H_2S content in CH_4 fuel is beneficial to improve the reforming process of CH_4 and SOFC electrochemical performance particularly H_2-H_2O electro-oxidation process. The adsorbed surface species are very sensitive to the variations of the supplied hydrogen and oxygen as well as the cell voltage. To mitigate potential surface carbon

deposition, one may: (1) suitably increase H_2O content in the fuel; (2) reduce the content of CH_4, CO, CO_2 in the supplied fuel; (3) increase the operating temperature; (4) increase the cell operating current; (5) improve exchange current density of electrodes.

The simulation results of electrolyzer cell indicate that: (1) the intensity of surface electrolysis processes appears to be strong at the H_2 electrode/electrolyte interface even though the composite electrode is assumed; (2) the surface electrolysis processes of CO_2 and H_2O are pretty much independent with each other; (3) the carbon coking effect is mainly determined by the fraction of CO_2 in the H_2 electrode; (4) high cell voltage conditions may cause the enhancement of the surface coverage of C(s) and the deposition of carbon on the surface of Ni catalyst; (5) high operating temperature may effectively improve adsorption/desorption rate, and enhance surface electrolysis process as well as potentially mitigate carbon deposition on Ni surface.

TABLE OF CONTENTS

LIST OF TABLES

LIST OF FIGURES

LIST OF SYMBOLS

A	The Arrhenius parameter for the rate constants
c_i	Concentration (mol/m^3)
$D_{m,k}$	Ordinary diffusion coefficient (m^2/s)
D_{Kn}^{eff}	Knudsen diffusion coefficient (m^2/s)
D_i^{surf}	Surface diffusivity of specie i (m^2/s)
D^T	Thermal diffusion coefficient($kg/m\,s$)
E^0	The standard potential(V)
E^{act}	The thermal activation energy(kJ/mol)
F	Faraday's constant ($96{,}485\ C/mol$)
G	The Gibbs free energy(J)
i_F	Faradic current density (A/m^2)
k_f, k_b	The forward and backward reaction rate coefficients
K	Permeability
K_{eq}	The equivalent thermal conductivity($W/m\,K$)
M_i	Molecular weight of species i
m, n	The stoichiometric coefficients
p_i	The partial pressure of specie i
Q_H	The heat source term(J/mol)

r_i	The rate of elementary reaction i
R	Universal gas constant (8.314 J/K mol)
R_i	Mass conservation source term of species i
R_n	The net reaction rate
l_{TPB}	Three phase boundary length per unit volume (m/m^3)
T	Temperature (K)
V	Cell voltage (V)
x_i	Molar fraction of specie i
z	The number of electrons
Γ	The available surface site density(mol/cm^2)
η_{act}	The activation overpotential (V)
θ_i	Surface coverage of adsorbed specie i
ρ	Density(kg/m^3)
$\sigma_{e,i}$	Electronic/ionic charge conductivity (S/m)
σ_i^{surf}	The number of surface sites occupied by specie i
w_i	Mass fraction of species i
μ	Viscosity
ε	Porosity
τ	Tortuosity
An	anode
Ca	cathode
El	electrolyte

Cl	channel
eff	effective
ohm	Ohmic
chem	Electrochemical/chemical

CHAPTER 1

INTRODUCTION

1.1 GENERAL INTRODUCTION OF ENERGY CRISIS AND FUEL CELLS

The rapid economic growth has triggered excessive and accelerated use of fossil fuels, especially coal, oil and gas, leading to a global energy crisis [1,2]. The increasing demand for energy has raised two significant issues. On one hand, the naturally existing fossil fuels will be depleting, implying that the present power generation techniques from the fossil fuels are not sustainable. On the other hand, carbon dioxide emission generated from the combustion of fossil fuels has placed enormous pressure on the environment, which is regarded as the key factor influencing the climate and related environmental problems. Obviously, meeting the energy needs while maintaining the quality of the environment will need significant advancement in new energy technologies. Among the power generation technologies, fuel cells have been recognized as the most efficient and environmentally benign energy conversion technology [3,4].

In literature, several types of fuel cells have been studied, including alkaline fuel cell (AFC)[5,6,7], proton exchange membrane fuel cell (PEMFC)[8,9,10], direct methanol fuel cell (DMFC)[11,12,13], molten carbonate fuel cell (MCFC)[14,15,16], phosphoric acid fuel cell (PAFC)[17,18,19], and solid oxide fuel cell (SOFC)[20,21,22]. The features of these fuel

cells are characterized by the utilized electrolyte and catalysts, the operating temperatures, and different fuels. Table 1.1 summarizes the major characteristics of these fuel cells. Because of the characteristic differences, the practical applications may favor one type of fuel cell over another. The SOFC has many key advantages that make it stand out in the field of fuel cells, such as very high energy conversion efficiency, fuel flexibility, design flexibility, etc.

Table 1.1 Characteristic comparison of different type of fuel cells

	PEMFC	AFC	PAFC	MCFC	SOFC
Electrolyte	Polymer	Potassium hydroxide	Phosphoric acid	Molten carbonate	Ceramics
Conductor	H^+	OH^-	H^+	CO_3^{2-}	O^{2-}/H^+
Catalyst	Platinum	Platinum	Platinum	Electrode materials	Nickel, electrode ceramics
Operating temperature (^oC)	40-80	65-220	150-205	650	500-900
Fuel	Pure hydrogen	Pure hydrogen	Hydrogen	Fuel flexible	Fuel flexible

1.2 SOLID OXIDE FUEL CELL

The fundamental structure of SOFCs is a positive electrode-electrolyte-negative electrolyte tri-layer assembly, in which the dense electrolyte is sandwiched by porous electrode on either side. Figure 1.1 shows a schematic illustration of SOFC structure and the associated basic operating principle. Fuel arrives at the anode, where it is oxidized, thereby releasing electrons to the external circuit. On the other side of the fuel cell, oxidant is fed to the cathode, where it is reduced to oxygen ions by accepting electrons

from the external circuit. The electrolyte conducts the oxygen ions from the cathode to the anode, allowing the electrochemical reactions to occur continuously at both electrodes. The flow of electrons in the external circuit provides useful power.

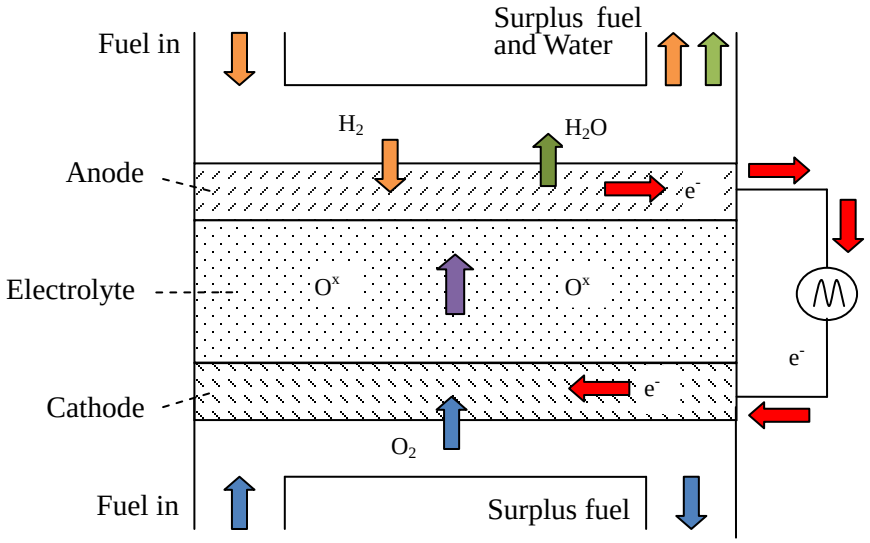

Figure 1.1 Scheme of solid oxide fuel cell

The SOFC technology has successfully demonstrated the capability of fuel flexibility, which can operate on not only hydrogen but also hydrocarbon fuels[23]. The high temperature operating condition together with hydrocarbon fuel may lead to very complicated reforming process in the anode. The reforming process in combination with electrochemical oxidation processes and thermal-fluid transport processes represent very complicated multi-physics transport processes in SOFCs. In order to fundamentally understand the multi-physics processes in SOFCs, significant efforts have been put into experimental investigations[24-28]. Modeling approach, as an important complementary to experiment, may provide significant advantages in this regard and has been extensively employed as a cost-effective technique in SOFC research.

1.3 MATHEMATICAL MODELING OF SOFC

In literature, SOFC models have been developed at different levels for different purposes, such as system-level modeling[29-31], stack-level modeling[32-34], and single cell modeling[35-37]. The system-level model is to study the system performance and design, in which the SOFC stack is embedded in the system. Usually, the major characteristic behavior is considered, e.g., input-output performance while the details of internal processes in the stack are generally neglected. A stack is formed by packing a few of single cells together. To study the details of transport processes in the stack while keeping the computation tractable, the stack –level model is developed by neglecting certain details of the involved single cells. The single cells have been widely used to investigate the fundamentals of SOFCs. Because the computational domain is relatively small, it is possible to consider many details in single cell models. Typically the cell model is developed based on computational fluid dynamics (CFD) multi-physics approach[38]. The fundamental processes involved in CFD multi-physics model include charge conservation, mass/species conservation, momentum conservation, and energy conservation. These processes are coupled together within porous electrodes through Butler-Volmer equation. At the early stages, the models only consider the charge conservation and fuel/gas diffusion processes in the porous electrodes[39,40], the momentum and energy conservations are neglected by assuming isothermal conditions. Later on, the momentum conservation and energy conservation are included in single cell models[41,42]. To better determine the boundary conditions, the thermal-fluid transport

processes in the test stand are also considered in the cell models[41].

SOFCs are fuel flexible, which can operate on not only hydrogen but also hydrocarbon fuel cells. The typical anode materials are nickel cermet. When hydrocarbons are used as the fuels for SOFCs, very complicated reforming processes exist in the porous anode due to the catalytic property of nickel. Some modeling work incorporate the reforming processes into the CFD model with different assumptions[43,44]. Usually, reforming processes are considered under bulk sense without incorporating the specific role of nickel catalyst.

The electrodes are critical components of SOFCs and consist of void phase solid phase. The void phase allows fuel/gas diffusion. Accordingly there are complicated gas/solid interactions in porous electrodes, such as surface adsorption/desorption processes and surface chemical reaction processes as well as electrochemical oxidation processes. Recent advancements in SOFC investigations involve the detailed identification of these processes using patterned anode electrode designs[45], where the triple boundary is carefully controlled. This provides an experimental base for SOFC model development with elementary reactions. The incorporation of elementary reactions with CFD based SOFC model may further improve the fidelity of SOFC model development for fundamental mechanism understanding [46].

1.4 OPEN TOPICS AND THE OBJECTIVES OF THIS DISSERTATION

Despite of the significant progress in SOFC modeling studies, there are still

some issues that can be improved upon. Fuel cell performance strongly depends on the electrochemical reactions. In principle, many electrochemical reactions could take place simultaneously at the triple phase boundaries. For example, in methane fueled SOFCs, the electrochemical oxidation reactions may occur through hydrogen oxidation process and carbon monoxide oxidation process[47]. The present studies usually neglect the CO oxidation process by making simplified assumptions[48,49], in which it could play an important role on affecting surface elementary reactions and other transport processes and ultimately the electrochemical performance of SOFCs.

The widely used anode materials are nickel cermet, in which the nickel catalyst is mixed with electrolyte materials. When hydrocarbon is used as the fuel for SOFCs, the deposition of carbon on the surface of catalyst nickel could occur, deactivating the catalytic function of nickel catalyst. With the elementary reactions coupling with the CFD-based SOFC model, it is quite feasible to study carbon deposition issues and the corresponding mitigation strategy. It has been found that a SOFC using the direct oxidation of syngas fuel is more powerful than using pure hydrogen fuel, and shows higher performance in terms of electrical efficiency[23]. Obviously it is worth performing further fundamental mechanism studies through the modeling approach.

Since a significant amount of H_2S is produced as an industrial by-product in the fossil fuel refining process, particularly recent years in the U.S.[50], the direct H_2S-fueled SOFC may provide a promising alternative to neutralize this environmental pollutant. Nevertheless, when H_2S is used as the fuel, sulfur poisoning issue could occur,

blocking the active sites of the catalyst (nickel) surface[51]. To investigate the associated fundamental mechanisms, significant efforts have been put into the study of direct H_2S fueled SOFCs[52-54]. Most of these researches are experimental in nature. Since very complicated chemical/electrochemical processes are involved in direct H_2S fueled SOFCs, it is worth to resorting the modeling techniques for this purpose.

The hydrocarbon fuels such as natural gas, methane-rich fuels derived from gasified biomass generally have many contaminants, typically sulfur- and carbon-containing compounds[55]. These contaminants may lead to sulfur poisoning and carbon deposition of nickel catalyst, and deactivate the function of nickel cermet anode. The issues of carbon deposition and sulfur poison effects on nickel-based anodes are usually studied individually. In order to simulate the contaminants involved in practical hydrocarbon fuels, the model of SOFCs fueled with mixture of hydrocarbon and H_2S is needed.

The potential fossil fuel crisis and climate changes raise the need to develop renewable and clean energy technology[2]. The co-electrolysis of H_2O and CO_2 using the inverse process of solid oxide fuel cell (SOFC) is able to produce synthetic gas in a clean and efficient way[56,57]. Such a technique has been demonstrated experimentally and attracted much interest recently. There have been recent studies on numerical modeling of solid oxide electrolysis cell (SOEC), including H_2O electrolysis[58-60] and CO_2 electrolysis[61-63]. Usually such models are a global type of kinetic models, where the concentrations of bulk gas species are used for Butler-Volmer equation to couple

electrochemical reactions with transport process in porous electrodes. As a consequence, the adsorbed species on electrode surface and surface reactions are neglected. To overcome this issue, the elementary kinetic modeling approach is recently investigated[64,65] to describe the adsorption/desorption processes and the detailed surface chemistry via individual reaction steps. While elementary kinetic model is able to provide more precise electrochemical charge-transfer calculation, such model is limited to describe the reaction process at one individual point on the electrode surface. Currently there is a lack of coherent integration between macro-scale transport processes and local elementary kinetic reactions.

The objective of this dissertation is to develop multi-physicochemical models for solid oxide fuel cells and electrolyzer cells to address above issues. In particular, the multi-physicochemical transport processes in SOFCs fueled with different type of fuels are systematically investigated, including hydrogen, hydrocarbons, H_2S, and their mixtures. The multi-physicochemical processes associated SOECs used for synthetic gas generation are studied.

1.5 DISSERTATION ORGANIZATION

The study of this dissertation is divided into eight chapters. The transport mechanisms and the chemical/electrochemical processes of SOFC are discussed in chapter 2. In chapters 3-5, the multi-physical SOFC modeling based on global reaction mechanisms of H_2S and CH_4 are developed, where the cell performance, the operating

condition effects, as well as the interaction between H_2S and CH_4 are investigated. The detailed elementary reaction kinetics modeling of SOFC are presented in chapters 6-8, where both the hydrogen/methane fueled SOFCs and the electrolysis cell are modeled and studied, and the connection between surface chemistry and global cell performance are investigated by the considering the coherently coupling of micro-level elementary reactions and cell-level transport processes. In the last chapter, the contribution of this research and future work are summarized.

CHAPTER 2

TRANSPORT MECHANISMS AND CHEMICAL PROCESSES IN SOFC

The transport processes inside the SOFCs are usually very complicate, which include fuel/gas transport in fuel supply tubes and porous electrodes, charge transport through material backbone, as well as the heat transfer. These transport processes are strongly interacted with each other, and moreover, are all coherently coupled with various heterogeneous chemical/electrochemical reactions within porous electrodes. To elucidate these transport and reaction mechanisms, the theory and governing equations are presented in the following.

2.1 CHARGE TRANSPORT

In principle, SOFC operating is based on the balance between the flow of electronic charges through external circuit and the flow of the ionic charge through the electrolyte. The charge transport process within SOFC has three control domains: anode, electrolyte and cathode. In the electrodes(anode and cathode), electrons and ions are charge carrying particles, while in the electrolyte layer electron flow is blocked and only ions are allowed to migrate through. The generic Ohm's law is usually utilized to formulate these processes. In the electrodes, the governing equation is:

$$-\nabla \bullet (\sigma_n^{eff} \nabla V_n) = \pm i_F \,, \quad n = e, i \tag{2.1}$$

where, V_n is the potential; σ_n^{eff} is the effective conductivity; e / i represents electronic/ionic field respectively; $\pm i_F$ is the faradic current in the electrodes, and $+i_F$ stands for electronic current while $-i_F$ denotes ionic current. Considering the composite electrodes, the conductivities are further calculated as $\sigma_e^{eff} = \phi(\frac{1-\varepsilon}{\tau})\sigma_e$ and $\sigma_i^{eff} = (1-\phi)(\frac{1-\varepsilon}{\tau})\sigma_i$, where ε is the porosity, τ the tortuosity, and ϕ the volume fraction of electronic conducting phase in the electrode. Since no exchange current exists in the electrolyte layer, the governing equation of this domain is built as:

$$-\nabla \bullet (\sigma_{ele} \nabla V_i) = 0 \tag{2.2}$$

where, σ_{ele} is the ionic conductivity of the electrolyte layer.

2.2 MASS TRANSPORT

The mass transport processes of SOFC includes various fuel gas species, integrated with the chemical reforming reactions at the solid active surface. Due to the porous structure of electrodes, the mass transfer is dominated by the diffusion process, while the electrolyte layer can be assumed to be impermeable.

The simplest diffusion model is Fick's law, which is widely applied to describe the transport of components through the gas phase and within porous media. The general extended form of this model takes into account diffusion and convection transport processes, which is formulated by,

$$\frac{\partial \varphi}{\partial t} = -\nabla \cdot J_i + R_i, \quad \varphi = \frac{\varepsilon P x_i}{RT} \tag{2.3}$$

$$J_i = \frac{1}{RT}(-D_i^{eff} \nabla (x_i P) + \frac{K_0 x_i P}{\mu} \nabla P) \tag{2.4}$$

here, ε is the porosity; J_i represents the rate of mass transport into porous media; R_i is

the rate of the chemical reaction; P is the pressure; x_i is the molar fraction of species i; K_0 is the permeability coefficient; μ is the viscosity of the gas species; D_i^{eff} is the effective diffusivity of species i, and can be typically divided into two diffusion mechanisms of molecular diffusion and Knudsen diffusion,

$$D_i^{eff} = (\frac{1}{D_{im}^{eff}} + \frac{1}{D_{ik}^{eff}})^{-1} \tag{2.5}$$

where, D_{im}^{eff} and D_{ik}^{eff} are the effective molecular diffusion coefficient and Knudsen diffusion coefficient respectively.

Accordingly, Fick's law is only applicable for single or binary fuel conditions. For multi-species fuel system (e.g. hydrocarbon fuels), the Stefan-Maxwell model is employed to formulate the transport processes in both fuel/gas supply tubes and porous electrodes. The governing equations are given as,

$$\nabla \bullet J_i + \rho v \bullet \nabla w_i = R_i \tag{2.6}$$

$$J_i = -\rho w_i \sum_k D_{i,k}^{eff} [\nabla x_k + (x_k - w_k) \frac{\nabla p}{p}] \tag{2.7}$$

where, the subscript i and k stand for different gas species; w is the mass fraction; R_i is the rate of species i generation; x_k is the mole fraction of species k; D_{ik}^{eff} is the effective diffusion coefficient and is determined by combining molecular diffusion in large pores(Empirical relation by Fuller, Schettler and Giddings[66]) and Knudsen diffusion in small pores comparable to the molecular mean-free path,

$$D_{i,k}^{eff} = (\frac{\tau}{\varepsilon D_{i,k}} + \frac{1}{D_{Kn}})^{-1} \tag{2.8}$$

$$D_{i,k} = 10^{-3} \frac{T^{1.75} (1/M_i + 1/M_k)^{0.5}}{p[(\sum_j V_{ji})^{1/3} + (\sum_j V_{jk})^{1/3}]^2}, \qquad D_{Kn} = \frac{d_{pr}}{3} \sqrt{\frac{8\kappa NT}{\pi M}} \tag{2.9}$$

where, M_i and M_k are molecular weights of species i and k respectively; T is the temperature in Kelvin; V_{ji} and V_{jk} are the volumes of parts of the molecule i and can be referred in[66]; d_{pr} is the average pore diameter.

2.3 MOMENTUM TRANSPORT

The flow field in fuel cells may be classified by three parts: fuel chamber, inlet/outlet fuel channels and porous electrodes. In the fuel chamber and channels, the incompressible laminar flow is usually assumed for fuel gases due to the relatively low velocities, of which the physics is formulated by the Navier-Stokes equations,

$$\nabla p + \rho(v \bullet \nabla)v = \nabla \bullet [\mu(\nabla v + (\nabla v)^T) - \frac{2}{3}\mu(\nabla \bullet v)\mathrm{I}] \tag{2.10}$$

$$\nabla \bullet (pv) = 0 \tag{2.11}$$

where, p is the pressure, μ is the viscosity of fuel gas, and I is the identity matrix. In the porous electrodes, due to the permeability variation, the Darcy's law is utilized to express the fuel flow. However, the traditional form of Darcy's law doesn't consider the solid boundary effect. Therefore, the Brinkman term is introduced and added to the classical Darcy equation,

$$\frac{\mu}{K}v = -\nabla p + \frac{1}{\varepsilon}\nabla \bullet \left\{\mu[\nabla v + (\nabla v)^T] - \frac{2}{3}\mu(\nabla \bullet v)I\right\} \tag{2.12}$$

$$K = \frac{\varepsilon^3 {d_p}^2}{150(1-\varepsilon)^2} \tag{2.13}$$

where, K is the permeability, d_p is the average particle diameter of porous electrode.

2.4 HEAT TRANSPORT

The heat transfer processes inside SOFCs consists of various aspects including

conductive heat through solid porous structures, convective/radiative heat transfer between the solid matrix surfaces and the fuel gas steams, and the heat generation due to the chemical/electrochemical reactions. In general, the local temperature equilibrium is assumed in the porous electrodes since plenty of experiment works proved that the temperature difference between the gas phases and the solid matrix is always negligible under most operating conditions. The governing equation can be formulated by,

$$\rho c_p v \bullet \nabla T - \nabla \bullet (k_e \nabla T) = Q_h \tag{2.14}$$

where, c_p is the heat capacity; v is the flow velocity; k_e is the effective volumetric thermal conductivity; Q_h is the general heat source term. Since the electrolyte layer is impermeable, the above governing equation can be reduced to pure heat conduction in this area.

The effective value of the capacity and thermal conductivity in porous electrodes can be specified as,

$$c_p = \beta c_{p,l} + (1-\beta) c_{p,s} \tag{2.15}$$

$$k_e = \beta k_l + (1-\beta) k_s \tag{2.16}$$

where, β is the volume fraction of gas phase, l and s are the gas phases and solid phases respectively. The specific heat capacity for each gas species is calculated as,

$$c_{p,l} = \sum_i x_i c_{p,i} \tag{2.17}$$

$$c_{p,s} = \sum_{n=1}^{n} a_n \left(\frac{T}{1000}\right)^n \tag{2.18}$$

where a_n is the species dependent parameter and n stands for the number of parameters

involved in the specific heat calculation. The thermal conductivity for each species of the gas phase, as well as for the gas mixture, is formulate as,

$$k_l = \sum_i x_i c_i \tag{2.19}$$

$$k_s = 0.01 \sum_{n=1}^{n} c_k \left(\frac{T}{1000}\right)^n \tag{2.20}$$

where c_k is the species dependent parameter and n stands for the number of parameters in the thermal conductivity evaluation.

The general heat sources consists of the heat consumption/generation of internal reforming reactions $Q_{h,r}$, the heat production due to the activation and concentration polarizations $Q_{h,ac}$, and the ohmic resistance induced heat generation $Q_{h,ohm}$ [67],

$$Q_{h,r} = r \cdot \Delta H \tag{2.21}$$

$$Q_{h,ac} = -(\eta_{act} + \eta_{con}) \cdot i \cdot AV_e \tag{2.22}$$

$$Q_{h,ohm} = i^2 / \sigma \tag{2.23}$$

where, r is the reaction rate (in mol/m3 s); ΔH the enthalpy change of the reforming reactions; i is the ion current density; η_{act} the activation polarization; η_{con} is the concentration polarization; AV is the electrochemical active area to volume ratio; σ is the conductivity.

2.5 CHEMICAL/ELECTROCHEMICAL REACTION PROCESSES

The internal reforming processes inside SOFC porous electrodes depend on both type of fuel and operating conditions, especially in high molecular weight hydrocarbon fuel applied anode electrode[68]. Generally, the operating process is through the catalytic

reforming reactions, hydrocarbon fuel species can be converted to a mixture of hydrogen, carbon monoxide/dioxide or other species, then hydrogen/carbon monoxide further takes electrochemical reactions with oxygen ions conducted from electrolyte layer, and generate steam/carbon dioxide as well as the heat. The global reaction kinetics and elementary reaction kinetics are usually employed to mathematically describe these processes.

The global reaction kinetics is based on the simplified global reforming reactions developed in open literatures, and the reaction rates of these reforming process are calculated by the classical Arrhenius equation[69],

$$k_f = AT^n \exp(\frac{-E_f^{act}}{RT}), \quad k_b = AT^n \exp(\frac{-E_b^{act}}{RT}) \tag{2.24}$$

where, k_f and k_b are the forward and backward reaction rates respectively; A, n and E^{act} are the Arrhenius parameters corresponding to different global reactions; R is the gas constant; T is the reaction temperature. The chemical equilibrium state of species n can be determined by the net reaction rate R_n:

$$R_n = \sum_n v_n (k_f \prod_i [c_i^{Ra}]^{n_i} - k_b \prod_j [c_j^{Pu}]^{m_j}) \tag{2.25}$$

where, v_n is the pre-factor for elementary reaction; c_i^{Ra} and c_j^{Pu} are the concentrations of reactant and product respectively while n_i and m_j are the corresponding stoichiometric factors.

The elementary reaction kinetics is strongly connected to the heterogeneous catalysis and the surface chemistry. Since the information about surface coverage are not available in global approach, the detailed elementary reaction model can provide more

precise simulations of surface chemical processes and are recently developed by Bessler et al.[69-71] and Kee et al.[72]. Generally, two types of processes are included in elementary kinetics model: the adsorption/desorption process and surface diffusion/reaction process. It is recognized that fuel species are first adsorbed on the electrode surface under catalytic function, then take surface diffusion and reaction processes. The reaction rates of adsorption/desorption processes and surface reactions can be determined by the Arrhenius equations. As for the surface diffusion process, according to the mean field approach[73], it can be described by,

$$\frac{\sigma_i^{surf}}{\Gamma} R_n = -\nabla \bullet (D_i^{suf} \nabla \theta_i) \tag{2.26}$$

where, σ_i^{surf} is the number of surface sites occupied by species i; D_i^{suf} is the surface diffusivity of species i ($D_i^{suf} = D_i^0 \exp(-E_i^{act} / RT)$); R_n is the net reaction rate for species n; the concentration of surface species i is normalized by the total available surface sites Γ, yielding the surface coverage ($\theta = c_i \sigma_i^{surf} / \Gamma$), a dimensionless parameter.

At the triple-phase boundary, charge transfer reactions take place between the adsorbed species and oxygen ions conducted from the electrolyte layer. Due to that many charge transfer pathways may exist simultaneously[64], and the identification of kinetic steps of charge transfer is still difficult from experiments. The rate-dominating charge transfer steps are assumed to simulate the electrochemical processes. For example, the H_2-H_2O electro-oxidation pathway can be determined by,

$$\eta_{H_2} = \frac{\Delta G}{zF} + \frac{RT}{2F} \ln\left(\frac{p_{H_2} p_{O_2}^{0.5}}{p_{H_2O}}\right) \tag{2.27}$$

$$i_{an}^{H_2} = z \cdot F \cdot l_{TPB} \cdot i_{0,an}^{H_2} [\exp(\frac{\alpha z F}{RT}(\eta - \eta_{H_2})) - \exp(-\frac{(1-\alpha) z F}{RT}(\eta - \eta_{H_2}))] \quad (2.28)$$

where, ΔG is the Gibbs free energy of the reaction, z is the number of electrons, p is the partial pressure; l_{TPB} is the three phase boundary length per unit volume, $i_{0,an}^{H_2}$ is the exchange current density and can be formulated as[74],

$$i_{0,an}^{H_2} = i_{H_2}^{*} \frac{(p_{H_2} / p_{H_2}^{*})^{0.25} (p_{H_2O})^{0.75}}{1 + (p_{H_2} / p_{H_2}^{*})^{0.5}} \quad (2.29)$$

where, $p_{H_2}^{*}$ is about 0.7atm; $i_{H_2}^{*}$ is the empirical constant.

CHAPTER 3

MODELING OF DIRECT H_2S FUELED SOLID OXIDE FUEL CELLS WITH GLOBAL REFORMING CHEMICAL KINETICS

3.1 INTRODUCTION

Solid oxide fuel cells (SOFCs) show great fuel flexibility and can utilize H_2, CO, H_2S, hydrocarbons, or their mixture to generate electrical energy[75,76]. Since a significant amount of H_2S is produced as an industrial by-product in the fossil fuel refining process, particularly recent year in the U.S.[50,77], the direct H_2S-fueled SOFC may provide a promising alternative to neutralize this environmental pollutant. Nevertheless, when H_2S is used as the fuel, sulfur poisoning issue could occur, blocking the active sites of the catalyst (nickel) surface[51,78,79]. To investigate the associated fundamental mechanisms, significant efforts have been put into the study of direct H_2S fueled SOFCs [78-81]. Most of these researches are experimental in nature. Since very complicated chemical/electrochemical processes are involved in direct H_2S fueled SOFCs, the modeling technique is also resorted for this purpose.

The modeling of direct H_2S fueled SOFCs is still at its early stages[77,80,81], where the multi-physics transport processes are considered [77], but the heterogeneous chemical reactions are usually neglected. Theoretically, under relatively high operating temperature,

the H_2S may dissociate into H_2 and S_2 or react with the steam to produce SO_2 and H_2 [82,83]. The generated H_2 may further experience electro-oxidation process with oxygen ions conducted from the cathode side. These chemical/electrochemical reaction processes are affected by the operating conditions, which in turn influence the local chemical balance and SOFC performance. Therefore, in order to improve the fundamental mechanism understanding of direct H_2S fueled SOFCs, there is a need to coherently couple these chemical/electrochemical processes with multi-physics processes in SOFCs. To our best knowledge, none of present H_2S SOFC models considers the complicated H_2S reforming reactions.

The objective of the study then is to develop a direct H_2S fueled SOFC model. The detailed chemical kinetics is coherently coupled with multi-physics transport processes. The model is first validated using experimental polarization data. Further simulations are performed to obtain the insight understanding of fundamental mechanisms of direct H_2S fueled SOFCs.

Table 3.1 Chemical/Electrochemical reactions

	Reactions	ΔH
Hydrogen sulfide dissociation(r_1)	$H_2S \leftrightarrow H_2 + 0.5S_2$	$-20.63kJ/mol$
Hydrogen sulfide steam reforming reaction(r_2)	$H_2S + 2H_2O \leftrightarrow 3H_2 + SO_2$	$34.192kJ/mol$
Sulfur steam reforming reaction(r_3)	$S_2 + 4H_2O \leftrightarrow 4H_2 + 2SO_2$	$54.822kJ/mol$
Electrochemical reaction:	Anode: $H_2 + O^{2-} \leftrightarrow H_2O + 2e^-$ Cathode: $O_2/2 + 2e^- \leftrightarrow O^{2-}$	

3.2 CHEMICAL KINETICS OF H_2S AND ELECTROCHEMISTRY

The heterogeneous chemical/electrochemical processes of H_2S in SOFCs are

very complicated, and are influenced by not only the applied materials and catalysts but also the heterogeneous distribution of fuel species. For H_2S fueled Ni-YSZ/YSZ/YSZ-LSM button cell, the detailed reaction mechanisms are listed in Table 3.1, which describes the basic mechanisms of H_2S dissociation process, steam reforming and sulfur reforming processes[77,83]. At the triple phase boundary, where the nickel phase, the YSZ phase, and the gas phase meet together, the hydrogen electro-oxidation process takes place[84,85]. Accordingly the local equilibrium potential is determined as,

$$\eta_{eq} = \frac{\Delta G}{zF} + \frac{RT}{2F}\ln\left(\frac{p_{H_2} p_{O_2}^{0.5}}{p_{H_2O}}\right) \tag{3.1}$$

where, ΔG is the Gibbs free energy of the reaction, z is number of electrons, p is the species partial pressure. The corresponding local Butler-Volmer equation can be formulated as,

$$i_F = z \cdot F \cdot l_{TPB} \cdot i_0 \left[\exp\left(\frac{\alpha z F}{RT}(\eta - \eta_{eq})\right) - \exp\left(-\frac{(1-\alpha) z F}{RT}(\eta - \eta_{eq})\right)\right] \tag{3.2}$$

where, l_{TPB} is the three phase boundary length per unit volume, i_0 is the exchange current density and can be formulated as[74],

$$i_{0,an} = i_{H_2}^* \frac{(p_{H_2} / p_{H_2}^*)^{0.25} (p_{H_2O})^{0.75}}{1 + (p_{H_2} / p_{H_2}^*)^{0.5}} \tag{3.3}$$

$$i_{0,ca} = i_{O_2}^* \frac{(p_{O_2} / p_{O_2}^*)^{0.25}}{1 + (p_{O_2} / p_{O_2}^*)^{0.5}} \tag{3.4}$$

here, $p_{H_2}^*$ is about 4.9 atm; $p_{O_2}^* = 4.9 \times 10^8 \exp(-2 \times 10^5 / RT)$; $i_{H_2}^*$ and $i_{O_2}^*$ are the empirical constants used to fit the numerical results with experimental data.

These chemical/electrochemical processes are coupled with multi-transport

processes of charge, mass, momentum, and energy within the porous electrodes. The governing equations for multi-transport processes are described in chapter 2. Besides, we have the following assumptions: (1) the catalyst Ni is uniformly distributed within the anode; (2) the microstructure of electrodes is stable and homogeneous during the operations; (3) the effect of sulfur poisoning on the pore structure and catalytic property of Ni are negligible.

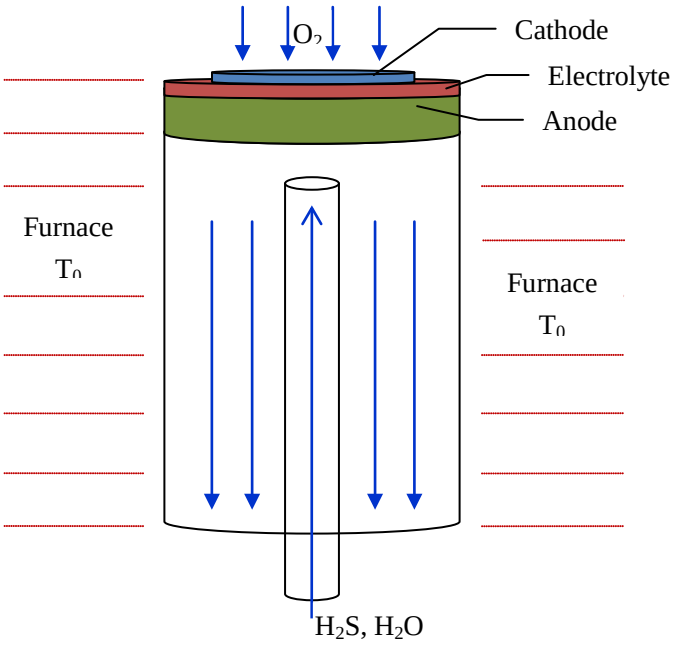

Figure 3.1 Schematic of H_2S fueled SOFC operation system

3.3 MODEL VALIDATION

The model development is based on a physical experimental setup. As shown in Figure 3.1, the anode-supported button cell Ni-YSZ/YSZ/YSZ-LSM is mounted on the top of a large ceramic tube. The fuel is supplied to the anode electrode via a small ceramic tube while the surplus gas and products in the anode flow out through the large ceramic tube. The cathode electrode is exposed to the ambient air. The temperature of

this test stand is controlled by a furnace. In order to precisely determine the boundary conditions at the anode/channel interface, the transport processes in the fuel supply tube is also considered. Due to the axis-symmetry of the test stand, a 2-D axial-symmetric domain is used to model the multi-physics processes in the test stand.

Table 3.2 Boundary conditions

Interfaces(Ω)	$\Omega_{Ca/Cl}$	$\Omega_{Ca/El}$	$\Omega_{El/An}$	$\Omega_{An/Cl}$	Ω_{Cl}
Ionic charge	Insulation	Continuity	Continuity	Insulation	N/A
Electronic charge	Specified voltage	Insulation	Insulation	0	N/A
Mass	O_2/N_2 (Mass fractions)	Insulation	Insulation	Continuity	H_2S/H_2O (Mass fraction)
Momentum	Pressure	Wall (no slip)	Wall (no slip)	Continuity	Flow rate, pressure
Energy	Temperature	Continuity	Continuity	Continuity	Temperature

The mathematical model is solved using COMSOL Multiphysics 4.2a. The model parameters are listed in Tables 3.2-3.5, including the constants of reaction rates, reaction source terms and energy source terms, testing system operating parameters and boundary conditions. For a specified cell voltage at the cathode electrode boundary, the corresponding the species distributions and average cell current density are calculated. The cell polarization curve then is obtained by specifying a series of cell voltages and calculating the corresponding average cell current density. Figure 3.2 shows the experimental polarization curve at 900^{o}C when 5% H_2S and 95%N_2 are used as the fuel. Obviously the model predictions match the experimental data reasonably well. This

model is further utilized for numerical simulations.

Table 3.3 Reaction rates and constants

Reaction Rate	Rate Constant
$r_1 = A_{1f}\ \exp(\frac{-E_{1f}}{RT})(p_{H_2S} - \frac{p_{H_2}\sqrt{p_{S_2}}}{K_1})$	$A_{1f} = 7.84\times10^{6}$; $E_{1f} = 1.96\times10^{5}$;
$r_2 = A_{2f}\ \exp(\frac{-E_{2f}}{RT})(p_{H_2S}\,p_{H_2O}{}^{2} - \frac{p_{H_2}{}^{3}p_{SO_2}}{K_2})$	$A_{2f} = 6.3\times10^{12}$; $E_{2f} = 1.27\times10^{5}$;
$r_3 = A_{3f}\ \exp(\frac{-E_{3f}}{RT})(p_{S_2}\,p_{H_2O}{}^{4} - \frac{p_{H_2}{}^{4}p_{SO_2}{}^{2}}{K_3})$	$A_{3f} = 6.3\times10^{11}$; $E_{3f} = 1.837\times10^{6}$;

Table 3.4 Source terms

Reaction source terms	Energy source terms
$R_{H_2S} = (-r_1 - 0.5r_2)M_{H_2S}$	$R_{Ca} = Q_{h,r} + Q_{h,ac} + Q_{h,ohm}$
$R_{H_2} = (r_1 + 3r_2 + 4r_3)M_{H_2} - i_F M_{H_2}/2F$	$R_{El} = Q_{h,ohm}$
$R_{H_2O} = (-2r_2 - 4r_3)M_{H_2O} + i_F M_{H_2O}/2F$	$R_{An} = Q_{h,r} + Q_{h,ac} + Q_{h,ohm}$
$R_{S_2} = (0.5r_1 - r_3)M_{S_2}$	$R_{Cl} = 0$
$R_{SO_2} = (r_2 + 2r_3)M_{SO2}$	
$R_{O_2} = -i_{0,c}M_{O_2}/4F$	

3.4 RESULTS AND DISCUSSION

3.4.1 The distributions of fuel species and temperature field

Figure 3.3 illustrates the molar fraction distributions of fuel species within the button cell and fuel supply tubes, where 5%H_2S, 10%H_2O and 85%N_2 are supplied to the cell anode and the cathode side is exposed to the ambient air. The operating temperature

Table 3.5 Operating parameters

	Value	Units
Cathode layer thickness, radius	4×10^{-5}, 2.5×10^{-3}	m
Electrolyte layer thickness, radius	2×10^{-5}, 6.5×10^{-3}	m
Anode layer thickness, radius	3.5×10^{-4}, 6.5×10^{-3}	m
Inlet fuel channel radius, wall radius	1×10^{-3}, 1.5×10^{-3}	m
Outlet fuel channel radius	6.5×10^{-3}	m
Pressure	1	atm
Anode ionic conductivity	$3.34\times10^{4}\exp(-10300/T)$	$S\cdot m^{-1}$
Cathode ionic conductivity	$3.34\times10^{4}\exp(-10300/T)$	$S\cdot m^{-1}$
Anode electronic conductivity	2×10^{6}	$S\cdot m^{-1}$
Cathode electronic conductivity	$42\times10^{6}\exp(-1150/T)/T$	$S\cdot m^{-1}$
Electrolyte ionic conductivity	$3.34\times10^{4}\exp(-10300/T)$	$S\cdot m^{-1}$
Porosity(ε)	0.4	1
Particle diameter	2×10^{-6}	m
Tortuosity	$(\frac{3-\varepsilon}{2})^{0.5}$	1
Permeability	$\frac{\varepsilon^3 d^2}{150(1-\varepsilon)^2}$	1
Specific three-phase boundary length	1.8×10^{12}	$m\cdot m^{-3}$

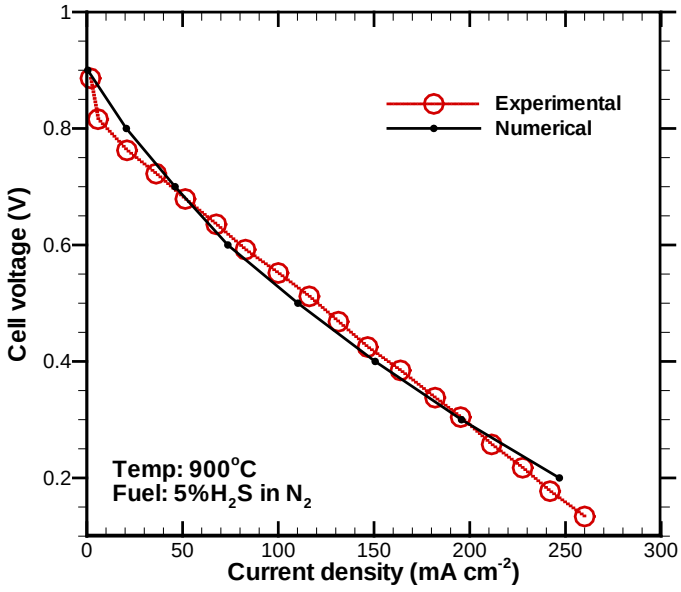

Figure 3.2 Comparison between numerical result and experimental data

of the furnace is set at 900^{o}C and the cell voltage is 0.2V. As shown in the figure, the molar fraction of H_2S is relatively uniform in the small tube. Beyond the outlet of the small tube, the molar fraction of H_2S decreases toward the anode electrode. The molar fractions of H_2O and SO_2 show opposite trends. One also can notice that the distribution of generated S_2 shows relative high concentration around the circumference of the anode. For the ideal gas, the molar fraction concentration is proportional to its partial pressure. Accordingly the partial pressure of the generated S_2 is relatively high around the anode circumference. It has been realized that the higher partial pressure of S_2 (or S) indicates the worse sulfur poisoning effect[81,86]. It seems that the sulfur poisoning effect is relatively severe around the anode circumference.

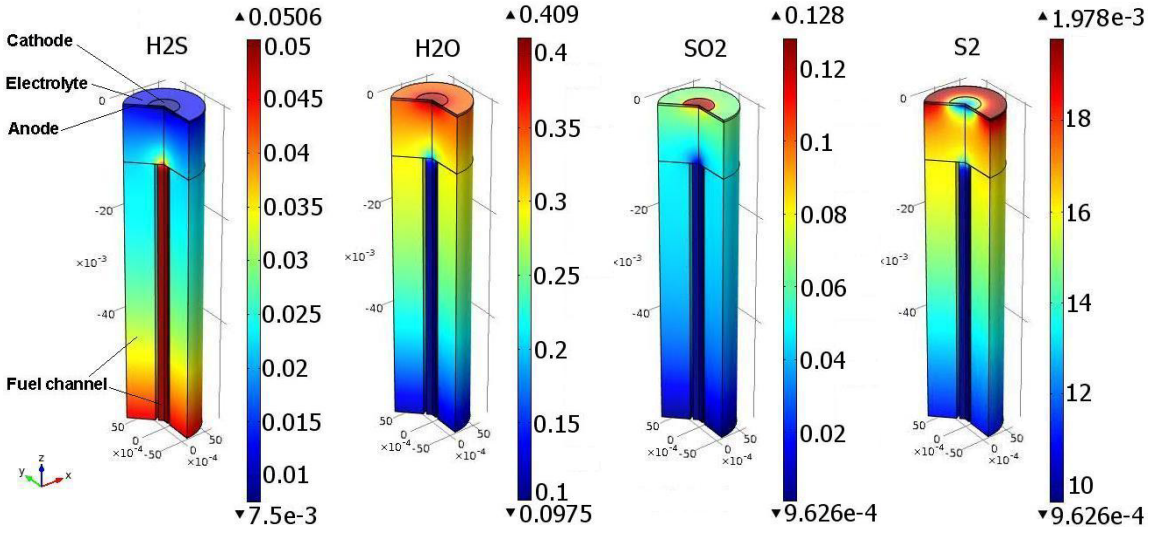

Figure 3.3 Distribution of gas species within the fuel cell and tube system

The distribution of temperature field is shown in Figure 3.4. It is clear that the highest temperature is present at the anode side, particularly the area well aligned with the cathode along the axial-symmetric line. Since the heat generation within the cell is mainly due to the heterogeneous chemical/electrochemical reactions, the results indicate

that the intensive reactions mainly take place in the anode.

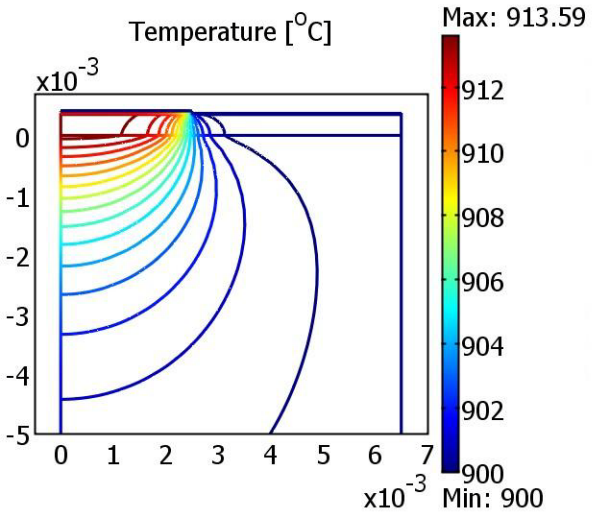

Figure 3.4 Temperature field distribution in the button cell and fuel supply tubes

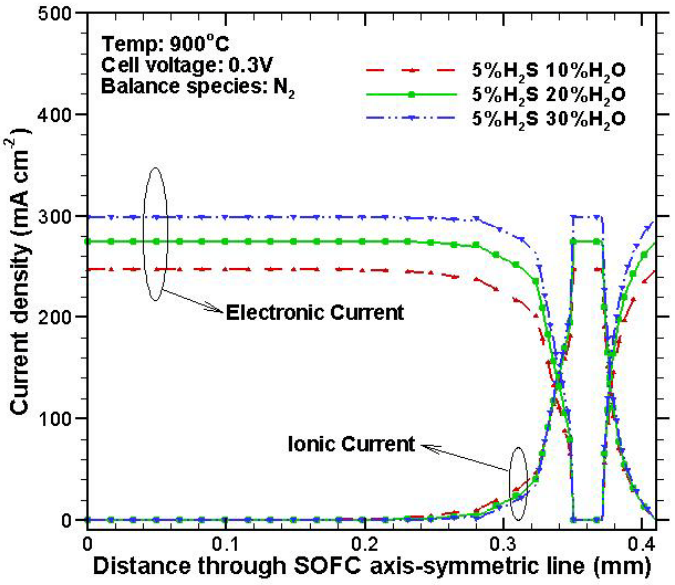

Figure 3.5 Effect of H_2O content on the distribution of electronic/ionic current densities along the axis-symmetric line (r=0)

3.4.2 The effect of H_2O content

Since the steam content affects the H_2S reforming and sulfur reforming reactions, it may have significant effects on H_2S fueled SOFCs. In this section, the effect of H_2O

content is studied. We consider three fuel compositions with different H_2O contents, i.e., $5\%H_2S+10\%H_2O$, $5\%H_2S+20\%H_2O$ and $5\%H_2S+30\%H_2O$. The N_2 is used as the balance species. The operating temperature is set at 900^oC and the cell voltage is 0.3V. In order to clearly illustrate the effects, the simulation results are recorded along the axis-symmetric line of the cell. As shown in Figure 3.5, the electronic current density shows relatively high gradient at the electrodes/electrolyte interfaces and is uniform towards the channel/anode interface. The ionic current density shows the highest gradient at both the anode/electrolyte interface and cathode/electrolyte interface. Within the electrolyte, the ionic current density is very uniform. Towards the channel/anode interface, the ionic current density approaches zero. Obviously increasing the H_2O content from 10% to 30% in the H_2S fuel significantly improves both electronic current density and ionic current density. Therefore, suitable increasing the H_2O content in H_2S

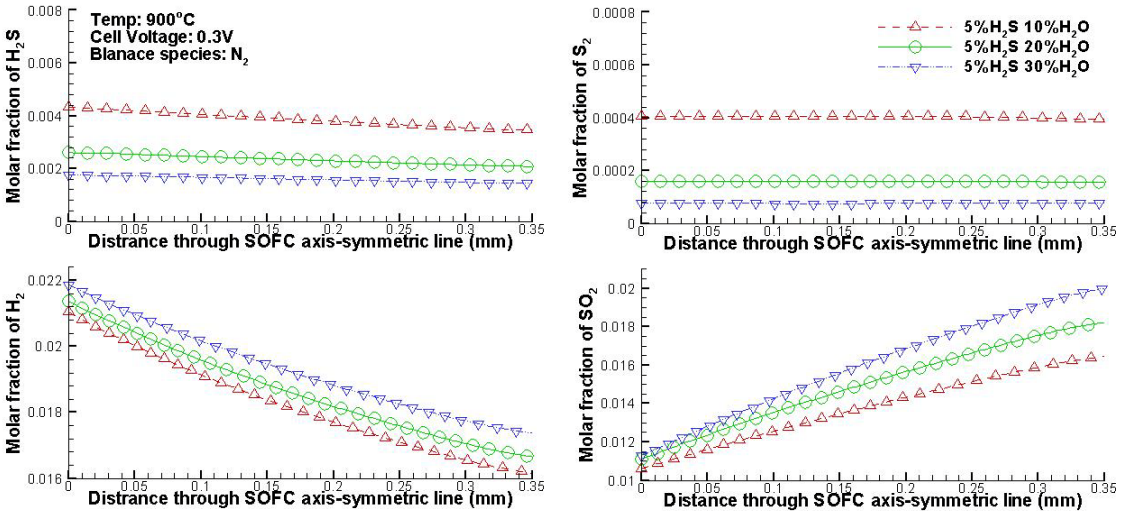

Figure 3.6 The effect of H_2O content on the fuel species distribution through axis-symmetric line (r=0)

in fuel is beneficial for the improvement of SOFC electrochemical performance. The

corresponding molar fraction distributions of fuel species in the anode along the cell axis-symmetric line are shown in Figure 3.6. It can be seen that increasing the H_2O content leads to the decrease of molar fraction of H_2S fuel, implying that the consumed H_2S increases. Accordingly the generated H_2 and SO_2 increase. It also can be noted that the generated S_2 decreases, indicating that high steam content may potentially mitigate the sulfur poising effect.

3.4.3 The effect of operating temperature and cell voltage

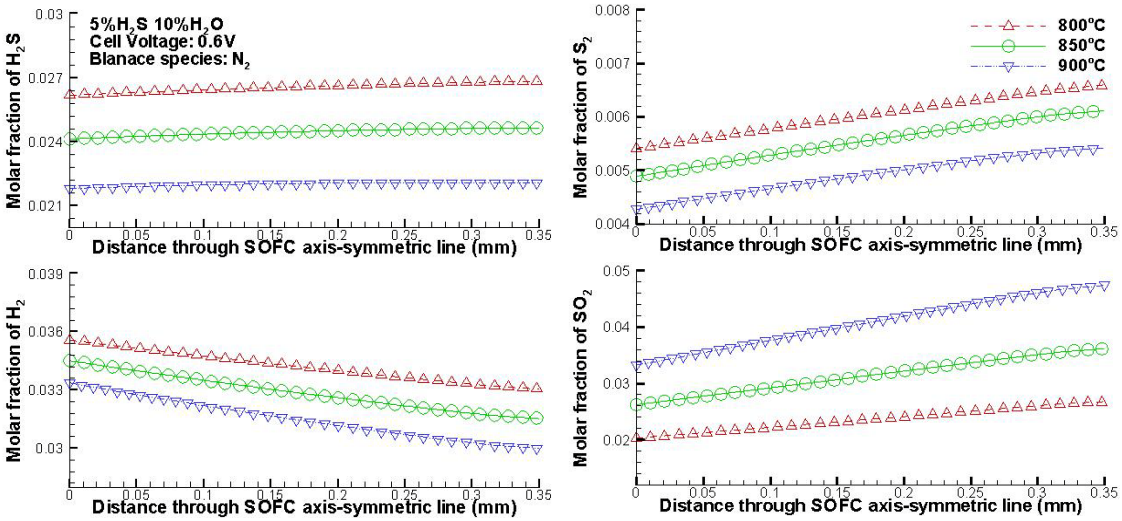

Figure 3.7 The effect of operating temperature on the fuel species distribution through axis-symmetric line (r=0)

The operating temperature can significantly influence multi-physical transport processes and local chemical/electrochemical reactions. As shown in Figure 3.7, the molar fractions of H_2S, H_2, and S_2 decrease when the operating temperature increases from 800°C to 900°C while that of SO_2 increases. This observation indicates that the higher temperature facilitates the reforming of H_2S and improves the consumption of the generated H_2. Accordingly the electrochemical performance of the cell is enhanced.

Since the molar fraction of the generated S_2 decreases, the corresponding sulfur poisoning effect is mitigated.

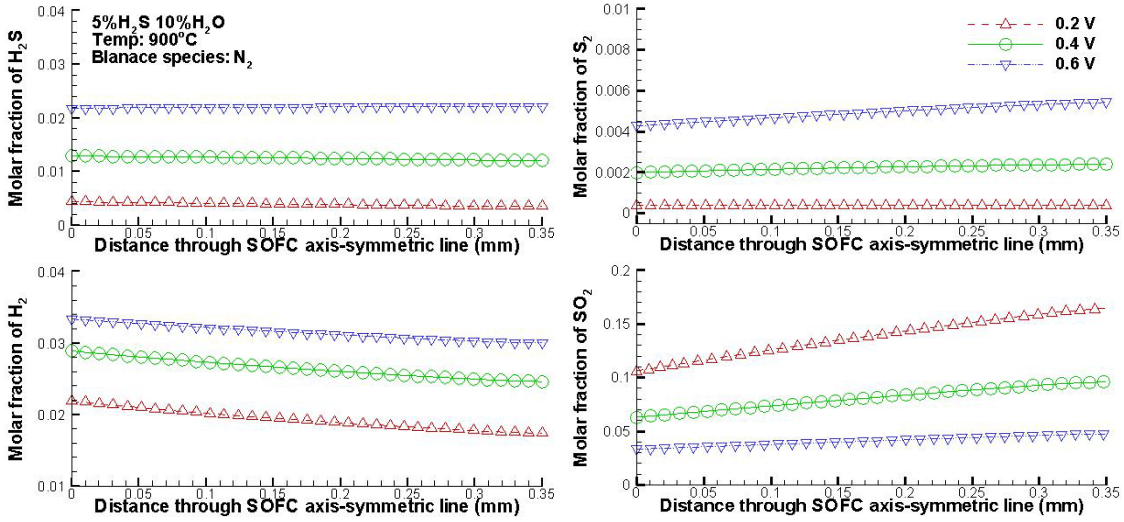

Figure 3.8 The effect of operating cell voltage on the fuel species distribution through axis-symmetric line (r=0)

The effect of cell operating voltage on the molar fraction distributions of fuel species is illustrated in Figure 3.8. When the cell voltage decreases from 0.6V to 0.2V, the molar fractions of H_2S, H_2, and S_2 decrease while that of SO_2 increases. Decreasing the cell voltage actually leads to the increase of the cell current. Accordingly the consumption of H_2 increases due to the electro-oxidation of H_2. The reduced H_2 may further improve the conversion of H_2S. The decrease of generated S_2 implies that lowering the cell voltage may potentially mitigate the sulfur poisoning effect.

3.4.4 Flow rate effect

Figure 3.9 illustrates the effect of fuel flow rate on the fuel species distribution within the button cell and fuel supply tubes. Here the fuel composition of $5\%H_2S+10\%H_2O$ is utilized at the inlet of fuel supply tube. The operating temperature

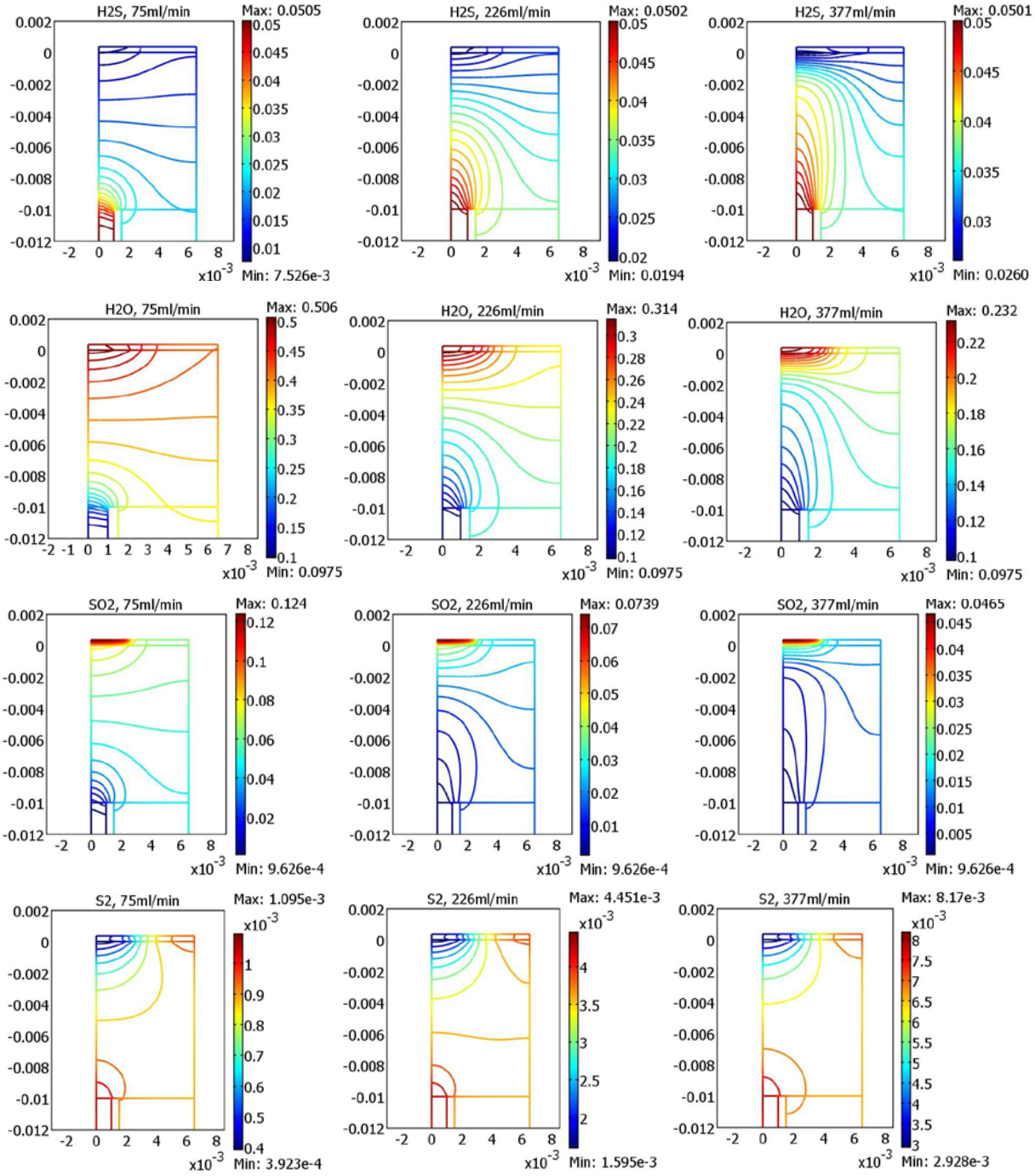

Figure 3.9 The effect of fuel flow rate on the fuel gas species distribution

and cell voltage are set at 900^{o}C and 0.2V respectively. When the fuel flow rate increases 75ml/min to 226ml/min and 377ml/min, the molar fraction of H_2S shows obvious increase from the outlet of the small fuel supply tube towards the anode. The molar

fraction increase of H_2S in turn will enhance the chemical/electrochemical processes. This can be seen from other species distributions. The molar fractions of H_2O and SO_2 decrease, indicating that the consumptions of both H_2O and SO_2 are improved. However the molar fraction of S_2 increases with increasing the fuel flow rate, indicating that the high fuel flow rate may potentially intensify the sulfur poisoning effect.

3.5 CONCLUSIONS

A direct H_2S fueled SOFC model is developed based on a button cell test system. The model considers the detailed chemical reforming processes of H_2S and the multi-physics processes in button cell and fuel supply tubes. The model is validated using experimental polarization curve. Upon the model validation, extensive simulations are performed. Results show that operating conditions have significant different effects on the fuel/gas species distributions and cell performance. Suitable increasing the H_2O content in H_2S fuel can improve SOFC electrochemical performance and potentially mitigate the sulfur poising effect. High operating temperature may facilitate the reforming of H_2S and improve the electrochemical performance as well as mitigate the sulfur poisoning effect. Simulation results also show that lowering both the cell voltage and fuel flow rate may potentially mitigate the sulfur poisoning effect.

CHAPTER 4

MODELING OF DIRECT CH_4 FUELED SOLID OXIDE FUEL CELLS WITH GLOBAL REFORMING CHEMICAL KINETICS

4.1 INTRODUCTION

Solid oxide fuel cells (SOFCs) have gained increasing interests as electrochemical energy conversion systems due to their high efficient and environmentally benign characteristics[87]. Compared to other type of fuel cells, SOFCs are much more fuel-flexible, which can use a variety of fuels such as hydrogen, natural gas, coal gas, or other hydrocarbon fuels. SOFC directly fueled with hydrocarbon is a promising technology to simplify the fuel-reforming system and reduce the total cost [88]. When hydrocarbon fuel is used, very complicated thermal/electrochemical reactions are involved. Experimental results show that methane could react with the steam to generate hydrogen and carbon monoxide at the surface of transition metal catalysts [89-91]; methane also has dissociation process at high operating temperature to generate carbon and hydrogen under the Ni catalysis condition. The carbon could deposit on the surface of the nickel and quickly destroying the catalytic performance of the nickel. To better utilize hydrocarbon fuels, the internal reaction processes are worth to be further studied. In this respect, modeling techniques are cost-effective for this purpose. The methane

fueled SOFCs have been investigated in a few references[92-97]. Nevertheless, it is generally assumed that only hydrogen is oxidized within the anode, while methane and carbon monoxide, if present, are reformed or shifted to produce hydrogen[92,93]. Since the oxidation process of direct carbon monoxide is neglected, the modeling results could be misleading. To overcome this limitation, CO-CO_2 oxidation electrochemistry has been considered in recent modeling studies[94,95,74]. When CO-CO_2 electrochemical reactions are considered, the corresponding reforming reactions are very complicated by the presence of CH4, H_2 and H_2O species, which are rarely considered in the open literature. Obviously, there is a need to couple the electrochemical processes of both H_2-H_2O and CO-CO_2 with primary methane dissociation and reforming reactions.

Table 4.1 Chemical/Electrochemical reactions

	Reactions
Methane dissociation(r_1)	$CH_4 \leftrightarrow C + 2H_2$
Methane steam reforming reaction(r_2)	$CH_4 + H_2O \leftrightarrow 3H_2 + CO$
Methane dry reforming reaction(r_3)	$CH_4 + CO_2 \leftrightarrow 2H_2 + 2CO$
Carbon monoxide steam reaction(r_4)	$CO + H_2O \leftrightarrow H_2 + CO_2$
Electrochemical reaction:	Anode : $H_2 + O^{2-} \leftrightarrow H_2O + 2e^-$ $CO + O^{2-} \leftrightarrow CO_2 + 2e^-$ Cathode: $O_2/2 + 2e^- \leftrightarrow O^{2-}$

In this study, a direct methane fueled SOFC model is developed, taking into account of both H2-H2O and CO-CO2 oxidation reactions and their interactions with methane reforming. The model is validated by experimental data under different fuel conditions. Based upon the validated model, further simulation studies are carried out to investigate the steady state and transient performance of the cell.

4.2 REACTION MECHANISMS WITHIN ELECTRODES

With methane as the fuel, very complicated interactions exist between the primary methane dissociation, the reforming reactions as well as the electrochemical processes of both H_2-H_2O and CO-CO_2. Table 4.1 lists these reactions proved by experiments[96,97]. The corresponding reaction rates and rate constants are listed in Table 4.2. In general, the form of a chemical/electrochemical reaction can be written as,

$$\sum_i^n n_i Ra_i \leftrightarrow \sum_j^m m_j Pu_j + ze^- \tag{4.1}$$

where, Ra is the reactant, Pu is the product, n_i and m_j are the stoichiometric factors for the reactants and products, respectively, z is the number of electrons. For the single-step elementary reactions, the forward and backward reaction rate coefficients k_f and k_b can be represented as,

$$k_f = AT^n \exp(\frac{-E^{act}}{RT}) \exp(\alpha \frac{zF}{RT} \eta) \tag{4.2}$$

$$k_b = AT^n \exp(\frac{-E^{act}}{RT}) \exp(-(1-\alpha) \frac{zF}{RT} \eta) \tag{4.3}$$

where, E^{act} is the thermal activation energies, η is the electrical potential difference between THE reactants and products. The net reaction rate R_n then can be calculated as,

$$R_n = k_f \prod_i [Ra_i]^{n_i} - k_b \prod_j [Pu_j]^{m_j} \tag{4.4}$$

Using the Nernst equation, the equilibrium potential η_{eq} and the Butler-Volmer equation can be constructed respectively as,

$$\eta_{eq} = \frac{\Delta G}{zF} + \frac{RT}{zF}\ln(\frac{\prod_j [Pu_j]^{m_j}}{\prod_i [Ra_i]^{n_i}}) \tag{4.5}$$

$$i = i_0[\exp(\frac{\alpha zF}{RT}(\eta - \eta_{eq})) - \exp(-\frac{(1-\alpha)zF}{RT}(\eta - \eta_{eq}))] \tag{4.6}$$

where, ΔG is the Gibbs free energy of the reaction, i_0 is the exchange current density. If the hydrogen electro-oxidation pathway is dominant, equation (5) can be simplified as,

$$\eta_{eq} = E^0 + \frac{RT}{2F}\ln(\frac{p_{H_2} p_{O_2}^{0.5}}{p_{H_2O}}) \tag{4.7}$$

Table 4.2 Reaction rates and Rate constants

Reaction Rate	Rate Constant
$r_1 = k_{11}\frac{p_{CH_4} - \frac{p_{H_2}^2}{K_1}}{(1 + k_{12}\sqrt{p_{H_2}})^2}$	$k_{11} = 2.31\times10^{-5}\exp(20.492 - \frac{104200}{R_g T})$ $k_{12} = \exp(\frac{163200}{R_g T} - 22.426)$ $K_1 = 5.088\times10^{5}\exp(-\frac{91200}{R_g T})$
$r_2 = k_{2f}[CH_4][H_2O] - k_{2b}[CO][H_2]^3$	$k_{2f} = 2.3\times10^{-8}$ $k_{2b} = 1.4\times10^{-20}$
$r_3 = \frac{K_{31}K_{32}k_3[CH_4][CO]}{K_{31}K_{32}[CH_4][CO_2] + K_{31}[CH_4] + K_{32}k_3[CO_2]}$	$K_{31} = 2.61\times10^{-3}\exp(-\frac{4300}{T})$ $K_{32} = 5.71\times10^{-5}\exp(\frac{8700}{T})$ $k_3 = 5.35\times10^{-1}\exp(-\frac{7500}{T})$
$r_4 = k_{4f}[CO][H_2O] - k_{4b}[CO_2][H_2]$	$k_{4f} = 1.5\times10^{-7}$ $k_{4b} = 1.4\times10^{-7}$

According to Zhu et al[74], And the exchange current density for H_2-H_2O oxidation process can be formulated as,

$$i_{0,an}^{H_2} = i_{H_2}^* \frac{(p_{H_2}/p_{H_2}^*)^{0.25}(p_{H_2O})^{0.75}}{1 + (p_{H_2}/p_{H_2}^*)^{0.5}} \tag{4.8}$$

$$i_{0,ca} = i_{O_2}^* \frac{(p_{O_2}/p_{O_2}^*)^{0.25}}{1 + (p_{O_2}/p_{O_2}^*)^{0.5}} \tag{4.9}$$

where, $p^*_{H_2}$ was about 0.7atm; $p^*_{O_2} = 4.9\times10^8 \exp(-2\times10^5 / RT)$; $i^*_{H_2}$ and $i^*_{O_2}$ are the empirical constants used to fit the numerical results with experimental data.

The rate-determining step of CO-CO_2 oxidation process is quite similar to that of H_2-H_2O oxidation process[98]. It is realized that the rate of CO oxidation is 2-3 times less than that of hydrogen oxidation under the same oxidant partial pressure. When the rate of CO oxidation reaction is assumed to be three times lower than that of H_2 oxidation, the modeling result is able to obtain a good agreement with experimental data[99]. Here this assumption is employed to describe CO-CO_2 oxidation electrochemistry,

$$i^{CO}_{0,an} = \frac{i_0}{3}[\exp(\frac{\alpha z F}{RT}(\eta - \eta_{eq})) - \exp(-\frac{(1-\alpha) z F}{RT}(\eta - \eta_{eq}))] \tag{4.10}$$

$$i_{0,an} = i^*_{CO} \frac{(p_{CO} / p^*_{CO})^{0.25} (p_{CO_2})^{0.75}}{1 + (p_{CO} / p^*_{CO})^{0.5}} \tag{4.11}$$

And the total exchange current density within the anode can be formulated as,

$$i_{0,an} = i^{H_2}_{0,an} + i^{CO}_{0,an} \tag{4.12}$$

Table 4.3 Reaction Source terms

Reaction source terms	Energy source terms
$R_{CH_4} = (-r_1 - r_2 - r_3) M_{CH_4}$	$R_{Cathode} = Q_{ohm} + Q_{chem/entropy}$
$R_{H_2} = (2r_1 + 3r_2 + 2r_3) M_{H_2} - i^{H_2}_{0,an} M_{H_2} / 2F$	$R_{Electrolyte} = Q_{ohm}$
$R_{H_2O} = (-r_2 - r_4) M_{H_2O} + i^{H_2}_{0,an} M_{H_2O} / 2F$	$R_{Anode} = Q_{ohm} + Q_{chem/entropy}$
$R_{CO} = (r_2 + 2r_3 + r_4) M_{CO} - i^{CO}_{0,an} M_{CO} / 2F$	$R_{Fuel-channel} = 0$
$R_{CO_2} = (-r_3 + r_4) M_{CO2} + i^{CO}_{0,an} M_{CO_2} / 2F$	
$R_{O_2} = -i_{0,c} M_{O_2} / 4F$	

4.3 SOLUTION ALGORITHM AND MODEL VALIDATION

In addition to the global reforming chemistry and electro-oxidation processes, SOFCs also include very complicated transport processes. Figure 4.1 has illustrated the corresponding experimental setup, of which the transport processes include fuel/gas transport in fuel supply tubes and porous electrodes, charge transport through material backbone, as well as heat transfer. The governing equations for these processes are described in chapter 2.

Table 4.4 Boundary conditions

Interfaces(Ω)	$\Omega_{Ca/Cl}$	$\Omega_{Ca/El}$	$\Omega_{El/An}$	$\Omega_{An/Cl}$	Ω_{Cl}
Ionic charge	Insulation	Continuity	Continuity	Insulation	N/A
Electronic charge	Specified voltage	Insulation	Insulation	0	N/A
Mass	O_2/N_2 (Mass fractions)	Insulation	Insulation	Continuity	CH_4/H_2O (Mass fraction)
Momentum	Pressure	Wall (no slip)	Wall (no slip)	Continuity	Flow rate, pressure
Energy	Temperature	Continuity	Continuity	Continuity	Temperature

The mathematical model is solved by using COMSOL MULTIPHSICS V4.0a. The model parameters and boundary conditions are provided in Table 4.3-4.5. For a specified cell voltage at cathode electrode boundary, the corresponding average cell current density is calculated. Accordingly, a variety of species distributions are calculated. The cell polarization curve is obtained by specifying a series of cell voltages and calculating the corresponding cell current density. And the species distributions

associated with multi-physicochemical processes are calculated under each of the individual voltage conditions.

Table 4.5 Operation parameters

	Value	Units
Cathode layer thickness, radius	4×10^{-5}, 2.5×10^{-3}	m
Electrolyte layer thickness, radius	2×10^{-5}, 6.5×10^{-3}	m
Anode layer thickness, radius	3.5×10^{-4}, 6.5×10^{-3}	m
Inlet fuel channel radius, wall radius	1×10^{-3}, 1.5×10^{-3}	m
Outlet fuel channel radius	6.5×10^{-3}	m
Faraday Constant	96500	$C\cdot mol^{-1}$
Gas constant	8.314	$J\cdot mol^{-1}K^{-1}$
Operating Temperature	700	^{o}C
Pressure	1	atm
Anode ionic conductivity	$3.34\times10^{4}\exp(-10300/T)$	$S\cdot m^{-1}$
Cathode ionic conductivity	$3.34\times10^{4}\exp(-10300/T)$	$S\cdot m^{-1}$
Anode electronic conductivity	2×10^{6}	$S\cdot m^{-1}$
Cathode electronic conductivity	$42\times10^{6}\exp(-1150/T)/T$	$S\cdot m^{-1}$
Electrolyte ionic conductivity	$3.34\times10^{4}\exp(-10300/T)$	$S\cdot m^{-1}$
Anode local electrical capacity	0.01	mF
Cathode local electrical capacity	0.1	mF
Porosity(ε)	0.4	1
Particle diameter	2×10^{-6}	m
Tortuosity	$(\frac{3-\varepsilon}{2})^{0.5}$	1
Permeability	$\frac{\varepsilon^{3}d^{2}}{150(1-\varepsilon)^{2}}$	1
Inlet velocity	0.2	$m\cdot s^{-1}$

The model validation is carried out by comparing the model predictions with experiment data under identical operating conditions. The polarization curves of the cell are obtained under two different fuel compositions: 97%H_2+3%H_2O and 97%CH_4+3%H_2O. As shown in Figure 4.2, the model predictions match with experimental data reasonably well with different fuels at three temperature conditions of 600^{o}C, 650^{o}C and 700^{o}C.

4.4 RESULTS AND DISCUSSIONS

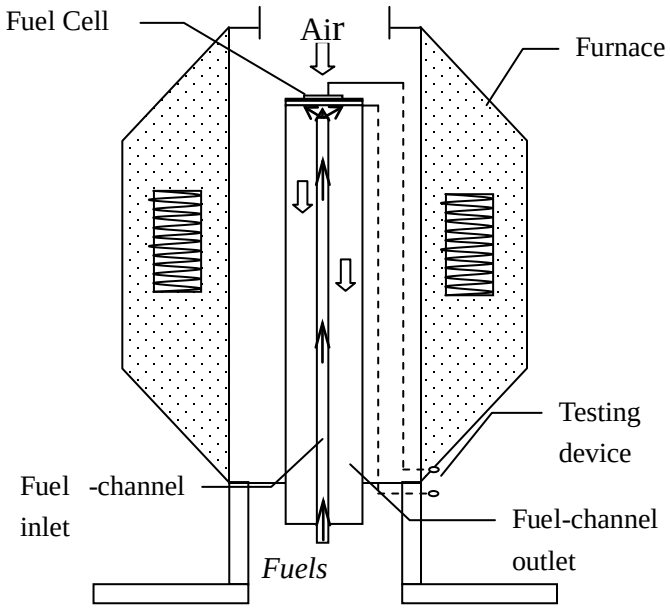

Figure 4.1 Experimental setup of SOFC testing system

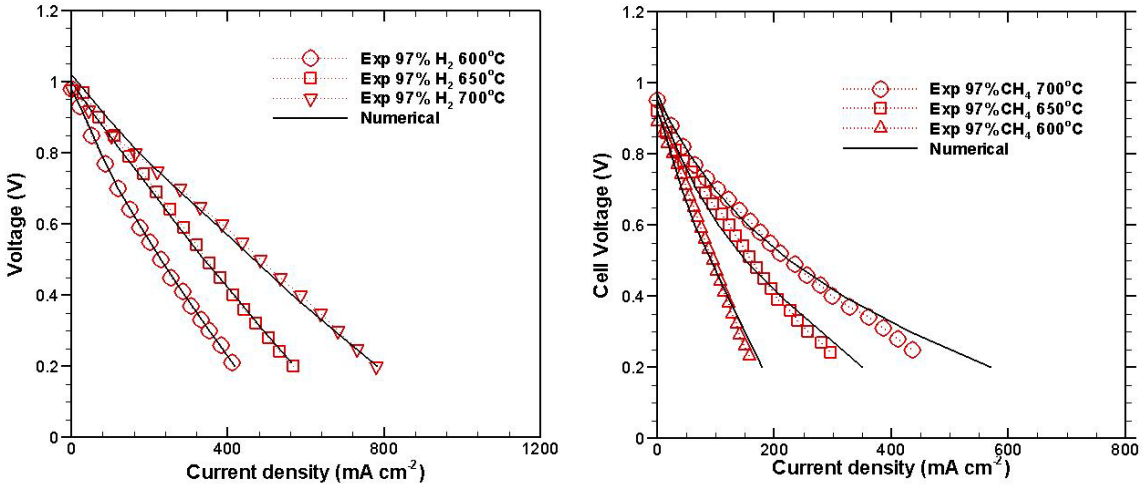

Figure 4.2 Comparison between experimental data and numerical results

4.4.1 Steady state analysis

4.4.1.1 Distribution of bulk gas species

Figure 4.3 shows the molar fraction distributions of various fuel/gas species, where the inlet fuel is composed of 84%CH_4, 4%CO, 4%H_2, 4%H_2O and 4%CO_2. The

operating temperature and the cell voltage are set at 700^{o}C and 0.5V respectively. It can be seen that the molar fractions of reactants, CH_4, H_2 and CO, decrease from the anode inlet toward the anode/electrolyte interface. CH_4 is decomposed into various gas species such as H_2 and CO; the generated H_2 and CO are consumed by electrochemical reactions. The reduced concentrations of H_2 and CO further drive the decomposition of CH_4. The electrochemical reaction sites take place in the anode electrode, resulting in the decreasing trend from the fuel inlet toward the anode electrode. On the other hand, H_2O and CO_2 are produced in the anode electrode through electrochemical reactions. Accordingly the molar fractions show opposite trend, decreasing from the anode/electrolyte interface toward the fuel/gas outlet.

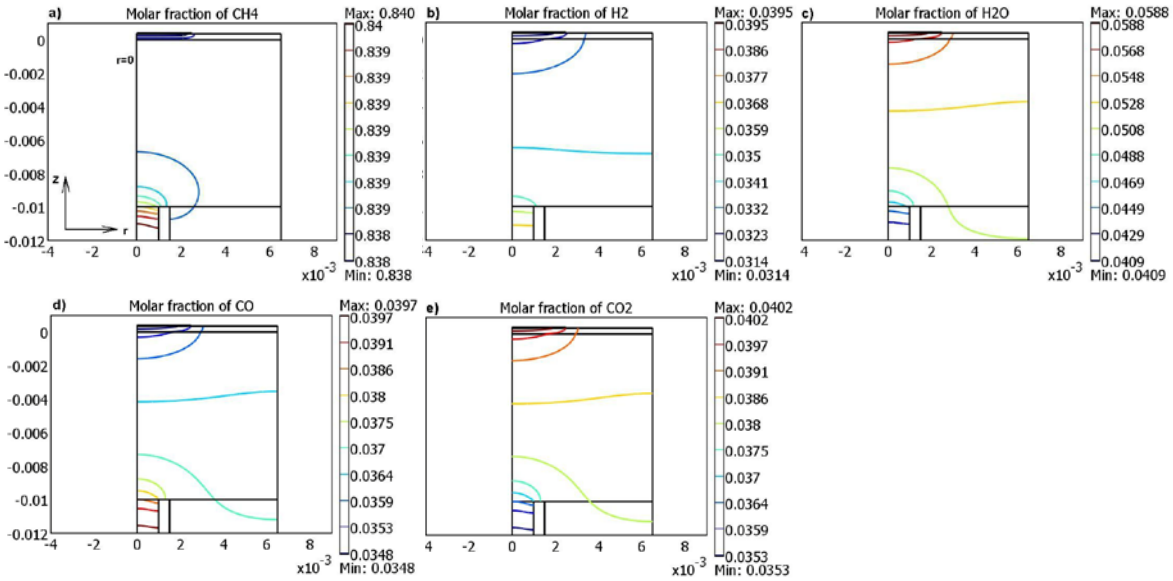

Figure 4.3 Distribution of bulk fuel species within the testing system

4.4.1.2 Effect of CO-CO_2 electrochemical process

In this section, the effect of CO-CO_2 electrochemical process is highlighted in hydrocarbon gas fueled SOFCs. As shown in Figure 4.4, with and without consideration

of $CO\text{-}CO_2$ electrochemical process, the cell polarization performance shows a clear difference, indicating that the contribution of CO-CO2 oxidation process to the electrical current generation of the cell. The involvement of CO-CO2 oxidation process also affects the concentration distributions of gas species. Figure 4.5 shows the concentration comparisons of species along the axis-symmetrical line of the cell with/without considering the CO-CO2 oxidation process, where the operating temperature is 700^oC and the cell voltage is set at 0.5V. Without $CO\text{-}CO_2$ oxidation process, the concentrations of CH_4, H_2 and CO_2 are lower than those with $CO\text{-}CO_2$ oxidation process, while the corresponding concentrations of H_2 and CO_2 are higher. Once the $CO\text{-}CO_2$ oxidation process is taken into account, the concentration distributions of the species flip over. This observation indicates that $CO\text{-}CO_2$ oxidation process has significant effects on the CH_4 decomposition and electrochemical reactions.

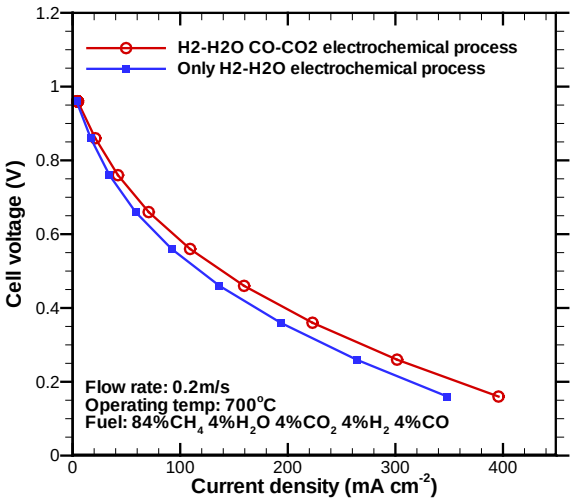

Figure 4.4 Effect of $CO\text{-}CO_2$ electrochemical process on the SOFC output performance

4.4.1.3 Pressure/temperature distribution and effects of fuel composition

Figure 4.6 shows the distributions of pressure and temperature fields under the same operating conditions as in Figure 4.4. Both distributions decrease from the anode electrode toward the outlet of fuel supply tube, and the high values of pressure and temperature appear near the anode/electrolyte interface. The results indicate that the reactions of methane reforming and oxidation mainly take place at this site.

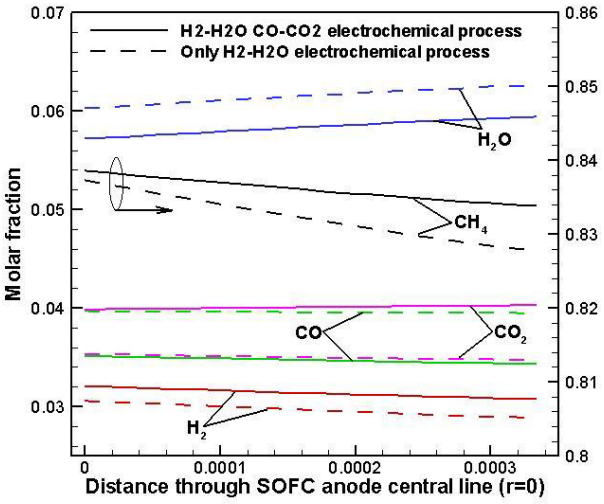

Figure 4.5 The distribution of synthesis gas species in anode along axis-symmetrical line under different electrochemical processes

The fuel composition at the inlet will greatly influence the dissociation and reforming processes of methane and consequently the cell performance. Figure 4.7 shows the cell current density variations with respect to the inlet fuel compositions when the cell voltage is set at 0.2V. For the inlet fuel composition of mixed CH_4 and H_2O, the cell current density increases with decreasing the content of H_2O from ~100% to 35%; beyond 35%, further decreasing the H_2O content actually makes the cell performance worsen. Addition of CO into the methane has a slight effect on cell performance,

particularly at the CO content between 100% and 80%. Beyond 80%, further decreasing the CO content shows little effect on the cell performance. With the mixture of CH_4 and CO_2 as the fuel, the cell performance monotonically increases with decreasing CO_2 content.

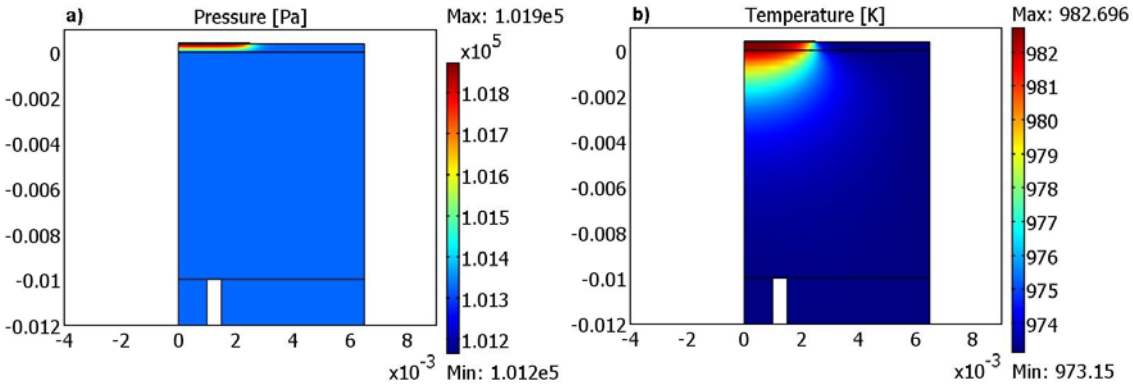

Figure 4.6 The distribution of pressure and temperature fields in the testing system

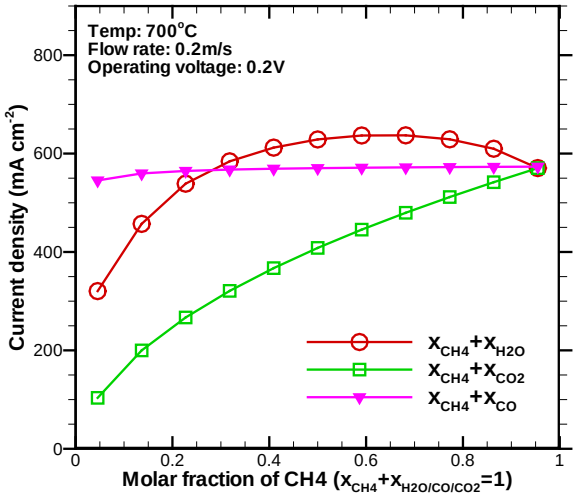

Figure 4.7 The effect of fuel gas content on the SOFC output performance

4.4.2 Transient cell performance

The transient behaviors of the methane fueled cell are studied by applying a step change of the operating voltage and fuel inlet velocity to the cell respectively. We record

the responses of various species at the intersecting point between the axis-symmetrical line and the electrode/electrolyte interface.

4.4.2.1 Step change effects of cell voltage

In this section, the transient behavior of the cell is studied. The operating temperature of the furnace is set at 700^{o}C. The cell voltage is set at 0.5V and has a step decrease of 0.1V at the 20th second as shown in Figure 4.8. The corresponding responses of the species molar fraction at the concerned intersecting point are then calculated. As can be seen, it takes about 20 seconds for the species CH_4, H_2, CO, H_2O and CO_2 to change from one steady state to another. The responses of species CH_4 and CO_2 are relatively slow while those of species H_2, CO, and H_2O are relatively fast. At the cathode

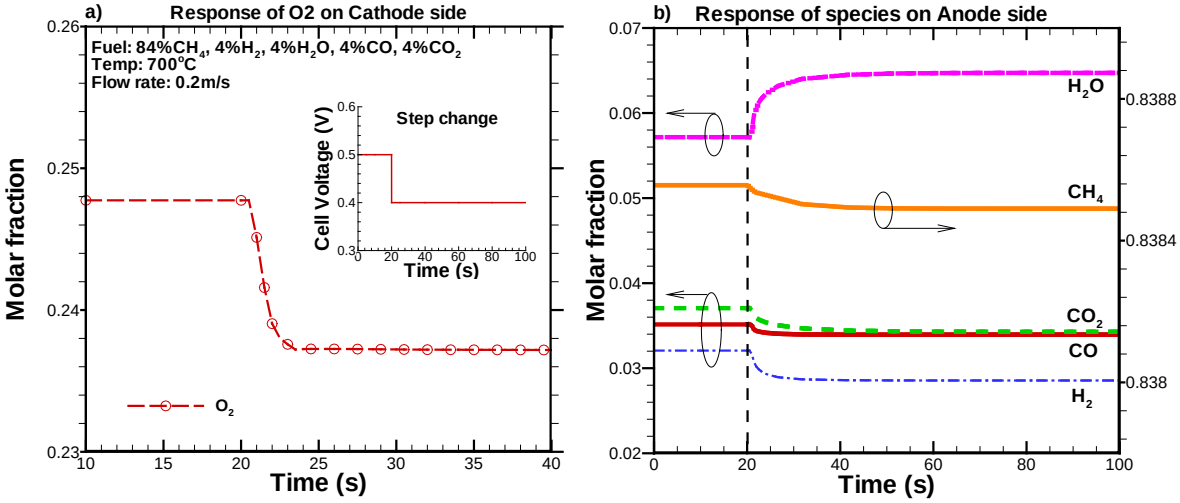

Figure 4.8 Response of gas species to the step change of cell voltage

side, the response of O2 is pretty fast, and less than 5 seconds from one steady state to another. It is generally recognized that the oxygen reduction reaction in the cathode is the most sluggish process in the cell when humidified hydrogen is used as the fuel[100]. The

present simulation results demonstrate that the processes in the anode are slow than that in the cathode. Due to the fact that the reforming process of CH_4 in the anode has multiple steps and is coupled with oxidation processes of H_2 and CO, leading to the overall slow effects. The result also indicates that anode is the critical component limiting the electrochemical performance for direct methane fueled SOFCs.

4.4.2.2 Step change effects of fuel inlet velocity

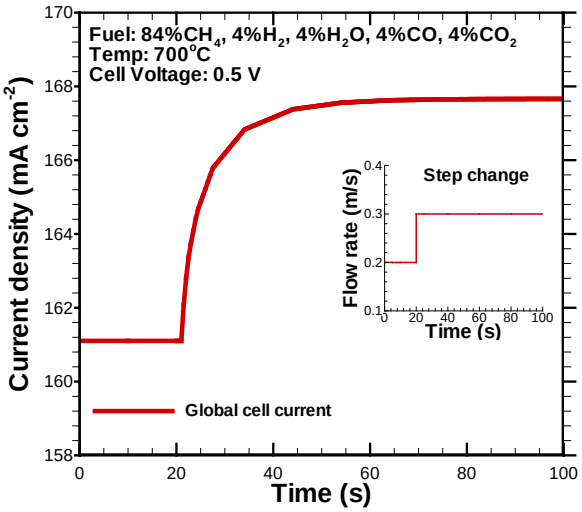

Figure 4.9 The response of global cell current to the step change of fuel flow rate

The step change effects of fuel inlet velocity on the cell performance and the species concentrations in the anode are also studied. Here the operating temperature of the furnace is set at 700°C. The cell voltage is set at 0.5V. The anode inlet fuel is composed of 84%CH_4, 4%CO, 4%H_2, 4%H_2O and 4%CO_2. The fuel inlet velocity increases from 0.2m/s to 0.3m/s at 20th second. As shown in Figure 4.9, the current density has an obvious increase from 161mA/cm^2 to 167.8 mA/cm^2. The transient procedure takes about 40 seconds. Figure 4.10 shows the corresponding responses of the

reaction species in the anode at the concerned intersecting point defined above. The molar fractions of species CH_4, CO, H_2, and CO_2 increase to a steady state with high values. However that of species H_2O decreases. In general, the H2O generated from electrochemical reaction increases with increasing the cell current density. In the present situation, increasing the current density actually decreases the generated H_2O. This fact indicates that part of the generated H_2O is consumed by the reforming reactions of CH_4. As a result, increasing the inlet flow rate of the fuel is able to improve the reforming reactions of CH_4 and the cell performance.

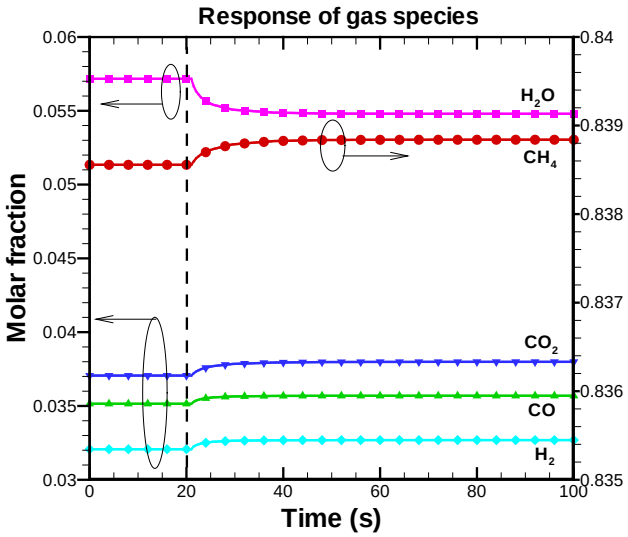

Figure 4.10 Transient response of fuel species to the step change on flow rate

4.5 CONCLUSION

Direct methane fueled SOFC model is developed, in which the methane reforming processes are coherently integrated with multi-transport processes within a button cell test system. The model takes into account the two electrochemical reaction processes of hydrogen and carbon monoxide oxidations. The model is validated using

experimental polarization curve under the temperature condition of 600^{o}C, 650^{o}C and 700^{o}C. Simulation results show that the reaction processes in the anode of direct methane fueled cell are more sluggish than the oxygen reduction process in the cathode, which is the opposite case to hydrogen fueled SOFCs. The CO-CO_2 oxidation process plays an important role, which not only directly influences the cell performance but also affects methane reforming process. The results also show that H2O is able to improve the cell performance through intensifying the methane reforming reactions, while CO and CO2 have relatively small effects. Increasing the inlet flow rate of the anode is able to improve the methane reforming process and the cell performance.

CHAPTER 5

MULTIPHYSICAL MODELING OF CH_4 AND H_2S MIXTURE FUELED SOLID OXIDE FUEL CELLS WITH GLOBAL REACTION KINETICS

5.1 INTRODUCTION

Solid oxide fuel cells (SOFCs) are energy conversion devices that convert the chemical energy of fuels into electrical energy directly. The widely used SOFC anode material is nickel cermet. The high catalytic property of the nickel anode allows certain degree of internal reforming to occur, enabling direction operations on hydrocarbon fuels such as methane[75]. This capability together with high operating temperatures makes SOFCs the most fuel flexible and efficient energy conversion fuel cell technology[76]. However the hydrocarbon fuels such as natural gas, methane-rich fuels derived from gasified biomass generally have many contaminants, typically sulfur- and carbon-containing compounds[78,101]. These contaminants may lead to sulfur poisoning and carbon deposition of nickel catalyst, and deactivate the function of nickel cermet anode. Therefore significant efforts have been put into the fundamental mechanism understanding of hydrocarbon fueled SOFCs and strategy development to mitigate the anode degradations caused by contaminants.

The issues of carbon deposition and sulfur poison effects on nickel-based anodes

are usually studied individually. For example, direct methane (CH_4) fueled SOFCs are generally employed to investigate carbon deposition effect. This includes experimental studies, e.g., S.A.Barnett et al.[102,103] and modeling studies, e.g.,[74,104,105]. Similarly, H_2S is used as the fuel to investigate the sulfur poisoning effects on the anode. Most of the sulfur poisoning studies are experimental[51,78,106] with a little work being modeling [80,81,107]. In order to simulate the contaminants involved in practical hydrocarbon fuels, the mixture of CH_4 and H_2S are used as the fuel in the experiments for nickel-based anode degradation studies[83,108]. When CH_4-H_2S mixture is used as the fuel for SOFCs, there exist complicated dissociation processes of CH_4 and H_2S respectively, (steam/dry) reforming processes of CH_4, the CH_4 reforming process induced by H_2S, and the steam reforming of intermediate species CO as well as the electrochemical reactions induced by both H_2 and CO. It is in general difficult for experimental methods to interpret the complicated multiphysics processes in the anodes. In this aspect, mathematical modeling technique may provide a cost-effective way to deconvolute the complicated chemical and electrochemical processes. To our best knowledge, the CH_4-H_2S mixture fueled SOFCs have not been investigated through modeling method.

The objective of this study is to develop a SOFC model with CH_4-H_2S mixture as the fuel. The model considers the complicated dissociations and reforming reactions processes. The electrochemical oxidation process of both H_2 and CO are taken into account in the model. The developed model is first validated using experimental data by matching the model predictions with experimental polarization curves. Based on the

validated model, numerical simulations are carried out to study the complicated multi-physics processes in the SOFCs. The carbon deposition and sulfur poisoning issues are also discussed based upon the simulation results.

5.2 CHEMICAL REACTION KINETICS AND ELECTROCHEMICAL REACTIONS

When the mixture of CH_4 and H_2S is used as the fuel, very complicated chemical and electrochemical reaction processes occur in porous nickel cermet anode. These include the dissociations of CH_4 and H_2S, the steaming reforming of CH_4, the CO_2 reforming of CH_4, the H_2S reforming of CH_4, and the carbon monoxide steam reaction [104,108]. The anode also involves the electrochemical oxidations of H_2 and CO. These reactions are summarized in Table 5.1. The corresponding reaction rates and rate constants are shown in Table 5.2. Accordingly the reaction source terms and energy source terms are obtained as shown in Table 5.3.

Table 5.1 Chemical/Electrochemical reactions

	Reactions
Methane dissociation(r_1)	$CH_4 \leftrightarrow C + 2H_2$
Methane steam reforming reaction(r_2)	$CH_4 + H_2O \leftrightarrow 3H_2 + CO$
Methane dry reforming reaction(r_3)	$CH_4 + CO_2 \leftrightarrow 2H_2 + 2CO$
Carbon monoxide steam reaction(r_4)	$CO + H_2O \leftrightarrow H_2 + CO_2$
Hydrogen sulfide dissociation(r_5)	$H_2S \leftrightarrow H_2 + 0.5S_2$
Methane hydrogen sulfide reforming(r_6)	$CH_4 + 2H_2S \leftrightarrow 4H_2 + CS_2$
Electrochemical reaction:	Anode : $H_2 + O^{2-} \leftrightarrow H_2O + 2e^-$, $CO + O^{2-} \leftrightarrow CO_2 + 2e^-$ Cathode: $O_2/2 + 2e^- \leftrightarrow O^{2-}$

For Ni-YSZ composite anode, the Ni phase conducts electrons while the YSZ phase conducts oxygen ions. The electrochemical reactions take place at the triple phase

boundary, where Ni phase, YSZ phase, and gas phase meet together. In principle, various types of electrochemical reactions could occur simultaneously in the anode[84]. Recent results show that only a few of them are rate-dominate steps. In this paper, the H_2-H_2O and CO-CO_2 electro-oxidation pathways are assumed to be the two dominant electrochemical processes.

Table 5.2 Reaction rates and constants

Reaction Rate	Rate Constant
$r_1 = k_{11} \dfrac{p_{CH_4} - \dfrac{p_{H_2}^2}{K_1}}{(1 + k_{12}\sqrt{p_{H_2}})^2}$	$k_{11} = 2.31\times10^{-5} \exp(20.492 - \dfrac{104200}{R_g T})$ $k_{12} = \exp(\dfrac{163200}{R_g T} - 22.426)$ $K_1 = 5.088\times10^{5} \exp(-\dfrac{91200}{R_g T})$
$r_2 = k_{2f}[CH_4][H_2O] - k_{2b}[CO][H_2]^3$	$k_{2f} = 2.3\times10^{-8}$ $\quad k_{2b} = 1.4\times10^{-20}$
$r_3 = \dfrac{K_{31}K_{32}k_3[CH_4][CO]}{K_{31}K_{32}[CH_4][CO_2] + K_{31}[CH_4] + K_{32}k_3[CO_2]}$	$K_{31} = 2.61\times10^{-3} \exp(-\dfrac{4300}{T})$ $K_{32} = 5.71\times10^{-5} \exp(\dfrac{8700}{T})$ $k_3 = 5.35\times10^{-1} \exp(-\dfrac{7500}{T})$
$r_4 = k_{4f}[CO][H_2O] - k_{4b}[CO_2][H_2]$	$k_{4f} = 1.5\times10^{-7}$ $\quad k_{4b} = 1.4\times10^{-7}$
$r_5 = A_{5f} \exp(\dfrac{-E_{5f}}{RT})(p_{H_2S} - \dfrac{p_{H_2}\sqrt{p_{S_2}}}{K_5})$	$A_{5f} = 7.84\times10^{6}$, $E_{5f} = 1.96\times10^{5}$; $K_5 = \sqrt{10^{5} \exp(\dfrac{-184.1\times10^{3}}{2.303RT})}$
$r_6 = A_{6f} \exp(\dfrac{-E_{6f}}{RT})(p_{CH_4} {p_{H_2S}}^2 - \dfrac{{p_{H_2}}^4 p_{CS_2}}{K_6})$	$A_{6f} = 2\times10^{11}$, $E_{6f} = 1.7168\times10^{4}$, $K_6 = \exp(\dfrac{-19.5\times10^{3}}{2.303RT})$

For the hydrogen oxidation process, the local equilibrium potential can be determined by,

$$E_{H_2} = \frac{\Delta G}{zF} + \frac{RT}{2F}\ln(\frac{p_{H_2} p_{O_2}^{0.5}}{p_{H_2O}}) \tag{5.1}$$

where, ΔG is the Gibbs free energy of the reaction, z is the number of electrons, p is the partial pressure, and the local Butler-Volmer equation can be formulated as,

$$i_{an}^{H_2} = z \cdot F \cdot l_{TPB} \cdot i_{0,an}^{H_2}[\exp(\frac{\alpha z F}{RT}(\eta - E_{H_2})) - \exp(-\frac{(1-\alpha)zF}{RT}(\eta - E_{H_2}))] \tag{5.2}$$

where, l_{TPB} is the length of three phase boundary per unit volume, $i_{0,an}^{H_2}$ is the exchange current density and can be formulated as[74],

$$i_{0,an}^{H_2} = i_{H_2}^{*} \frac{(p_{H_2} / p_{H_2}^{*})^{0.25}(p_{H_2O})^{0.75}}{1 + (p_{H_2} / p_{H_2}^{*})^{0.5}} \tag{5.3}$$

where, $p_{H_2}^{*}$ is about 0.7atm; $i_{H_2}^{*}$ is the empirical constant used to fit the model predictions with experimental data.

Table 5.3 Reaction Source terms

Reaction source terms	Energy source terms
$R_{CH_4} = (-r_1 - r_2 - r_3)M_{CH_4}$	$R_{Cathode} = Q_{ohm} + Q_{chem/entropy}$
$R_{H_2} = (2r_1 + 3r_2 + 2r_3)M_{H_2} - i_{0,an}^{H_2} M_{H_2} / 2F$	$R_{Electrolyte} = Q_{ohm}$
$R_{H_2O} = (-r_2 - r_4)M_{H_2O} + i_{0,an}^{H_2} M_{H_2O} / 2F$	$R_{Anode} = Q_{ohm} + Q_{chem/entropy}$
$R_{CO} = (r_2 + 2r_3 + r_4)M_{CO} - i_{0,an}^{CO} M_{CO} / 2F$	$R_{Fuel-channel} = 0$
$R_{CO_2} = (-r_3 + r_4)M_{CO2} + i_{0,an}^{CO} M_{CO_2} / 2F$	
$R_{O_2} = -i_{0,c} M_{O_2} / 4F$	

The oxidation process of carbon monoxide in the anode is quite similar to that of hydrogen[47]. It has been realized that the rate of CO oxidation is about 2~3 times less than that of hydrogen oxidation under the same oxidant partial pressure[109]. Published

studies show that when the rate of CO oxidation reaction is assumed to be three times lower than that of H_2 oxidation, the modeling prediction is able to obtain a good agreement with experimental data[110]. Therefore, in this paper, this assumption is employed to describe CO-CO_2 oxidation reaction in the anode,

$$E_{CO} = \frac{\Delta G}{zF} + \frac{RT}{2F}\ln(\frac{p_{CO}\, p_{O_2}^{0.5}}{p_{CO_2}}) \tag{5.4}$$

$$i_{an}^{CO} = \frac{1}{3} z \cdot F \cdot l_{TPB} \cdot i_{0,an}^{CO}[\exp(\frac{\alpha z F}{RT}(\eta - E_{CO})) - \exp(-\frac{(1-\alpha) z F}{RT}(\eta - E_{CO}))] \tag{5.5}$$

$$i_{0,an}^{CO} = i_{CO}^{*} \frac{(p_{CO} / p_{CO}^{*})^{0.25} (p_{CO_2})^{0.75}}{1 + (p_{CO} / p_{CO}^{*})^{0.5}} \tag{5.6}$$

where, i_{CO}^{*} is the empirical constant. Then, the total exchange current density within the anode is contributed from both H_2-H_2O and CO-CO_2 electro-oxidation processes,

$$i_{an} = i_{an}^{H_2} + i_{an}^{CO} \tag{5.7}$$

At the cathode side, the oxygen diffuses into the porous cathode and reaches triple phase boundary, where the oxygen phase, the electronic conducting phase LSM, and the ionic conducting phase YSZ meet together. The oxygen molecule combines with electrons transported from the LSM, generating oxygen ions. The oxygen ions transport from the cathode side to the anode side through the YSZ phase. Here one step oxygen reduction reaction is assumed to keep the consistence of electrochemical reaction and charge transfer process:

$$\frac{1}{2} O_2 + 2e^{-} \leftrightarrow O^{2-}$$

and the local Butler-Volmer equation can be formulated as,

$$i_{ca} = z \cdot F \cdot l_{TPB} \cdot i_{0,ca}[\exp(\frac{\alpha zF}{RT}(\eta - E_{eq})) - \exp(-\frac{(1-\alpha)zF}{RT}(\eta - E_{eq}))] \tag{5.8}$$

$$i_{0,ca} = i^*_{O_2} \frac{(p_{O_2} / p^*_{O_2})^{0.25}}{1 + (p_{O_2} / p^*_{O_2})^{0.5}} \tag{5.9}$$

where, $p^*_{O_2} = 4.9 \times 10^8 \exp(-2 \times 10^5 / RT)$; $i^*_{O_2}$ is the empirical fitting parameter. E_{eq} is the equilibrium overpotential, e.g., $E_{eq} = 0.75E_{H_2} + 0.25E_{CO}$.

5.3 SOLUTION ALGORITHM AND MODEL VALIDATION

In addition to the global reforming chemistry and electro-oxidation processes, SOFCs also include very complicated transport processes. Figure 5.1 has illustrated the corresponding experimental setup, of which the transport processes include fuel/gas transport in fuel supply tubes and porous electrodes, charge transport through material backbone, as well as heat transfer. The governing equations for these processes are described in chapter 2.

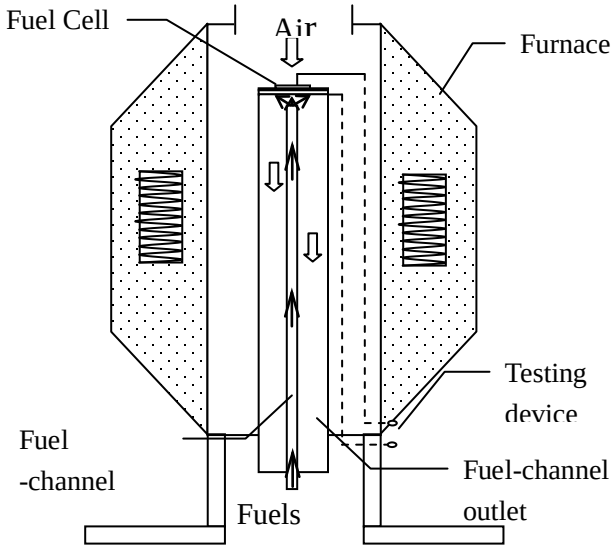

Figure 5.1 SOFC testing system

The mathematical model developed above is solved using the finite element package COMSOL MULTIPHYSICS 4.2a. For a given cell voltage at the cathode

electrode boundary, various charge and species distributions are calculated by combining conservation equations with chemical/electrochemical reactions. The cell average current density is then obtained. By specifying a series of cell voltages and calculating the corresponding average cell current density, we may obtain the polarization curves of the cell, relating the cell voltage to the cell average current density. The species distributions are calculated at each of the individual voltage conditions.

The model is validated using experimental polarization curves, where $10\%CH_4+90\%N_2$ and $5\%H_2S+95\%N_2$ are used as the fuel, and the polarization curves are measured at temperatures of 850°C and 900°C respectively. As shown in Figure 5.2, the model predictions match with experimental data reasonably well. This model is then used for further numerical studies.

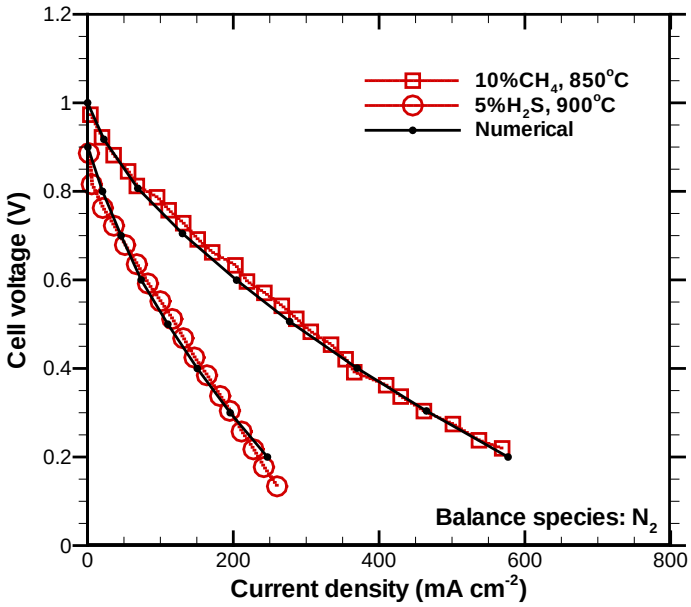

Figure 5.2 Comparison between numerical result and experimental data

5.4 RESULTS AND DISCUSSION

5.4.1 Fuel species distribution

To elucidate the fundamental mechanisms of CH_4-H_2S mixture fueled SOFCs, we first study the gas species distributions in the anode. Here the gas mixture of 40%CH_4, 40%H_2S and 20%N_2 is used as the fuel, the cathode is exposed to the ambient air, the operating temperature of the furnace is controlled at 900^{o}C while the cell voltage is set at 0.2V as an example. Figure 5.3 shows the molar fraction distributions of various fuel/gas species in the button cell and fuel supply system. In the central small tube, the CH_4 and H_2S are relatively uniform. Beyond the outlet of the small tube, the CH_4 and H_2S show relatively high gradients and decrease toward the anode electrode. Due to various chemical/electrochemical reactions, other gas species are also generated, including H_2, H_2O, CO, CO_2, S_2 and CS_2, the detailed distributions are shown in Figure 5.3. The molar

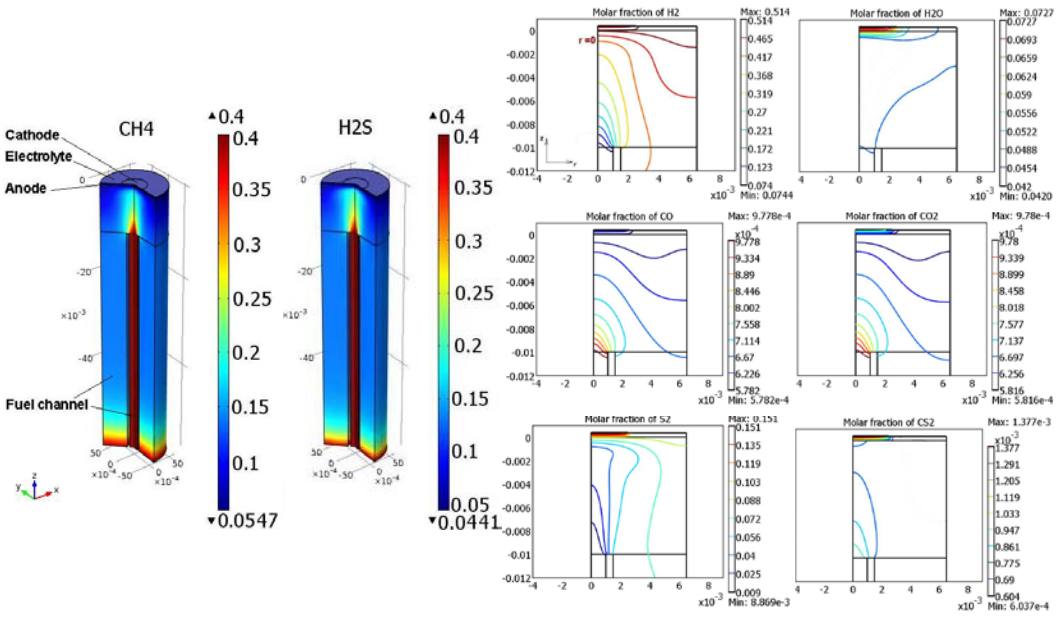

Figure 5.3 The distribution of fuel gas species within the testing system

fractions of H_2, H_2O, and S_2 increase from the outlet of the small supply tube towards the anode, but those of H_2O, and S_2 show relatively high gradients near the channel/electrode interface. The molar fraction of CO decreases from the small tube outlet towards the anode electrode. It is interesting to see that the molar fractions of CO_2 and CS_2 decrease from the small tube outlet toward the channel/anode electrode interface and then increase from the channel/anode interface toward the anode/electrolyte interface.

5.4.2 Effects of operating conditions on local Nernst potentials

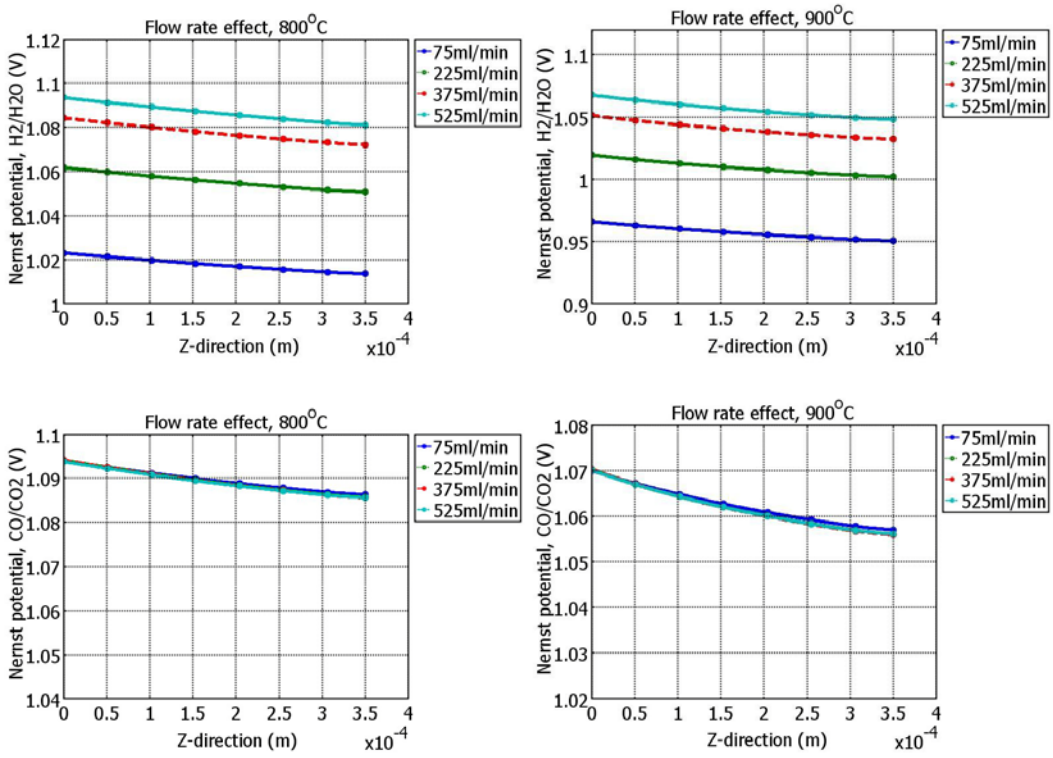

Figure 5.4 The effect of fuel flow rate and operating temperature on the local E_{H2} and E_{CO}

Theoretically, the Nernst potential is the equilibrium reduction potential determining the total electromotive force of the electrochemical process in a fuel cell. In present model, two electro-oxidation processes of H_2-H_2O and CO-CO_2 are considered,

therefore we have two Nernst potentials E_{H2} and E_{CO}. To calculate the E_{H2} and E_{CO}, we use equations (5.1) and (5.4). Here the oxygen partial pressure P_{O_2} is obtained by averaging the P_{O_2} across the entire cathode/electrolyte interface. The partial pressures of other species H_2, H_2O, CO, CO_2 are their local values in the anode electrode. The effects of operating temperature and fuel flow rate on these two Nernst potentials are shown in Figure 5.4. Both E_{H2} and E_{CO} decrease when the operating temperature increases from 800°C to 900°C. The E_{H2} is sensitive to the fuel flow rate, increasing with increasing the fuel flow rate. But E_{CO} shows little sensitivity to the fuel flow rate.

5.4.3 The electronic/ionic current densities

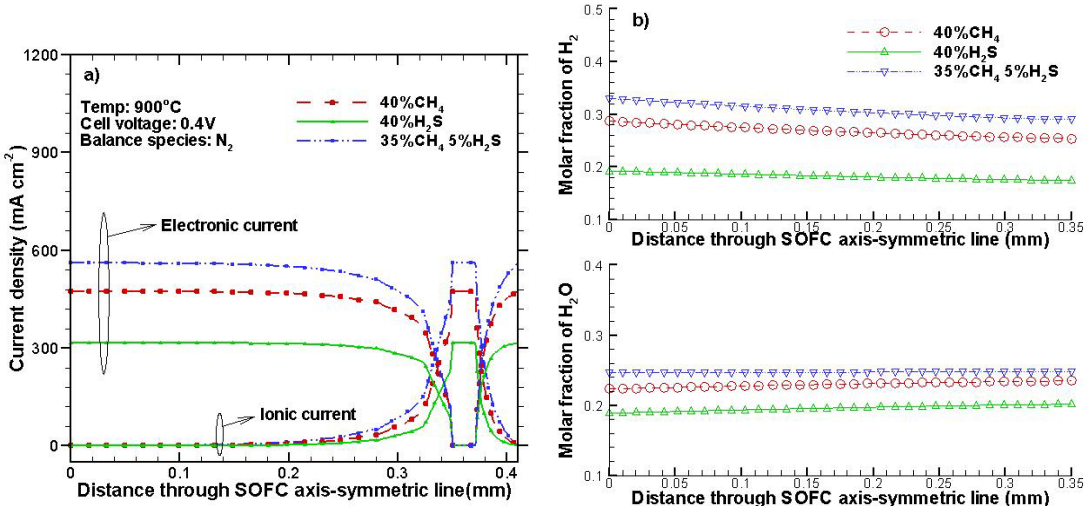

Figure 5.5 Distributions along the cell axis-symmetric line: a) The distribution of electronic/ionic current densities; b) Molar fraction distribution of H_2 and H_2O

To study the effects of fuel composition on the distributions of electronic and ionic current densities, we employ three fuel compositions with N_2 as the gas balance species, i.e., 40%CH_4, 40%H_2S and 35%CH_4+5%H_2S, respectively. The simulations are run at the temperature of 900°C and the cell voltage of 0.4V. For the convenient

illustration, the current density and species distributions along the axis-symmetric line of the cell are utilized. As shown in Figure 5.5a, the electronic current density shows relatively high gradient at the anode/electrolyte interface and is uniform beyond this interface. The ionic current density shows the highest gradient at both the anode/electrolyte interface and cathode/electrolyte interface. Within the electrolyte, the ionic current density is very uniform. Towards the channel/anode interface, the ionic current density approaches zero. When H_2S is used as the fuel ($40\%H_2S+60\%N_2$), the charge (electron/ion) current density is relatively low. When CH_4 is used as the fuel ($40\%CH_4+60\%N_2$), the charge current density is significantly improved. It is interesting to see that the mixed fuel ($35\%CH_4+5\%H_2S+60\%N_2$) may further improve the charge current density. Therefore, the H_2S in hydrocarbon fuels is beneficial to improve SOFC electrochemical performance. Figure 5.5b shows the molar fraction distributions of H_2 and H_2O under different fuel compositions. It is obvious that H_2 and H_2O reach the highest molar fractions when the mixed fuel ($35\%CH_4+5\%H_2S+60\%N_2$) is used for the SOFC. The high molar fraction of H_2 may improve the electrochemical performance. The high molar fraction of H_2O may improve the reforming of CH_4, which in turn improve the production of H_2 and electrochemical performance.

5.4.4 Effects of mixed CH_4-H_2S fuel on local Nernst potentials E_{H2} and E_{CO}

The effects of fuel composition of mixed CH_4-H_2S on local Nernst potential distributions are also studied. The Nernst potential induced by H_2-H_2O electro-oxidation process is denoted as E_{H2}, while that induced by CO-CO_2 electro-oxidation process is

represented by E_{CO}. For the simplicity, the Nernst potential distribution along the axis-symmetric line of the cell is used for the study. As shown in Figure 5.6, the E_{H2} demonstrates a strong correlation with the cell voltage, increasing with increasing the cell voltage from 0.2V to 0.9V. However, the E_{CO} shows a weak dependence on the cell voltage, especially at the anode/electrolyte interface. When the H_2S content in the fuel increases from 5% to 10%, the E_{H2} shows obvious increase particularly at low cell voltage conditions, e.g., 0.6V and 0.2V. The E_{CO} also shows a little bit increase. The corresponding molar fraction distributions of CH_4 and CO are shown in Figure 5.7. When

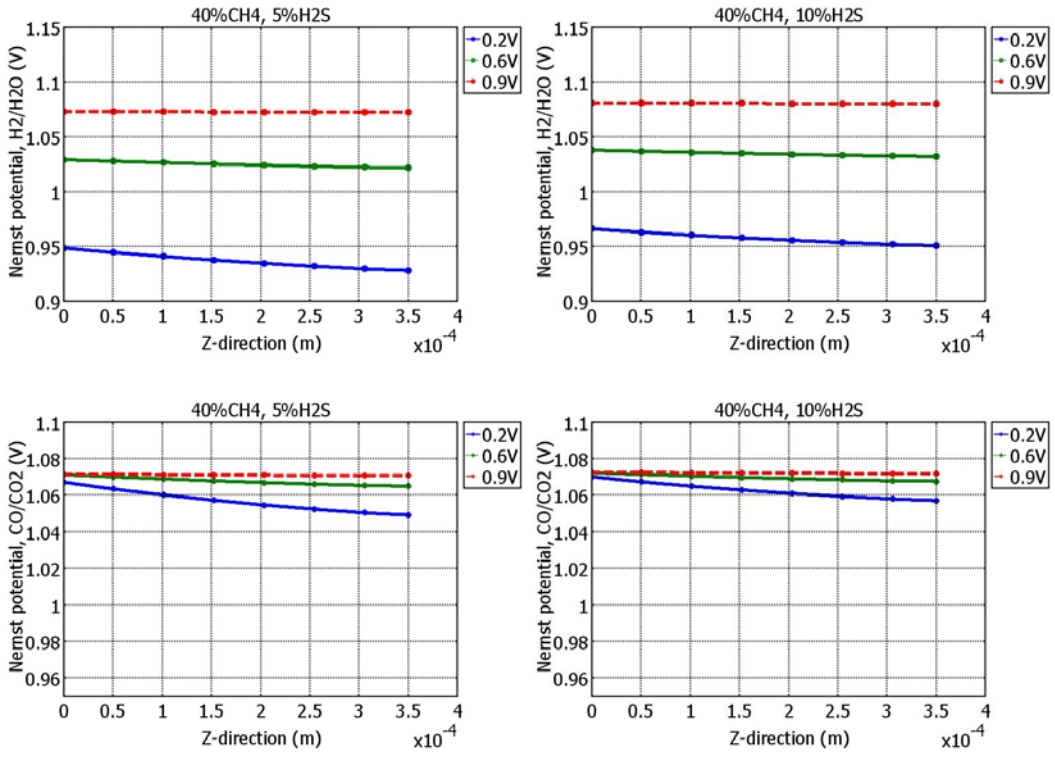

Figure 5.6 The effect of fuel content and operating voltage on the local E_{H2} and E_{CO}

the cell voltage decreases from 0.9V to 0.2V, the molar fraction of CH_4 also decreases, but that of CO increases. The decrease of cell voltage leads to the increase of cell current density, which in turn improves the consumption of species H_2 and CO through

electro-oxidation processes and the dissociation and reforming of CH_4. The net increase of CO is caused by the combinational effects of CH_4 reforming process and CO electro-oxidation process. One also can notice from Figure 5.7 that the molar fraction of CH_4 decreases at every single voltage when the H_2S content increases from 5% to 10%, implying that the consumed CH_4 increases. However the corresponding CO increases, indicating that suitable increasing H_2S content in CH_4 fuel may enhance the fuel conversion from CH_4 to CO.

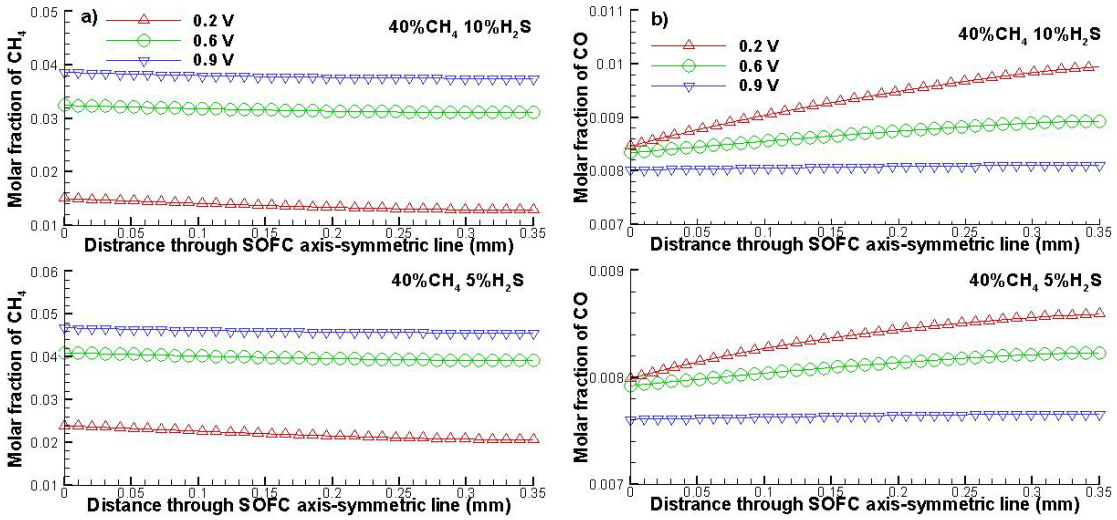

Figure 5.7 Molar fraction distributions of a) CH_4 and b) CO along the SOFC axis-symmetric line

5.4.5 Carbon Deposition and Sulfur Poisoning

The carbon deposition and sulfur poisoning are two major obstacles for hydrocarbon fueled SOFCs with nickel cermet anode. The deposited carbons and/or sulfur may deactivate the catalytic function of nickel[83]. In this section, carbon deposition and sulfur poisoning are studied. Figure 5.8 shows the carbon concentration at the interacting point between cell axial-symmetric line and the anode/electrolyte interface

under different operating conditions. Obviously increasing the operating temperature from 800°C to 900°C, the carbon concentration decreases, suggesting that increasing the temperature may facilitate to mitigate the carbon deposition effects. Similarly increasing

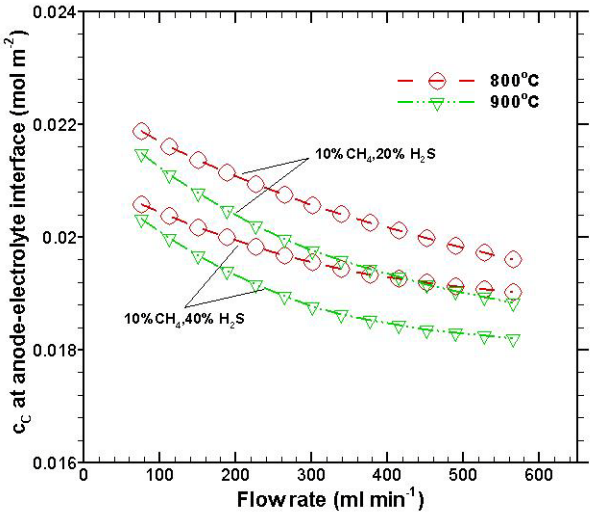

Figure 5.8 The carbon generation under different fuel conditions (The calculation of carbon concentration on the interface is based on matter conservation, $c_C = c^R_{CH4} - c^P_{CH4} - c^P_{CO} - c^P_{CO2}$, R-reactant, P-product)

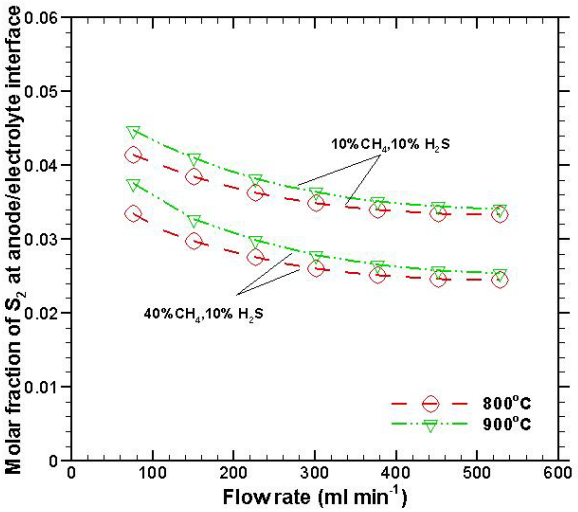

Figure 5.9 The effect of different fuel conditions and operating temperatures on the S_2 production

the flow rate of the fuel may also mitigate carbon deposition effects. When the H_2S content in the fuel increases from 20% to 40%, the carbon concentration is also reduced. Figure 5.9 shows the corresponding S_2 concentration at the intersecting point. Although increasing the fuel flow rate may reduce the generated sulfur concentration, increasing the operating temperature actually improve the sulfur generation. Obviously reducing the H_2S content in the fuel or equivalently increasing the CH_4 content may significantly mitigate the sulfur accumulation. In order to mitigate both the carbon deposition and sulfur poisoning, the feasible way is to increase the flow rate. Other options such as operating temperature and fuel composition show the conflicting roles on mitigating carbon deposition and sulfur poisoning.

5.5 CONCLUSION

The mixture CH_4 and H_2S fueled SOFC model is developed, integrating the detailed global reforming reaction processes and multi-physics transport processes of charge, mass, momentum and energy conservations. The model considers both H_2-H_2O and CO-CO_2 electro-oxidation processes and is validated using the experimental polarization data. Simulation results show that the Nernst potential E_{H2} shows a strong correlation with the cell voltage, increasing with increasing the cell voltage. The E_{CO} shows a weak dependence on the cell voltage, especially at the anode/electrolyte interface. Suitable H_2S in CH_4 fuel is beneficial to improve the reforming of CH_4 and SOFC electrochemical performance particularly H_2-H_2O electro-oxidation process. Increasing the fuel flow rate may mitigate the carbon deposition and sulfur poisoning effects. The

operating temperature and fuel composition show the conflicting roles on mitigating carbon deposition and sulfur poisoning effects. Increasing the temperature may mitigate the carbon deposition effects but potentially worsen the sulfur poisoning effect. Decreasing the H_2S content in the CH_4 fuel may significantly mitigate the sulfur poisoning effect but increase the possibility of carbon deposition effect.

CHAPTER 6

MULTIPHYSICAL MODELING OF HUMIDIFIED HYDROGEN FUELED SOLID OXIDE FUEL CELLS WITH ELEMENTARY REACTION KINETICS

6.1 INTRODUCTION

Solid oxide fuel cell (SOFC) is one of clean energy technologies that can convert the chemical energy of fuels into electricity in a highly efficient and environmentally benign manner[111,112]. The electrochemical reactions at solid/gas interface in porous electrodes play a very important role. Due to very aggressive operating conditions, direct measurement becomes difficult and the modeling technique has been widely used to study the complicated electrochemical reaction processes[113]. Usually, a set of conservation equations are used to describe the processes of heat transfer, fuel/gas species transport, and charge (ion and electron) migration. These processes are coupled together at solid/gas interface through Butler-Volmer equation[114,115]. Since Butler-Volmer equation is only able to consider bulk electrochemical reactions, the detailed interim reaction species, which can improve the underlying mechanism understanding of electrochemical reactions, cannot be captured.

To overcome the limitations of the modeling method mentioned above, elementary reaction kinetic modeling is employed[74,84,85,116]. The elementary reaction

models focus on the description of adsorption/desorption and surface reaction processes taking place at a local point, and is able to provide more precise electrochemical charge-transfer calculation through the balances of reaction species. It is usually assumed that such elementary reactions are identical across the entire porous electrodes. While this assumption can simplify the modeling and related computations, it is not consistent with the fact that the amplitude of such reactions could be different from one reaction site to another due to the limitations of mass transport processes. Therefore, there is a need to integrate the elementary reaction at each individual site with complicated fuel/gas transport processes [117-119].

The objective of this study is to develop a mathematical model that can link the elementary reactions at individual sites and the complicated multiple transport processes in porous electrodes. The model is validated using the experimental data of a button cell. Comprehensive simulation studies are performed to investigate multi-scale interactions of electrochemical elementary reactions and multi-transport processes.

6.2 ELEMENTARY REACTIONS KINETICS

Electrochemical reactions involve multiple steps in the anode and strongly depend on the anode materials. For the Ni-YSZ composite anode, it is generally recognized that the following reaction processes are recognized when hydrogen is used as the fuel [81,85,120,121].

After hydrogen diffuses into porous anode, it interacts with nickel. The hydrogen

can be adsorbed onto the surface of nickel as hydrogen atoms; the adsorbed hydrogen atoms can be desorbed off the nickel surface to form hydrogen molecules, i.e.,

$$H_2 + Ni \Leftrightarrow 2H_{(s)}$$

The reactions in two directions take place simultaneously until an equilibrium state is reached. The equilibrium state is dependent on the local multiple processes and thus the operating conditions of the cell.

At the cathode side, oxygen ions $O^{2-}_{(YSZ)}$ are conducted toward the anode through the oxygen vacancies of electrolyte, e.g.,YSZ,

$$O^{\times}_{(YSZ)} + (YSZ) \Leftrightarrow O^{2-}_{(YSZ)} + V^{\bullet\bullet}_{(YSZ)}$$

Where, $O^{\times}_{(YSZ)}$ is a lattice oxygen in YSZ and $V^{\bullet\bullet}_{(YSZ)}$ is an oxygen vacancy on YSZ surface. At three phase boundary (TPB) site, where nickel and YSZ as well as gas meet together, charge transfer reactions take place and several transfer pathways could occur at this site. It is recognized that incorrect predictions may be given by the two-step charge transfer mechanisms when the anode is polarized at high H_2O partial pressures[85]. Therefore, in the present elementary model a single-step oxygen-spillover process is assumed, i.e.,

$$O^{2-}_{(YSZ)} + Ni \Leftrightarrow O_{(s)} + (YSZ) + 2e^{-}_{(Ni)}$$

Here, the oxygen ions release electrons, forming oxygen atoms adsorbed onto the surface of YSZ. The electrons are released to the electronic conducting phase Ni. When the atomic oxygen $O_{(s)}$ on the surface of YSZ meets the adsorbed atomic hydrogen $H_{(s)}$ on the Ni surface at the TPB site, surface reactions take place. At this stage, there exist three

possible surface reactions: the atomic hydrogen $H_{(s)}$ combines with atomic oxygen $O_{(s)}$, forming adsorbed hydroxyl $OH_{(s)}$; the hydroxyls may combine together to form water molecule and atomic oxygen; the $OH_{(s)}$ may further react with atomic hydrogen $H_{(s)}$ to form adsorbed water molecule,

$$H_{(s)} + O_{(s)} \Leftrightarrow OH_{(s)}$$

$$OH_{(s)} + OH_{(s)} \Leftrightarrow O_{(s)} + H_2O_{(s)}$$

$$OH_{(s)} + H_{(s)} \Leftrightarrow H_2O_{(s)}$$

In addition, the steam may also experience the adsorption/desorption processes on the surface of Ni,

$$H_2O + Ni_{(s)} \Leftrightarrow H_2O_{(s)}$$

Table 6.1 summarizes the elementary reactions in Ni/YSZ composite anode. The electrochemical reactions in the anode can be represented with a generic formula [115],

$$\sum_i^n n_i Ra_i \leftrightarrow \sum_j^m m_j Pu_j + ze^- \tag{6.1}$$

where Ra is the reactant, Pu is the product, n_i and m_j are the stoichiometric factors for the reactants and products, respectively, z is the number of electrons. Using Arrhenius formula, the forward and backward reaction rate coefficient k_f and k_b can be calculated as [74,116],

$$k_f = AT^n \exp(\frac{-E^{act}}{RT}) \exp(\alpha \frac{zF}{RT} \eta) \tag{6.2}$$

$$k_b = AT^n \exp(\frac{-E^{act}}{RT}) \exp(-(1-\alpha) \frac{zF}{RT} \eta) \tag{6.3}$$

where E^{act} is the thermal activation energy, η is the electrical potential difference

between the reactants and products. The net reaction rate R_n can be determined as,

$$R_n = k_f \prod_i [Ra_i]^{n_i} - k_b \prod_j [Pu_j]^{m_j} \tag{6.4}$$

Then the elementary kinetic description of charge transfer can be formulated as,

$$i_{F,an} = Fl_{TPB} \sum zR_n \tag{6.5}$$

Where, $i_{F,an}$ is the faradic current in the anode; l_{TPB} is the TPB length of the composite anode. Because the electroactive species involved in the charge-transfer reactions are surface-adsorbed intermediates, to study their variations of spatial distribution, the surface coverage θ_i s are calculated through the surface diffusion process [85,119],

$$\frac{\sigma_i^{surf}}{\Gamma} R_i = -\nabla \bullet (D_i^{surf} \nabla \theta_i), \quad \theta_i = \frac{\sigma_i^{surf} c_i}{\Gamma} \tag{6.6}$$

Where, σ_i^{surf} is the number of surface sites occupied by species i; Γ is the area-specific density of adsorption site (mol/cm^2); D_i^{surf} is the surface diffusivity of species i; c_i is the concentration of surface species i. The elementary reactions are influenced by the local species concentrations through surface diffusion process, and the species concentrations are influenced by not only the local elementary reactions but also the complicated transport processes in porous electrodes. To study these coupling effects, the elementary reactions are linked to macro-scale transport processes.

Since the cathode has much simple elementary reaction steps, the equation from[74] is used to describe the oxygen reduction process,

$$i_{F,ca} = i_{ca}^* \frac{(p_{O2} / p_{O2}^0)^{0.25}}{1 + (p_{O2} / p_{O2}^0)^{0.5}} (\exp(\frac{0.5F\eta_{act}}{RT}) - \exp(-\frac{0.5F\eta_{act}}{RT})) \tag{6.7}$$

where, i_{ca}^* is a free parameter used to fit the model predictions with experimental data;

$p_{O2}^0 = 4.9\times10^8 \exp(-2\times10^5 / RT)$; p_{O2} is the partial pressure of local oxygen; η_{act} is the activation overpotential $\eta_{act} = \eta - \eta_{eq}$, and η_{eq} can be determined using the reactants and products of elementary reactions,

$$\eta_{eq} = \frac{\Delta G}{zF} + \frac{RT}{zF}\ln(\frac{\prod_j [Pu_j]^{m_j}}{\prod_i [Ra_i]^{n_i}}) \tag{6.8}$$

here, ΔG is the Gibbs free energy of the reaction. Considering that the hydrogen electro-oxidation pathway is dominant, the equation (6.8) can be simplified as,

$$\eta_{eq} = E^0 + \frac{RT}{2F}\ln(\frac{p_{H_2} p_{O_2}^{0.5}}{p_{H_2O}}) \tag{6.9}$$

Table 6.1 H2/H2O Surface reaction mechanism

Ni – surface		A	n	E
Adsorption/Desorption($f;b$)				
1	$H_2 + Ni(s) + Ni(s) \Leftrightarrow H(s) + H(s)$	10^{-2} ; 5.593×10^{19}	0 ; 0	0 ; 88.12
2	$H_2O + Ni(s) \Leftrightarrow H_2O(s)$	1×10^{-1} ; 4.579×10^{12}	0 ; 0	0 ; 62.68
Surface Reactions				
3	$O(s) + H(s) \Leftrightarrow OH(s) + Ni(s)$	5×10^{22} ; 2.005×10^{21}	0 ; 0	97.9 ; 37.19
4	$OH(s) + H(s) \Leftrightarrow H_2O(s) + Ni(s)$	3×10^{20} ; 2.175×10^{21}	0 ; 0	42.7 ; 91.36
5	$OH(s) + OH(s) \Leftrightarrow O(s) + H_2O(s)$	3×10^{21} ; 5.423×10^{23}	0 ; 0	100 ; 209.37
Ni/YSZ- Surface (Charge transfer reactions)		A^0	α	E
6	$O^{\times}(YSZ)+(YSZ) \Leftrightarrow O^{2-}(YSZ)+V^{\bullet\bullet}(YSZ)$	1.6×10^{22}	0	90.9
7	$O^{2-}(YSZ)+Ni(s) \Leftrightarrow O(s)+(YSZ)+2e^-(Ni)$	4.9×10^{-6}	0.5	c
Rate constant of Arrhenius equation written as: $k = AT^n\exp(-E/RT)$, the unit of E is kJ/mol. c - Calculated or estimated from references.				

6.3 SOLUTION ALGORITHM AND MODEL VALIDATION

In addition to the surface chemistry and electro-oxidation processes, SOFCs also include very complicated transport processes. Figure 6.1 has illustrated the corresponding experimental setup, of which the transport processes include fuel/gas transport in fuel supply tubes and porous electrodes, charge transport through material backbone, as well as heat transfer. The governing equations for these processes are described in chapter 2.

Table 6.2 Reaction rates and source terms

Reaction rate	Reaction source term	Energy source term
$r_1 = k_{1,f}[H_2] - k_{1,b}[H(s)]^2$ $r_2 = k_{2,f}[H_2O] - k_{2,b}[H_2O(s)]$ $r_3 = k_{3,f}[H(s)][O(s)] - k_{3,b}[OH(s)]$ $r_4 = k_{4,f}[OH(s)][H(s)] - k_{4,b}[H_2O(s)]$ $r_5 = k_{5,f}[OH(s)]^2 - k_{5,b}[O(s)][H_2O(s)]$	$R_{H_2} = -r_1$ $R_{H_2O} = -r_2$ $R_{H(s)} = 2r_1 - r_3 - r_4$ $R_{OH(s)} = r_3 - r_4 - 2r_5$ $R_{H2O(s)} = r_1 - r_4 + r_5$	$R_{Ca} = Q_{ohm} + Q_{elec/chem}$ $R_{El} = Q_{ohm}$ $R_{An} = Q_{ohm} + Q_{elec/chem}$ $R_{Cl} = 0$

The mathematical model is solved using COMSOL MULTIPHSICS V4.0. The model parameters and boundary conditions are provided in Table 6.3 and Table 6.4 respectively. For a specified cell voltage at the cathode electrode boundary, the distributions of various parameters are calculated. Accordingly, the average cell current

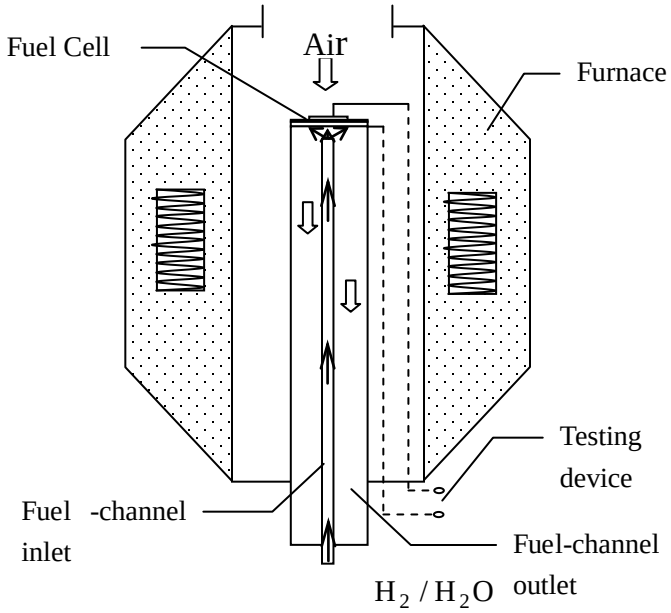

Figure 6.1 Experimental testing system

density is obtained. The cell polarization curve is then obtained by specifying a series of cell voltages and calculating the corresponding average cell current density. And the

species associated with multi-physicochemical processes are calculated at each of the specified voltage conditions.

Table 6.3 Operation parameters

	Value	Units
Cathode layer thickness, radius	4×10^{-5}, 2.5×10^{-3}	m
Electrolyte layer thickness, radius	2×10^{-5}, 6.5×10^{-3}	m
Anode layer thickness, radius	3.5×10^{-4}, 6.5×10^{-3}	m
Inlet fuel channel radius, wall radius	1×10^{-3}, 1.5×10^{-3}	m
Outlet fuel channel radius	6.5×10^{-3}	m
Faraday Constant	96500	$C\cdot mol^{-1}$
Gas constant	8.314	$J\cdot mol^{-1}K^{-1}$
Operating Temperature	700	^{o}C
Pressure	1	atm
Anode ionic conductivity	$3.34\times10^{4}\exp(-10300/T)$	$S\cdot m^{-1}$
Cathode ionic conductivity	$3.34\times10^{4}\exp(-10300/T)$	$S\cdot m^{-1}$
Anode electronic conductivity	2×10^{6}	$S\cdot m^{-1}$
Cathode electronic conductivity	$42\times10^{6}\exp(-1150/T)/T$	$S\cdot m^{-1}$
Electrolyte ionic conductivity	$3.34\times10^{4}\exp(-10300/T)$	$S\cdot m^{-1}$
Porosity(ε)	0.4	1
Particle diameter	2×10^{-6}	m
Tortuosity	$(\frac{3-\varepsilon}{2})^{0.5}$	1
Permeability	$\frac{\varepsilon^{3}d^{2}}{150(1-\varepsilon)^{2}}$	1
Inlet velocity	0.2	$m\cdot s^{-1}$
Surface site density of Ni	6.1×10^{-9}	$mol\cdot cm^{-2}$
Specific three-phase boundary length	1.8×10^{12}	$m\cdot m^{-3}$

The model is validated using experimental polarization curves, where the humidified hydrogen (97% hydrogen and 3% vapor) is used as the fuel and ambient oxygen is used as the oxidant. The cell polarization is obtained at three temperature conditions of 600^{o}C, 650^{o}C and 700^{o}C. As shown in Figure 6.2, the model predictions match with experimental data reasonably well. The validated model is then used for

further simulation studies.

Table 6.3 Boundary conditions

Interfaces(Ω)	$\Omega_{Ca/Cl}$	$\Omega_{Ca/El}$	$\Omega_{El/An}$	$\Omega_{An/Cl}$	Ω_{Cl}
Ionic charge	Insulation	Continuity	Continuity	Insulation	N/A
Electronic charge	Specified voltage	Insulation	Insulation	0	N/A
Mass	O_2/N_2 (Mass fractions)	Insulation	Insulation	Continuity	H_2/H_2O (Mass fraction)
Momentum	Pressure	Wall (no slip)	Wall (no slip)	Continuity	Flow rate, pressure
Energy	Temperature	Continuity	Continuity	Continuity	Temperature

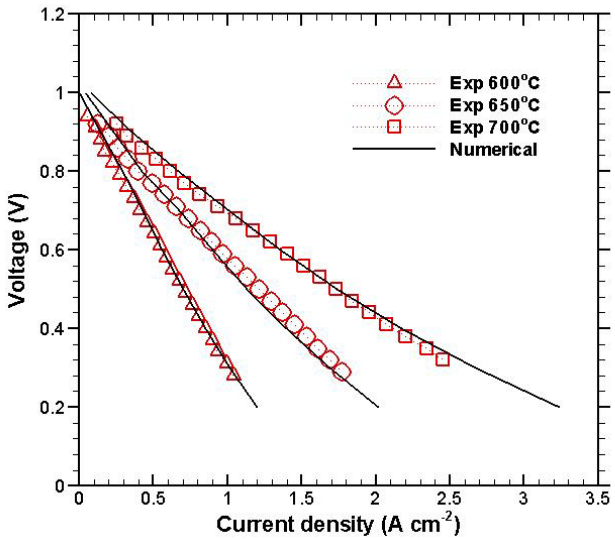

Figure 6.2 Comparisons between experimental and numerical data

6.4 RESULTS AND DISCUSSIONS

6.4.1 Distributions of fuel/gas and local potential/current

Figure 6.3 shows the molar fraction distributions of hydrogen, vapor, and oxygen. The hydrogen shows little variation in fuel supply tube, but decreases in the

anode toward the anode/electrolyte interface. The variation is well aligned with the size of the cathode. The vapor shows opposite trend and increases toward the anode/electrolyte interface. These distributions are due to the fact that the electrochemical reactions in the anode consume hydrogen while producing water molecules. Similarly, on the cathode side, the molar fraction of oxygen shows a slight decrease toward the cathode/electrolyte interface, in which the oxygen is consumed by electrochemical reactions.

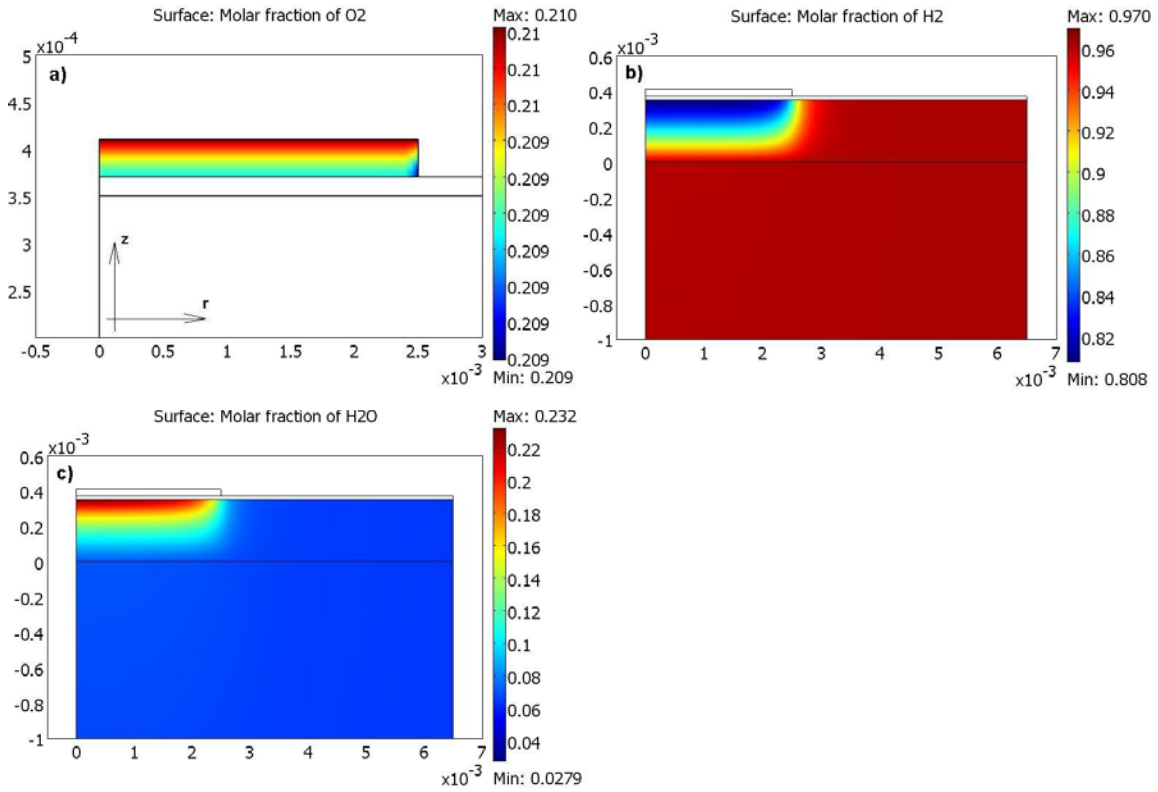

Figure 6.3 The molar fraction distribution of bulk gas species within electrodes: a) Oxygen, b) Hydrogen and c) Steam

To study the spatial effects of cell polarization performance, the electrical/ionic potentials and ionic current distribution are examined along the axis-symmetric line. As

shown in Figure 6.4a, when the cell voltage is set at 0.5V, the electrical potential of the cathode and anode remains at 0.5V and 0V respectively and doesn't show any gradient along the axial-symmetric line. The ionic potential is about 0.5V in the anode and approaches to zero in the cathode. Obvious gradients of ionic potential exist across the electrolyte. The current distribution along the axial-symmetric line is shown in Figure 6.4b. Clearly the ionic current reaches the highest value within the electrolyte, which is consistent with ionic potential distributions. This observation suggests that the electrochemical reactions mainly occur near the electrode/electrolyte interface. When the specified cell voltage increases to 1V, the corresponding ionic current distribution significantly decreases as shown in Figure 6.4b.

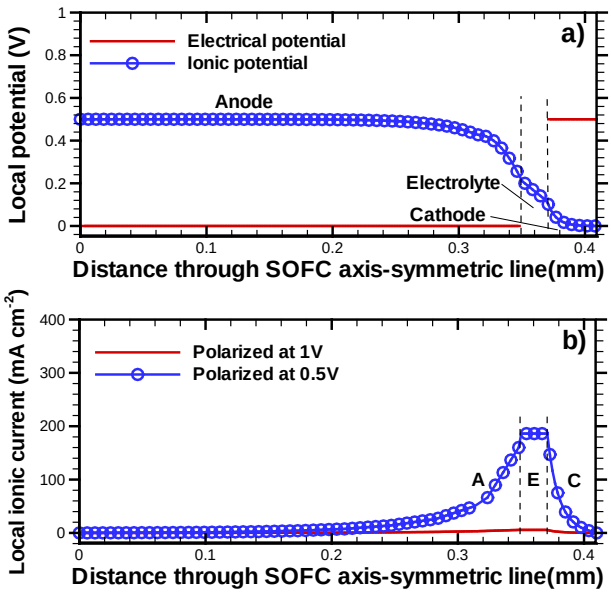

Figure 6.4 The distribution of local potential and current along cell axis-symmetric line: a) local potential, b) local ionic current

6.4.2 Surface species distribution within the anode

The adsorbed surface species such as O(s), H(s), OH(s), H_2O(s) are very

important intermediate products influencing the electrochemical reactions at TPB sites in the anode. As shown in Figure 6.5, the concentration of species H(s) increases from the

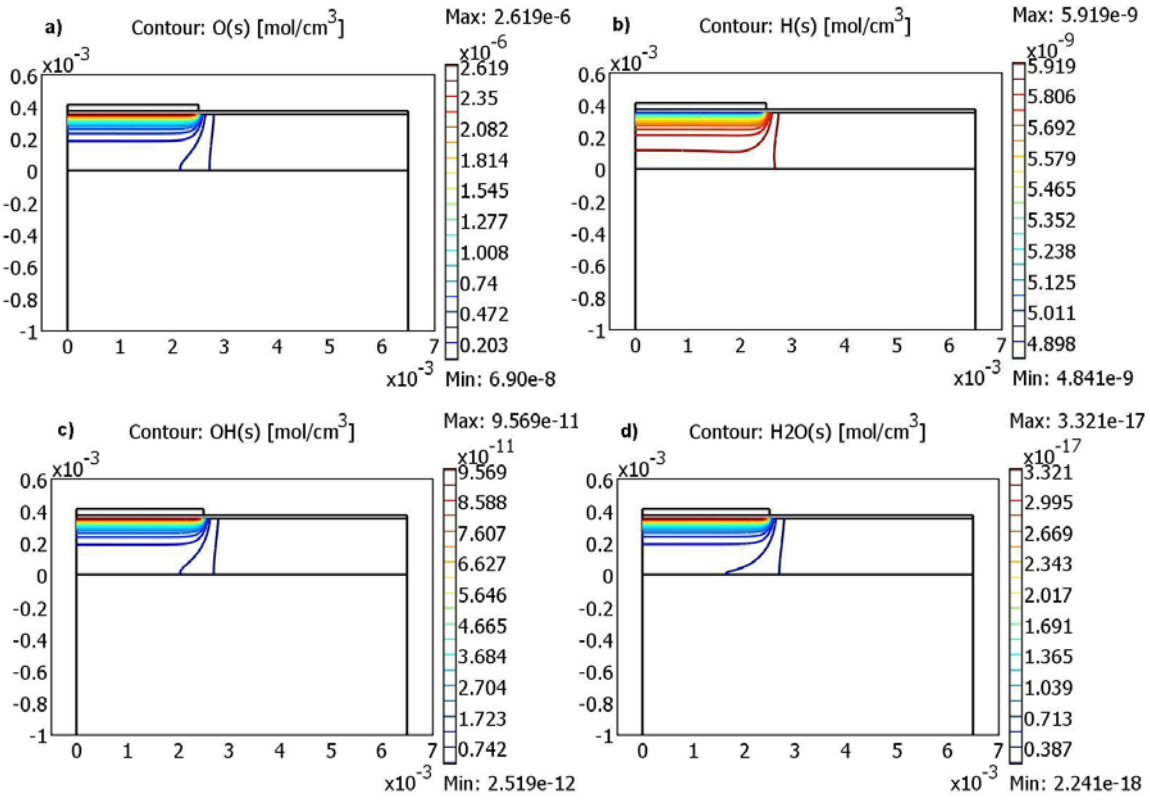

Figure 6.5 The concentration distribution of adsorbed surface species within the anode: a) O(s), b) H(s), c) OH(s), and d) H_2O(s)

electrolyte/anode interface toward the anode/channel interface, while the concentrations of other species, e.g., O(s), OH(s), H2O(s), decrease. One may also notice that the concentration of species H(s) is relatively uniform within the anode, however, those of the species O(s), OH(s), H2O(s) show relatively large gradients with the highest concentrations at the electrolyte/anode interface. It is generally recognized that Ni is a very active catalyst and uniformly distributed within the composite anode. As a result, the H(s) ions are generated throughout the entire anode, leading to the relatively uniform

distribution of species H(s). The species O(s) is generated from O^{2-}(YSZ) ions conducted from the cathode side. The species O(s) is consumed at the anode/electrolyte interface and keeps being consumed within the anode, resulting in the spatial concentration decrease from the anode/electrolyte interface toward the anode/channel interface. The OH(s) ions and H_2O(s) ions have much lower concentrations compared with those of O(s) and H(s) ions, and their high concentrations occur in the area close to the anode/electrolyte interface. These observations suggest that most of the surface reactions take place around the anode/electrolyte interface where O(s) shows the highest concentration.

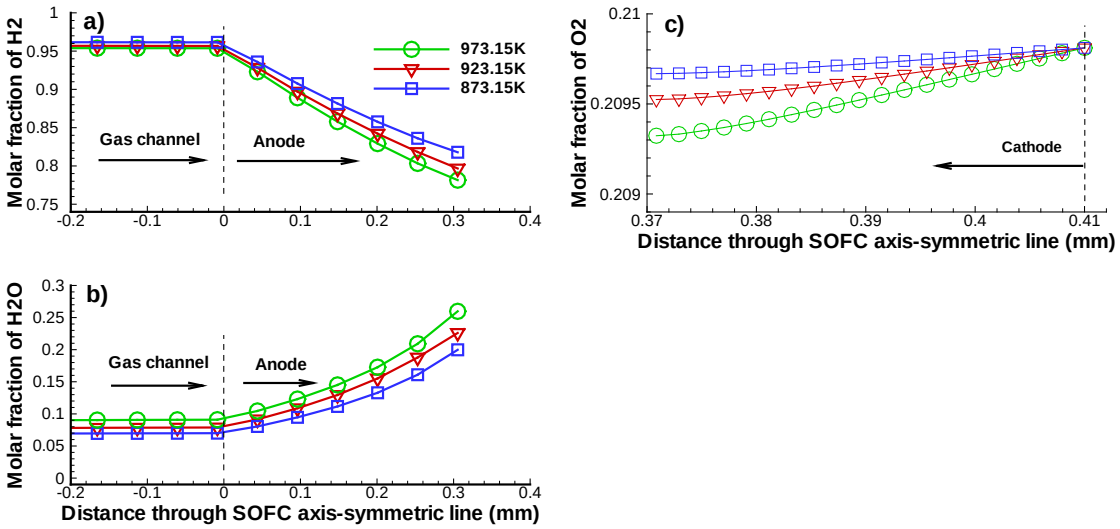

Figure 6.6 Effects of operating temperature on the bulk fuel species distribution along cell axis-symmetric line: a) Hydrogen, b) Steam, and c) Oxygen

6.4.3 Effects of operating temperatures

Experimental results show that the cell performance is significantly affected by the operating temperatures (Figure 6.3). To study the corresponding species transport processes under different operating temperatures, the modeling analysis is further

performed. Figure 6.6 shows the distributions of fuel/gas along the axial-symmetrical line of the cell at temperature 873K, 923K, 973K, respectively. Essentially, the molar fraction of hydrogen and oxygen decreases from the channel/electrode interface toward the electrolyte/electrode interface. The corresponding gradient of hydrogen and oxygen molar fractions increases with increasing operating temperature, indicating that more hydrogen and oxygen are consumed in higher operating temperatures. On the other hand, the vapor (H_2O) generated in the anode shows opposite trend to those of hydrogen and oxygen, and the production of H_2O increases with increasing the operating temperature.

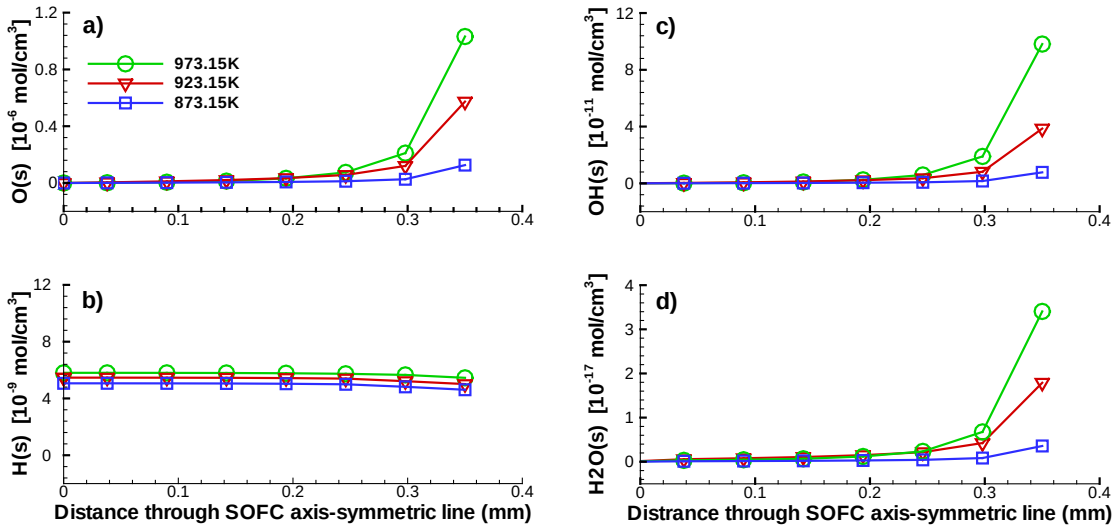

Figure 6.7 Effects of operating temperature on the adsorbed species along cell axis-symmetric line: a) O(s), b) H(s), c) OH(s), and d) H_2O(s)

Figure 6.7 shows the distributions of adsorbed surface species within the anode along the axial-symmetrical line of the cell at temperature 873K, 923K, 973K, respectively. The species H(s) ion shows relatively uniform distribution and a slight variation under different temperatures. The contribution distributions of other three

species O(s) ion, OH(s) ion, and H_2O(s) ion are very low but increase significantly approaching the anode/electrolyte interface, and increase with increasing the operating temperatures. These observations again indicate that the electrochemical reactions in the anode mainly take place near the anode/electrolyte interface, even though the composite anode is employed. One also can see that the concentrations of involved OH(s) ions and H_2O(s) ions are much lower than those of H(s) ions and O(s) ions.

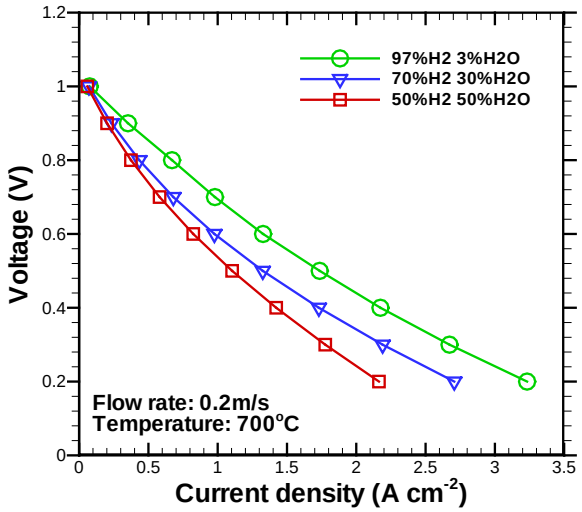

Figure 6.8 Effects of fuel compositions on the cell performance

6.4.4 Effects of fuel compositions

The effects of fuel composition on SOFC performance have been widely investigated through modeling techniques in open literatures, however the elementary reactions are generally neglected. As a result, the adsorbed surface intermediates are not considered. In this section, the surface electrochemistry details are further studied. Figure 6.8 shows the polarization performance of the cell under different fuel composition conditions. Obviously, larger hydrogen fraction in fuel supply leads to

better cell performance. Figure 6.9 shows the corresponding distributions of adsorbates along the axial-symmetrical line of the cell. Basically, the adsorbed H(s) ions increase with increasing hydrogen fraction in the fuel, and are relatively uniform. The adsorbed species O(s) increases near the anode/electrolyte interface with increasing hydrogen fraction in the fuel, while the adsorbed species of both OH(s) ion and H_2O(s) decrease. When hydrogen fraction in the fuel is low, less H(s) ions are generated. This leads to low chemical potential for O(s) production. As a result, the electrochemical reaction rate reduces and the cell performance decreases. On the other hand, when more H_2O(s) and OH(s) ions are generated by higher bulk H_2O concentration, it can raise the backward rate of surface chemical reactions. Accordingly the electrochemical reaction rate will also reduce. Therefore, the effect of fuel composition on cell performance depends on not only the reactant fuels but also the product species generated.

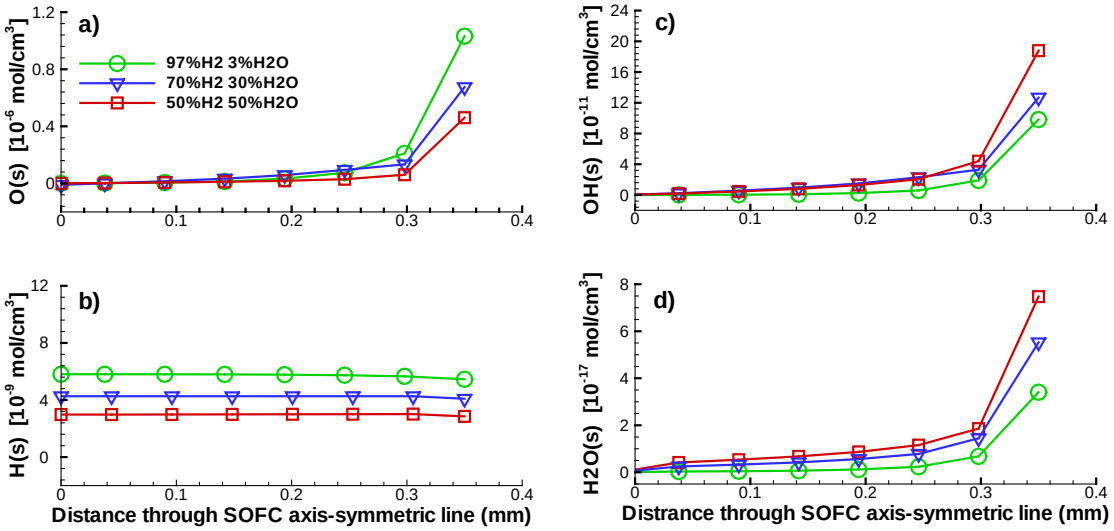

Figure 6.9 Effects of fuel composition on the adsorbed species along cell axis-symmetric line: a) O(s), b) H(s), c) OH(s), and d) H_2O(s)

To study the sensitivity of the generated intermediate species and other cell

parameters with respect to the variations of supplied hydrogen and oxygen, the simulations are run by adding 1% more hydrogen and oxygen to the anode and cathode respectively. Figure 6.10 shows the corresponding variations of various parameters at the anode/electrolyte interface. It is clearly seen that the surface adsorbed species O(s), H_2O(s), and OH(s) ions are very sensitive to the composition changes of fuel/gas. This result indicates that increasing fuel/gas concentrations can effectively improve the chemical potentials for the surface intermediate species productions and surface electrochemical reactions.

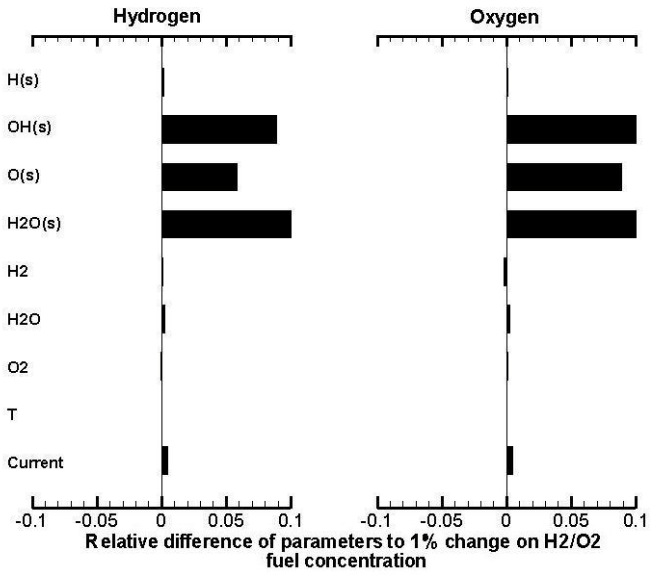

Figure 6.10 Sensitivity of species and cell parameters with respect to fuel compositions. The parameter values are recorded at the intersecting point between electrode/electrolyte interface and cell axial-symmetric line

6.4.5 Effects of cell voltage

The sensitivities of various parameters with respect to the variation of cell voltage are also studied. Figure 6.11 shows parameter variations at the anode/electrolyte interface when the cell voltage increases from 0.2V, 0.5V, and 0.8V to 0.21V, 0.51V, and

0.81V respectively. The cell current and three adsorbed surface species O(s), H_2O(s), and OH(s) ions demonstrate relatively high sensitivities among various parameters. The adsorbed surface species H(s) and the bulk H_2 and H_2O show slight variations. The variations of bulk O_2 and the cell temperature are negligible. One may also see that relatively high sensitivity is obtained at cell voltage 0.8V, particularly for adsorbed surface species OH(s) and H_2O(s). At high cell voltage conditions, the consumed hydrogen and oxygen are low. As a result, their concentrations are maintained at relatively high level. Accordingly, high chemical potentials are generated for adsorbate productions.

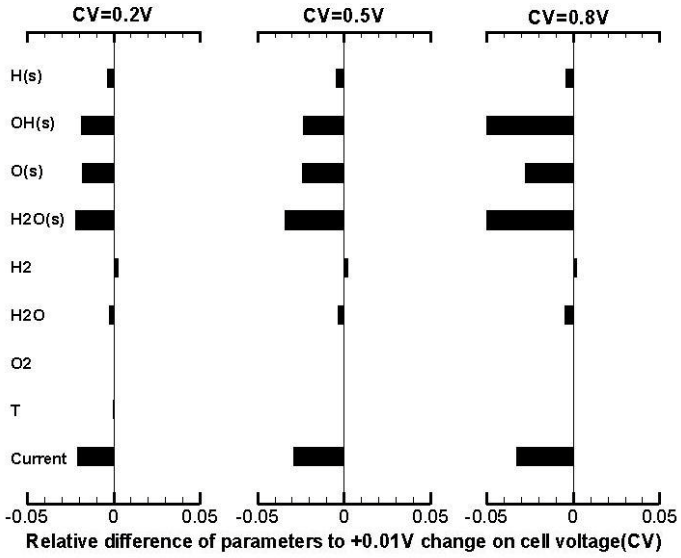

Figure 6.11 Sensitivity of species and cell parameters with respect to cell voltages. The parameter values are recorded at the intersecting point between electrode/electrolyte interface and cell axial-symmetric line

6.5 CONCLUSION

A 2D-axial-symmetrical SOFC model is developed using an anode supported Ni-YSZ/YSZ/LSM button cell test system as the physical base, in which the humidified

hydrogen is used as the fuel and ambient air as the oxidant. The model considers the elementary reactions at TPB sites in the anode and multiple transport processes. The elementary reactions are linked with multi-transport processes in a coherent way. The model is validated with experimental data. Simulation results indicate that very complicated interactions exist among fuel/gas transport in porous electrodes, adsorbed/desorbed species on the surface of porous electrodes, and charge transport through solid backbone, as well as elementary reactions. The concentrations of surface adsorbed species of O(s), OH(s) and H_2O(s) ions presented at the anode/electrolyte interface are relatively high, while that of H(s) ion is relatively uniform within the entire anode. With increasing the operating temperature, the concentrations of surface adsorbed O(s), OH(s) and H_2O(s) ions at the anode/electrolyte interface are significantly improved, while the H(s) ion is slightly influenced. The adsorbed surface species O(s), OH(s) and H_2O(s) ions are very sensitive to the variations of the supplied hydrogen and oxygen as well as the cell voltage.

CHAPTER 7

MULTIPHYSICAL MODELING OF DIRECT METHANE FUELED SOLID OXIDE FUEL CELLS WITH ELEMENTARY REACTION KINETICS

7.1 INTRODUCTION

Solid oxide fuel cells (SOFCs) are fuel flexible, which can operate on not only hydrogen but also hydrocarbon fuels[75]. The high temperature operating condition together with hydrocarbon fuel may lead to very complicated reforming and electrochemical oxidation processes within the anode[76]. One problem with nickel based anode is that the carbon deposition on the nickel surface could quickly weaken the catalytic function of the nickel and deteriorate the function of anodic electrode[122]. There have been significant efforts toward the fundamental mechanism understanding of carbon deposition process and the development of mitigation strategy. In this respect, mathematical modeling plays an important role as a cost-effective technique.

There are a few modeling studies regarding the direct methane fueled SOFCs[104,123,124]. One common assumption in these studies is that the chemical reaction processes only take place in bulk gas species, while the adsorbed species on the electrode surface and the corresponding surface reactions are neglected. To overcome these limitations, surface chemical kinetic modeling approach has been developed recently by

Bessler et al. [64,84,85,119] and Kee et al.[74,125] to describe the detailed surface chemistry. Such models focus on the description of adsorption/desorption and surface reaction processes, and can provide more precise simulations of surface chemical reactions. Toward the better understanding of the interactions between transport processes and surface chemical reactions and their effects on SOFC performance, Janardhanan and Deutschmann[126] presented an isothermal CFD analysis of an anode-supported SOFC button cell, in which the elementary surface reactions were coupled with fluid flow and mass transport processes. Goldin et al.[127] studied a multidimensional non-isothermal modeling of hydrocarbon fueled SOFC button cell with relatively comprehensive coupling between bulk transport processes and surface chemistry, in which the effects of different operating conditions on the cell performance were investigated. All of these researches represent significant progresses toward the modeling of hydrocarbon-fueled SOFCs.

Built upon the above progresses of SOFC modeling in open literature, the objective of this research is to further improve hydrocarbon fueled SOFC model by taking both H_2-H_2O and CO-CO_2 electro-oxidation processes into account and incorporating these two electro-oxidation processes into the complicated coupling between bulk transport processes, diffusion processes, and surface chemical processes. A button cell test system is used as the physical base for the model development and the corresponding experimental data is utilized to validate the model. Upon the model validation, extensive simulations are performed to elucidate the complicated interactions

between transport processes and surface reactions as well as their effects on the cell performance with emphasis on surface reaction processes under practical button cell operating conditions. The different roles and relative importance of various surface chemical kinetic and electro-oxidation processes are studied through sensitivity analysis.

Table 7.1 Surface reaction mechanism of methane

Anode surface(Ni/YSZ)		A	n	E
	Adsorption/Desorption($f;b$)			
1	$H_2 + Ni(s) + Ni(s) \Leftrightarrow H(s) + H(s)$	10^{-2} ; 5.593×10^{19}	0 ; 0	0 ; 88.12
2	$O_2 + Ni(s) + Ni(s) \Leftrightarrow O(s) + O(s)$	10^{-2} ; 2.508×10^{23}	0 ; 0	0 ; 470.39
3	$CH_4 + Ni(s) \Leftrightarrow CH_4(s)$	8×10^{-3} ; 5.302×10^{15}	0 ; 0	0 ; 33.15
4	$H_2O + Ni(s) \Leftrightarrow H_2O(s)$	1×10^{-1} ; 4.579×10^{12}	0 ; 0	0 ; 62.68
5	$CO_2 + Ni(s) \Leftrightarrow CO_2(s)$	1×10^{-5} ; 9.334×10^{7}	0 ; 0	0 ; 28.80
6	$CO + Ni(s) \Leftrightarrow CO(s)$	5×10^{-1} ; 4.041×10^{11}	0 ; 0	0 ; 112.85
	Surface Reactions			
7	$O(s) + H(s) \Leftrightarrow OH(s) + Ni(s)$	5×10^{22} ; 2.005×10^{21}	0 ; 0	97.9 ; 37.19
8	$OH(s) + H(s) \Leftrightarrow H_2O(s) + Ni(s)$	3×10^{20} ; 2.175×10^{21}	0 ; 0	42.7 ; 91.36
9	$OH(s) + OH(s) \Leftrightarrow O(s) + H_2O(s)$	3×10^{21} ; 5.423×10^{23}	0 ; 0	100 ; 209.37
10	$O(s) + C(s) \Leftrightarrow CO(s) + Ni(s)$	5.2×10^{23} ; 1.418×10^{22}	0 ; −3	148.1 ; 115.97
11	$O(s) + CO(s) \Leftrightarrow CO_2(s) + Ni(s)$	2×10^{19} ; 3.214×10^{23}	0 ; −1	123.6 ; 86.5
12	$HCO(s) + Ni(s) \Leftrightarrow CO(s) + H(s)$	3.7×10^{21} ; 2.338×10^{20}	0 ; −1	0 ; 127.98
13	$HCO(s) + Ni(s) \Leftrightarrow O(s) + CH(s)$	3.7×10^{24} ; 7.914×10^{20}	-3 ; 0	95.8 ; 114.22
14	$CH_4(s) + Ni(s) \Leftrightarrow CH_3(s) + H(s)$	3.7×10^{21} ; 4.438×10^{21}	0 ; 0	57.7 ; 58.83
15	$CH_3(s) + Ni(s) \Leftrightarrow CH_2(s) + H(s)$	3.7×10^{24} ; 9.513×10^{22}	0 ; 0	100 ; 52.58
16	$CH_2(s) + Ni(s) \Leftrightarrow CH(s) + H(s)$	3.7×10^{24} ; 3.008×10^{24}	0 ; 0	97.1 ; 76.43
17	$CH(s) + Ni(s) \Leftrightarrow C(s) + H(s)$	3.7×10^{21} ; 4.4×10^{22}	0 ; 0	18.8 ; 160.49
18	$CH_4(s) + O(s) \Leftrightarrow CH_3(s) + OH(s)$	1.7×10^{24} ; 8.178×10^{22}	0 ; 0	88.3 ; 28.72
19	$CH_3(s) + O(s) \Leftrightarrow CH_2(s) + OH(s)$	3.7×10^{24} ; 3.815×10^{21}	0 ; 0	130.1 ; 21.97
20	$CH_2(s) + O(s) \Leftrightarrow CH(s) + OH(s)$	3.7×10^{24} ; 1.206×10^{23}	0 ; 0	126.8 ; 45.42
21	$CH(s) + O(s) \Leftrightarrow C(s) + OH(s)$	3.7×10^{21} ; 1.764×10^{21}	0 ; 0	48.1 ; 129.08
	Charge transfer reactions(TPB)	Global B-V equation		
22	$H(s) + O^{2-}(YSZ) \Leftrightarrow OH^{-}(s) + e^{-}(Ni)$	$i_{an}^{H_2} = zFl_{TPB}i_{0,an}^{H_2}[\exp(\frac{\alpha zF}{RT}(\eta-\eta_{H_2})) - \exp(-\frac{(1-\alpha)zF}{RT}(\eta-\eta_{H_2}))]$		
23	$H(s) + OH^{-}(YSZ) \Leftrightarrow H_2O(s) + e^{-}(Ni)$	$i_{an}^{CO} = \frac{1}{3}zFl_{TPB}i_{0,an}^{CO}[\exp(\frac{\alpha zF}{RT}(\eta-\eta_{CO})) - \exp(-\frac{(1-\alpha)zF}{RT}(\eta-\eta_{CO}))]$		
24	$C(s) + O^{2-}(YSZ) \Leftrightarrow CO(s) + 2e^{-}(Ni)$			
25	$CO(s) + O^{2-}(YSZ) \Leftrightarrow CO_2(s) + 2e^{-}(Ni)$	$i_{an} = i_{an}^{H_2} + i_{an}^{CO}$		
Electrolyte (YSZ)				
26	$O_0^*(YSZ) + (YSZ) \Leftrightarrow O_0^*(YSZ) + V_0^*(YSZ)$			
Cathode surface(LSM)		A^0	α	E
27	$O_2(g) + 2(LSM) \Leftrightarrow 2O(LSM)$	10^{-2} ; 2.3×10^{15}	0	0 ; 258.2
28	$O(LSM) + V_0^*(YSZ) + 2e^{-} \Leftrightarrow O_0^*(YSZ) + (LSM)$	$i_{ca} = zFl_{TPB}i_{0,ca}[\exp(\frac{\alpha zF}{RT}(\eta-\eta_{eq})) - \exp(-\frac{(1-\alpha)zF}{RT}(\eta-\eta_{eq}))]$		

Rate constant of Arrhenius equation written as: $k = AT^n\exp(-E/RT)$, the unit of E is kJ/mol.

The carbon deposition issue is highlighted through the analysis of adsorbed surface carbons and the potential mitigation strategies are suggested.

7.2 HETEROGENEOUS SURFACE CHEMISTRY IN ELECTRODES

The heterogeneous chemical/electrochemical processes are influenced by not only the applied materials and catalysts but also the heterogeneous distribution of fuel species. The processes are much more complicated with hydrocarbon fuels than those with hydrogen fuel. For methane fueled Ni-YSZ/YSZ/YSZ-LSM button cell, the total of twenty-one reversible elementary reactions could occur with nickel as the anode catalysis [65] and is summarized in Table 7.1. The processes describe the basic mechanisms of methane reforming processes including dissociation, steam reforming, dry reforming and water-gas-shift process[128,129]. These elementary reactions consist of two types of processes: the adsorption/desorption processes and surface reaction processes. The surface of Ni provides the interaction site among adsorbed species without involving the electrochemical reactions and charge transfer processes[130]. At Ni-YSZ-gas triple phase boundary, charge transfer reactions take place between the adsorbed species and oxygen ions conducted from the electrolyte layer. The identification of kinetic steps of charge transfer is still difficult from experiments. It is envisioned that many charge transfer pathways may exist simultaneously[64,84,85], but only a few of them are rate-dominating steps. Therefore, in our following modeling, the H_2-H_2O and CO-CO_2 electro-oxidation pathways are assumed to be the two dominant electrochemical processes.

For the hydrogen oxidation process, the local equilibrium potential can be determined by,

$$\eta_{H_2} = \frac{\Delta G}{zF} + \frac{RT}{2F}\ln(\frac{p_{H_2} p_{O_2}^{0.5}}{p_{H_2O}}) \tag{7.1}$$

where, ΔG is the Gibbs free energy of the reaction, z is the number of electrons, p is the partial pressure, and the local Butler-Volmer equation can be formulated as,

$$i_{an}^{H_2} = z \cdot F \cdot l_{TPB} \cdot i_{0,an}^{H_2}[\exp(\frac{\alpha z F}{RT}(\eta - \eta_{H_2})) - \exp(-\frac{(1-\alpha) z F}{RT}(\eta - \eta_{H_2}))] \tag{7.2}$$

where, l_{TPB} is the three phase boundary length per unit volume, $i_{0,an}^{H_2}$ is the exchange current density and can be formulated as [74],

$$i_{0,an}^{H_2} = i_{H_2}^{*} \frac{(p_{H_2} / p_{H_2}^{*})^{0.25} (p_{H_2O})^{0.75}}{1 + (p_{H_2} / p_{H_2}^{*})^{0.5}} \tag{7.3}$$

where, $p_{H_2}^{*}$ is about 0.7atm; $i_{H_2}^{*}$ is the empirical constant used to fit the numerical results with experimental data.

The carbon monoxide oxidation process is quite similar to that of hydrogen[47]. It has been realized that the rate of CO oxidation is about 2~3 times less than that of hydrogen oxidation under the same oxidant partial pressure[109]. When the rate of CO oxidation reaction is assumed to be three times lower than that of H_2 oxidation, the modeling result is able to obtain a good agreement with experimental data[110]. Therefore, this assumption is employed to describe CO-CO_2 oxidation reaction,

$$\eta_{CO} = \frac{\Delta G}{zF} + \frac{RT}{2F}\ln(\frac{p_{CO} p_{O_2}^{0.5}}{p_{CO_2}}) \tag{7.4}$$

$$i_{an}^{CO} = \frac{1}{3} z \cdot F \cdot l_{TPB} \cdot i_{0,an}^{CO}[\exp(\frac{\alpha z F}{RT}(\eta - \eta_{CO})) - \exp(-\frac{(1-\alpha) z F}{RT}(\eta - \eta_{CO}))] \tag{7.5}$$

$$i_{0,an}^{CO} = i_{CO}^{*} \frac{(p_{CO} / p_{CO}^{*})^{0.25} (p_{CO_2})^{0.75}}{1 + (p_{CO} / p_{CO}^{*})^{0.5}} \tag{7.6}$$

where, i_{CO}^{*} is the empirical constant. Then, the total exchange current density within the anode can be formulated as,

$$i_{an} = i_{an}^{H_2} + i_{an}^{CO} \tag{7.7}$$

At the cathode side, two-step oxygen reduction reaction is assumed in order to keep the consistence of electrochemical reaction and charge transfer process:

$$O_2(g) + 2(LSM) \Leftrightarrow 2O(LSM)$$

$$O(LSM) + V^{\bullet\bullet}(YSZ) + 2e^{-} \Leftrightarrow O^{2-}(YSZ) + (LSM)$$

and the global Butler-Volmer equation can be built by,

$$i_{ca} = z \cdot F \cdot l_{TPB} \cdot i_{0,ca} [\exp(\frac{\alpha z F}{RT}(\eta - \eta_{eq})) - \exp(-\frac{(1-\alpha) z F}{RT}(\eta - \eta_{eq}))] \tag{7.8}$$

$$i_{0,ca} = i_{O_2}^{*} \frac{(p_{O_2} / p_{O_2}^{*})^{0.25}}{1 + (p_{O_2} / p_{O_2}^{*})^{0.5}} \tag{7.9}$$

where, $p_{O_2}^{*} = 4.9 \times 10^{8} \exp(-2 \times 10^{5} / RT)$; $i_{O_2}^{*}$ is the empirical fitting parameter; η_{eq} is the equilibrium overpotential (e.g., $\eta_{eq} = 0.75\eta_{H_2} + 0.25\eta_{CO}$).

7.3 TRANSPORT PROCESSES WITHIN THE CELL

In addition to the surface chemistry and electro-oxidation processes, SOFCs also include very complicated transport processes, such as fuel/gas transport in fuel supply tubes and porous electrodes, charge transport through material backbone, as well as heat transfer. The mass and charge transport processes are coupled together at reaction sites of porous electrodes through elementary reactions mentioned above. To elucidate these complicated transport and reaction mechanisms, the governing equations for

multi-transport processes are summarized in Table 7.2, the detailed modeling approach can be found in our previous study[131]. The applied operating parameters and corresponding boundary conditions are listed in Tables 7.3-7.5 respectively. In the model,

Table 7.2 Governing equations

Charge:	$-\nabla \bullet (\sigma_n^{eff} \nabla V_n) = \pm i_F \ , \quad n = e, i$
	$\sigma_e^{eff} = \phi(\frac{1-\varepsilon}{\tau})\sigma_e \ , \quad \sigma_i^{eff} = (1-\phi)(\frac{1-\varepsilon}{\tau})\sigma_i$
Mass:	$\nabla \bullet J_m + \rho v \bullet \nabla w_m = R_m \ ,$
	$J_m = -\rho w_m \sum_k D_{m,k}^{eff} [\nabla x_k + (x_k - w_k)\frac{\nabla p}{p}] \ ,$
	$D_{m,k}^{eff} = (\frac{\tau}{\varepsilon D_{m,k}} + \frac{1}{D_{Kn}})^{-1} \ ,$
	$D_{m,k} = 10^{-3} \frac{T^{1.75}(1/M_m + 1/M_k)^{0.5}}{p[(\sum_i V_{im})^{1/3} + (\sum_i V_{ik})^{1/3}]^2} \ ,$
	$D_{Kn} = \frac{d_{pr}}{3}\sqrt{\frac{8\kappa NT}{\pi M}}$
Momentum:	$\nabla p + \rho(v \bullet \nabla)v = \nabla \bullet [\mu(\nabla v + (\nabla v)^T) - \frac{2}{3}\mu(\nabla \bullet v)\mathrm{I}]$
	$\nabla \bullet (pv) = 0 \ ,$
	$\frac{\mu}{K} v = -\nabla p + \frac{1}{\varepsilon}\nabla \bullet \left\{ \mu[\nabla v + (\nabla v)^T] - \frac{2}{3}\mu(\nabla \bullet v) I \right\} \ ,$
	$K = \frac{\varepsilon^3 {d_p}^2}{150(1-\varepsilon)^2}$
Heat:	$c_p v \bullet \nabla T - \nabla \bullet (k_e \nabla T) = Q_h \ ,$
	$k_e = \beta k_l + (1-\beta)k_s \ ,$
	$Q_{h,r} = r \cdot \Delta H \ , \quad Q_{h,ac} = -(\eta_{act} + \eta_{con}) \cdot i \cdot AV_e \ , \quad Q_{h,ohm} = i^2 / \sigma$

several assumptions are employed: (1) the catalyst Ni is uniformly distributed within the anode electrode; (2) the microstructure of electrodes is homogeneous and stable; and (3)

the effects of carbon deposition on the pore structure and catalytic activity of Ni are neglected.

Table 3 Reaction Source terms

Net reaction rate of adsorbates	Reaction source term	Energy source term
$r_{CH4(s)} = r_3 - r_{14} - r_{18}$	$R_{H2} = -2r_1$	$R_{Ca} = Q_{ohm} + Q_{chem}$
$r_{CH3(s)} = r_{14} - r_{15} + r_{18} - r_{19}$	$R_{CH4} = -r_2$	$R_{El} = Q_{ohm}$
$r_{CH2(s)} = r_{15} - r_{16} + r_{19} - r_{20}$	$R_{H2O} = -r_4$	$R_{An} = Q_{ohm} + Q_{chem}$
$r_{CH(s)} = r_{16} - r_{17} + r_{20} - r_{21}$	$R_{CO2} = -r_5$	$R_{Cl} = 0$
$r_{C(s)} = -r_{10} + r_{17} + r_{21} - r_{24}$	$R_{CO} = -r_6$	
$r_{CO(s)} = r_6 + r_{10} - r_{11} + r_{12} + r_{24} - r_{25}$	$R_{O2} = -r_{27}$	
$r_{CO2(s)} = r_5 + r_{11} + r_{25}$		
$r_{H(s)} = 2r_1 - r_7 - r_8 + r_{12} + r_{14} + r_{15} + r_{16} + r_{17} - r_{22} - r_{23}$		
$r_{OH(s)} = r_7 - r_8 - r_9 + r_{13} + r_{18} + r_{19} + r_{20} + r_{21} + r_{22} - r_{23}$		
$r_{O(LSM)} = 2r_{27} - r_{18}$		

Table 4 Operation parameters

	Value	Units
Cathode layer thickness, radius	4×10^{-5}, 2.5×10^{-3}	m
Electrolyte layer thickness, radius	2×10^{-5}, 6.5×10^{-3}	m
Anode layer thickness, radius	3.5×10^{-4}, 6.5×10^{-3}	m
Inlet fuel channel radius, wall radius	1×10^{-3}, 1.5×10^{-3}	m
Outlet fuel channel radius	6.5×10^{-3}	m
Gas constant	8.314	$J\cdot mol^{-1}K^{-1}$
Pressure	1	atm
Anode ionic conductivity	$3.34\times10^{4}\exp(-10300/T)$	$S\cdot m^{-1}$
Cathode ionic conductivity	$3.34\times10^{4}\exp(-10300/T)$	$S\cdot m^{-1}$
Anode electronic conductivity	2×10^{6}	$S\cdot m^{-1}$
Cathode electronic conductivity	$42\times10^{6}\exp(-1150/T)/T$	$S\cdot m^{-1}$
Electrolyte ionic conductivity	$3.34\times10^{4}\exp(-10300/T)$	$S\cdot m^{-1}$
Porosity(ε)	0.4	1
Particle diameter	2×10^{-6}	m
Tortuosity	$((3-\varepsilon)/2)^{0.5}$	1
Permeability	$\varepsilon^3 d^2/(1-\varepsilon)^2/150$	1
Inlet velocity	0.2	$m\cdot s^{-1}$
Surface site density of Ni	6.1×10^{-9}	$mol\cdot cm^{-2}$
Specific three-phase boundary length	1.8×10^{12}	$m\cdot m^{-3}$

7.4 SOLUTION ALGORITHM AND MODEL VALIDATION

The mathematical model is solved using COMSOL MULTIPHSICS V4.0. For a specified cell voltage at the cathode electrode boundary, the corresponding average cell current density and the species distributions are calculated. The cell polarization curve is then obtained by specifying a series of cell voltages and calculating the corresponding average cell current density. The species distributions associated with multi-physics transport and surface reaction processes are calculated at each of the individual voltage conditions.

Table 5 Boundary conditions

Interfaces(Ω)	$\Omega_{Ca/Cl}$	$\Omega_{Ca/El}$	$\Omega_{El/An}$	$\Omega_{An/Cl}$	Ω_{Cl}
Ionic charge	Insulation	Continuity	Continuity	Insulation	N/A
Electronic charge	Specified voltage	Insulation	Insulation	0	N/A
Mass	O_2/N_2 (Mass fractions)	Insulation	Insulation	Continuity	CH_4/H_2O (Mass fraction)
Momentum	Pressure	Wall (no slip)	Wall (no slip)	Continuity	Flow rate, pressure
Energy	Temperature	Continuity	Continuity	Continuity	Temperature

The model is validated using experimental polarization curves, where the mixture of 97% CH_4+3% H_2O is used as the fuel and ambient oxygen as the oxidant. Figure 7.1 has illustrated the corresponding experimental setup. The cell polarization curve is obtained at three temperatures of 600^oC, 650^oC and 700^oC respectively. As shown in Figure 7.2, the model predictions match with experimental data reasonably well.

This model is then used for further numerical studies.

7.5 RESULTS AND DISCUSSION

7.5.1 Distribution of gas species and adsorbates

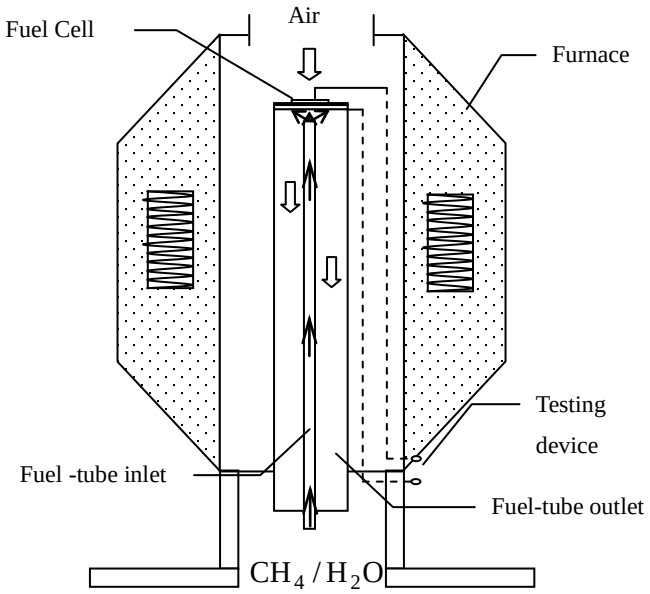

Figure 7.1 Schematic of button cell test system

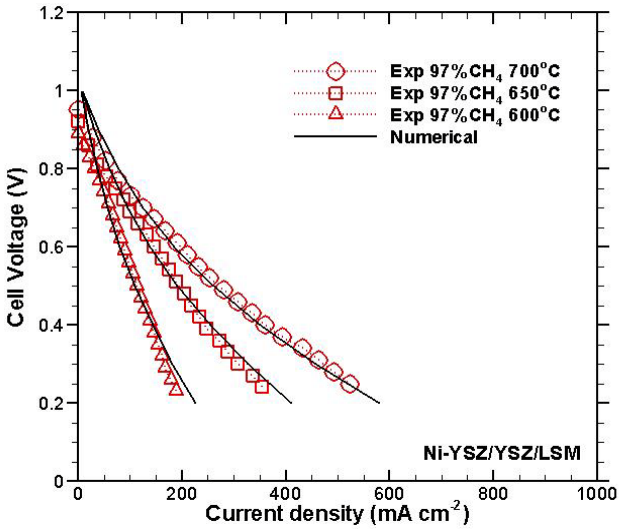

Figure 7.2 Comparison between model predictions and experimental data

Figure 7.3 shows the distributions of gas species within the fuel supply tubes

and the porous anode. Here the operating temperature for the simulation is 700^{o}C and the cell voltage is set at 0.5V as an example. Within the small fuel supply tube, the distributions of gas species are relatively uniform. Beyond the outlet the small tube, the molar fractions of CH_4 and CO decrease toward the anode electrode and increase from the anode electrode toward the outlet of the large ceramic tube. The molar fractions show relatively large gradients near the porous anode. The molar fractions of H_2O and CO_2 show opposite trends. Essentially, the surface reactions in the anode consume adsorbed hydrocarbon fuel CH_4, and generate H_2O and CO_2 through the electrochemical reaction processes. The CO species is generated through surface reaction process and consumed by oxidation process. The combinational effects lead to the species distributions mentioned above.

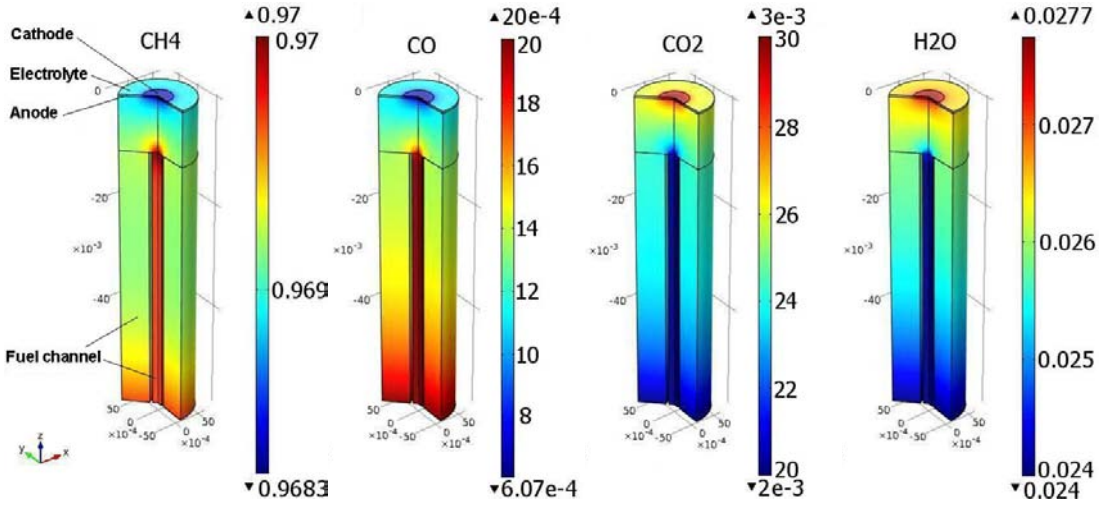

Figure 7.3 Distributions of fuel/gas species within fuel supply tubes and anode electrode

Figure 7.4 illustrates the major adsorbed species on the anode porous electrode surface, which are important reaction intermediates affecting the CH_4 conversion and oxidation processes. The surface coverage of all surface adsorbed intermediates, e.g.,

CH_4(s), CH_3(s), CH_2(s), CH(s), C(s) and H(s) decrease from the channel/anode interface and anode circumference toward the anode/electrolyte interface, while the surface oxidation products of H_2O(s) and CO_2(s) shows opposite trend, decreasing from the anode/electrolyte interface toward the channel/anode interface and anode circumference.

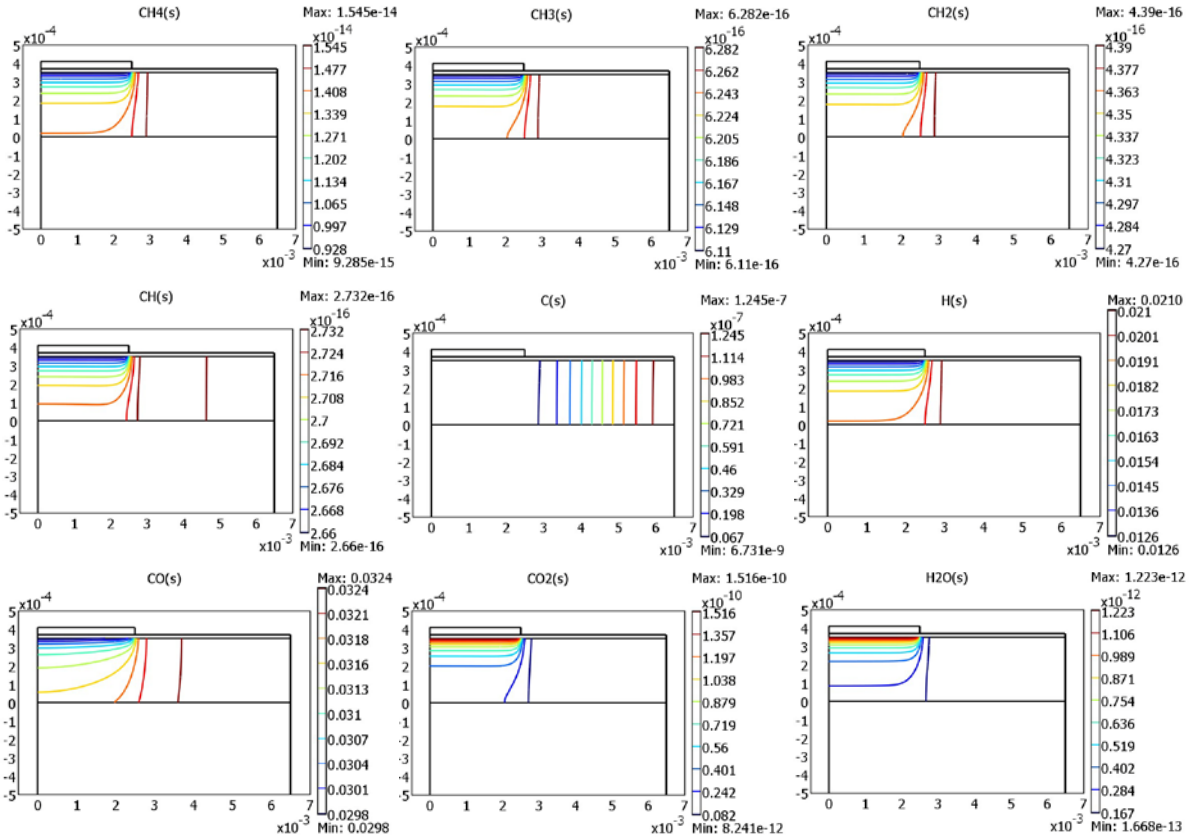

Figure 7.4 Distributions of surface coverage of adsorbed species within anode electrode

These observations indicate that the surface reactions of methane and electro-oxidation processes are relatively intensive near the anode/electrolyte interface. As mentioned above, for Ni-based anode, the hydrocarbon fuel could lead to the deposition of carbon on the surface of catalyst Ni, resulting in the deactivation of Ni catalytic function. As shown in Figure 7.4, the surface coverage of adsorbed carbon is relatively high at the

circumference of the anode and decreases toward the electrolyte/anode interface. Since the electrochemical reactions are relatively intensive near the electrolyte/anode interface and relatively weak at the circumference of the anode, it seems that the strong electrochemical reactions may facilitate to mitigate carbon adsorptions.

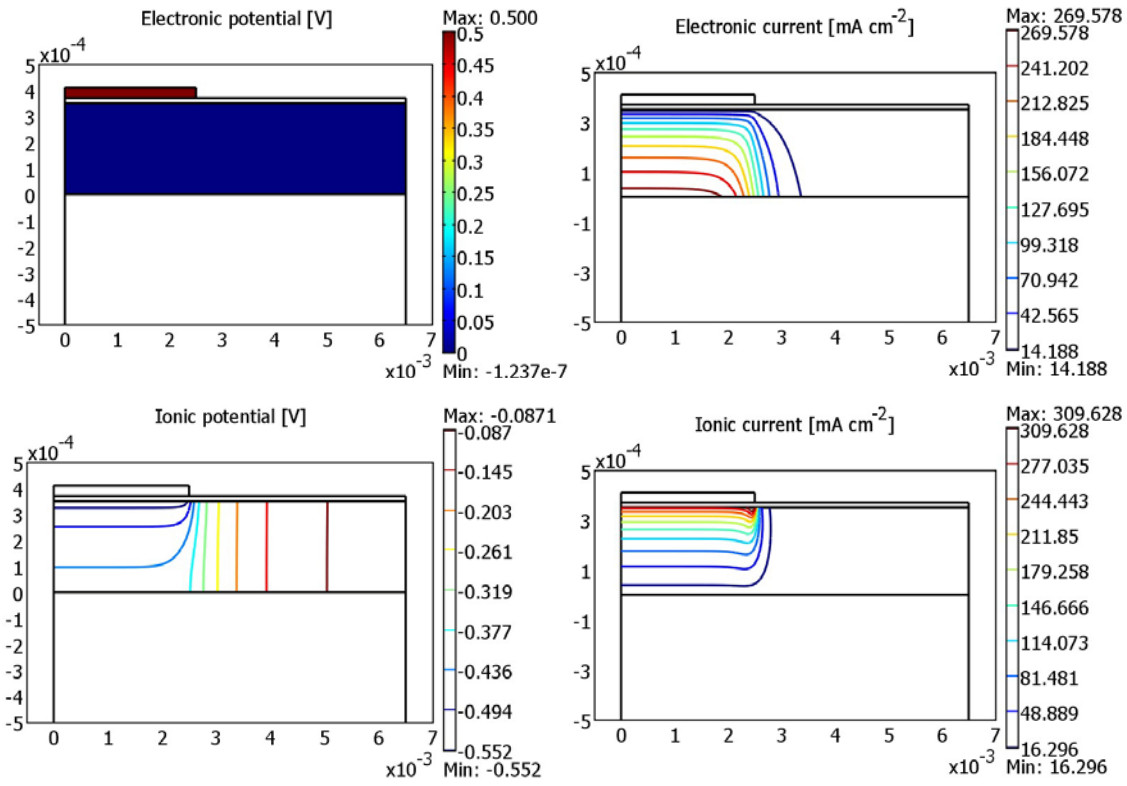

Figure 7.5 Distributions of electronic/ionic potential and current density within the anode

7.5.2 Local ionic/electronic potential and current

The distributions of local ionic/electronic potential and current densities are shown in Figure 7.5. It can be seen that the electronic potential in the cathode maintains at the specified level of 0.5V while that in the anode is approximately equal to zero. The electronic current density decreases from the channel/anode interface towards the

anode/electrolyte interface. The ionic potential decreases from the channel/anode interface towards the anode/electrolyte interface as well as from the anode circumference to the axial-symmetric line of the anode. The corresponding ionic current density distribution shows opposite trend. Since the YSZ electrolyte layer only allows oxygen ions to migrate through, the highest ionic current density around the anode/electrolyte layer indicates that the electrochemical reactions are much intensive at this site.

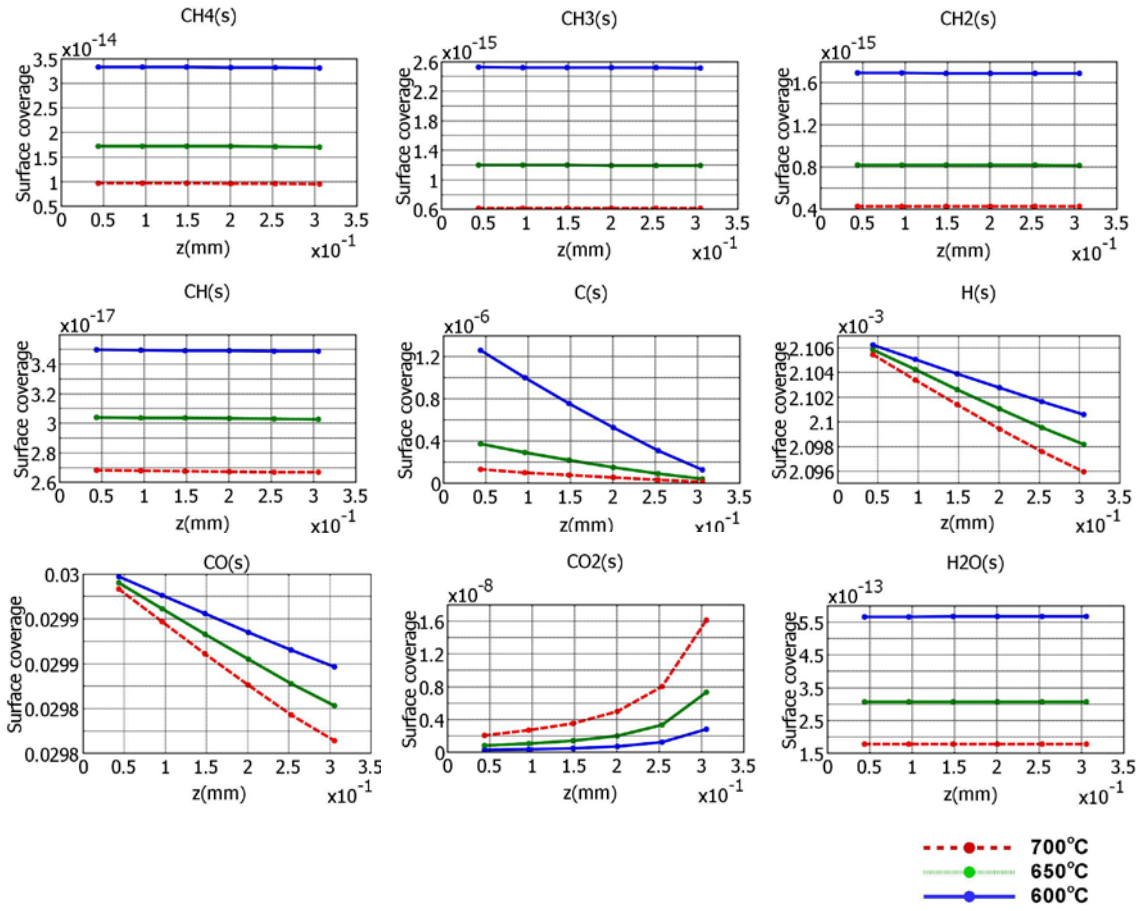

Figure 7.6 Distributions of adsorbed species along the axis-symmetrical line of the cell under different operating temperatures

7.5.3 Effect of operating temperature and current

The operating temperature/current can significantly affect multi-physics transport processes. This issue has been studied extensively in open literature. Usually the distributions of gas species are calculated under different temperature/current conditions and the corresponding SOFC performance is interpreted based on the bulk species distributions. However, it is rare in open literature to extensively study the distributions of adsorbed surface species under such operating conditions because of lacking of coherent links between bulk transport processes and surface reaction processes in SOFC button cell modeling. With the model developed in this paper, we are able to determine various surface species distributions under practical button cell operating conditions. Since the bulk species distributions have been investigated extensively in open literature, here we focus on adsorbed surface species in this paper, the bulk species distributions will not be shown for the concise and compact descriptions.

To examine the temperature effects on the surface chemistry, the distributions of surface adsorbed species along the axis-symmetrical line of the button cell are obtained under three temperatures of 600^{o}C, 650^{o}C and 700^{o}C respectively. Here the cell voltage is set at 0.5V as an example. As shown in Figure 7.6, the surface coverage of adsorbed CH_4(s), CH_3(s), CH_2(s), CH(s), and H_2O(s) are pretty uniform and those of adsorbed CO(s), H(s), and C(s) decrease from the anode/electrolyte interface towards the channel/anode interface along this axis-symmetrical line. The surface coverage of all these adsorbates decreases with increasing the operating temperature. It is worth noting

that the surface coverage of carbon significantly decreases particularly near the anode/electrolyte interface when the temperature increases from 600°C to 700°C, indicating that high operating temperature may potentially mitigate the surface carbon deposition. The surface coverage of adsorbed CO_2(s) increases nonlinearly from the anode/electrolyte interface towards the channel/anode interface along the axis-symmetrical line and increase with raising the operating temperatures.

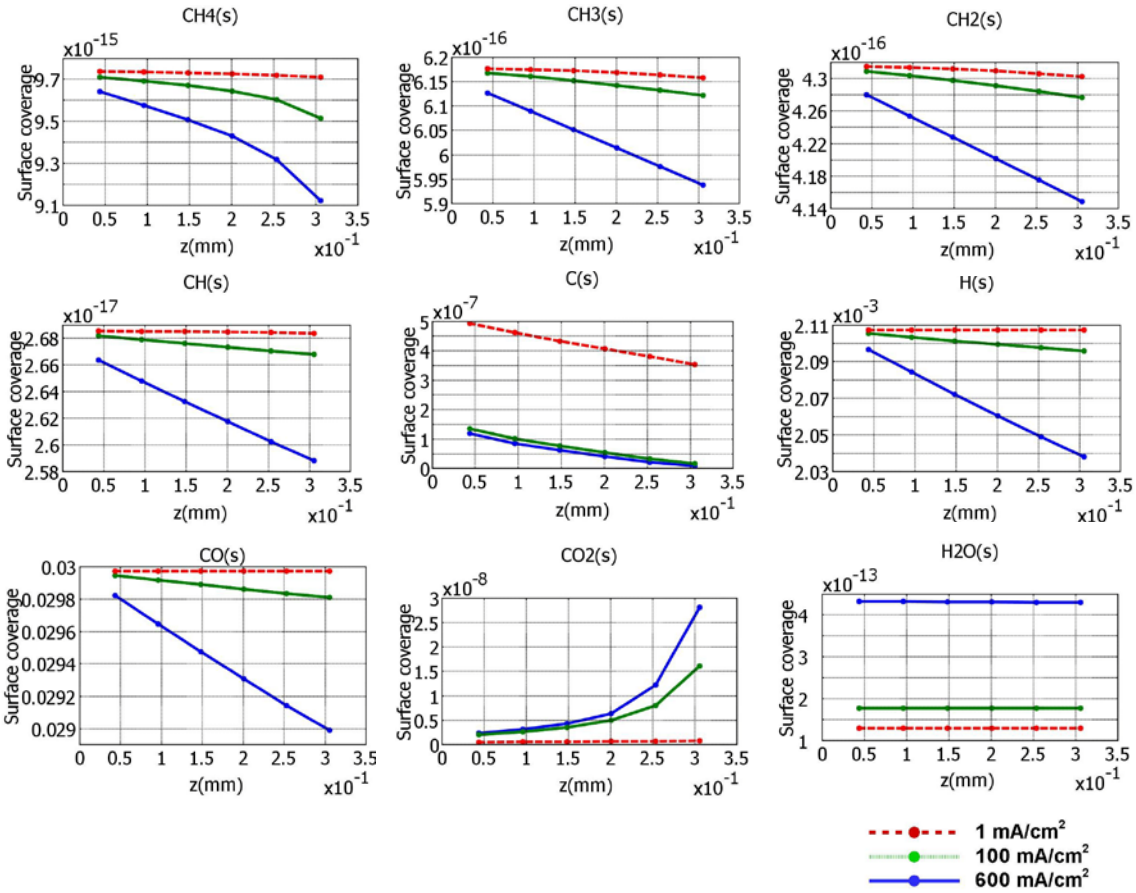

Figure 7.7 Distributions of adsorbed species along the axis-symmetrical line of the cell under different cell current loads

The effects of the cell current on the surface adsorbed species are shown in

Figure 7.7. The surface coverage of methane dissociation intermediates, e.g., $CH_4(s)$, $CH_3(s)$, $CH_2(s)$, CH(s), and H(s) and CO(s) decreases with increasing the cell current density, while that of $H_2O(s)$ and $CO_2(s)$ increases. Since the intermediate species $CH_4(s)$, $CH_3(s)$, $CH_2(s)$, CH(s), and H(s) and CO(s) are consumed and those of $H_2O(s)$ and $CO_2(s)$ are generated, increasing the current density improves the forward electrochemical reactions, consuming more fuels while generating more products. It is interesting to note that the adsorbed carbon C(s) decreases with increasing the current density, implying that high current density inhibits carbon deposition on the surface of catalyst Ni. Increasing the current improves the O^{2-} ions conducting from the cathode to anode side and the generation of more O(s) ions on the anode surface, as a result, enhancing oxidation reaction of adsorbed carbon C(s).

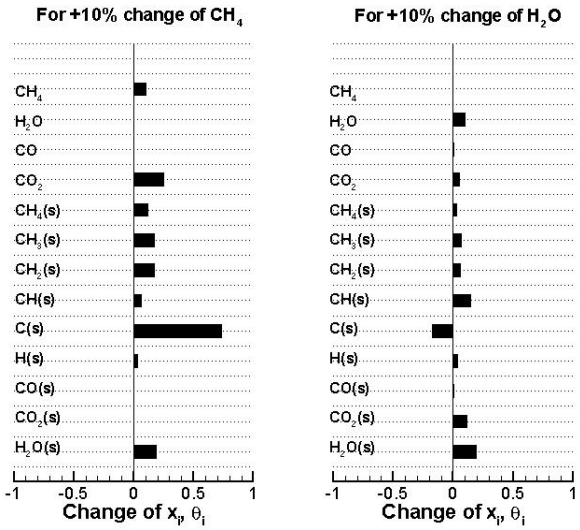

Figure 7.8 Sensitivity of 10% increase of the supplied CH_4 and H_2O on the molar fraction of species and the surface coverage of adsorbed species. The results are obtained at the intersect point between the anode/electrolyte interface and the axial-symmetric line of the cell.

7.5.4 Sensitivity analysis of bulk gas species

The surface elementary reaction processes are very complicated when hydrocarbon, e.g., methane, is used as the fuel. To study the different roles and relative importance of different processes and associated surface intermediates, the sensitivity analysis is carried out. Here the operating temperature is 700^{o}C and the cell voltage is set at 0.5V.

In the first case study, the sensitivities of the bulk gas species and adsorbates with respect to the variation of the supplied CH_4 are studied. The simulations are run by adding 10% more methane to the anode inlet. Figure 7.8 shows the corresponding variations of various species at the intersect point between the anode/electrolyte interface and the cell axial-symmetric line. It is clearly seen that the surface adsorbed species carbon C(s) is very sensitive to the change of the supplied methane. Here C(s) increases significantly with increasing the methane fraction in the fuel. The bulk gas species CO_2 and the surface adsorbed species H_2O(s), CH_4(s), CH_3(s), CH_2(s), CH(s), and H(s) show different degree of sensitivities to the variation of the supplied methane. The rest of species are not sensitive to the supplied methane. Similarly by adding 10% more H_2O to the anode inlet and running the simulation, the sensitivities of the bulk gas species and surface adsorbates relative to the variation of the supplied H_2O can be obtained. As shown in Figure 7.8, increasing the H_2O content in the anode actually improves the contents of CH_4(s), CH_3(s), CH_2(s), CH(s) and H(s) as well as the bulk gas species of CO and CO_2. Among these species, the surface adsorbates CH(s), CO_2(s) and H_2O(s) show

relatively high sensitivities to the variation of H_2O content. It is interesting to see that the adsorbed species carbon C(s) is very sensitive to the variation of H_2O content in the anode, increasing the H_2O content may significantly reduce the adsorbed surface carbon C(s). The high sensitivity of surface adsorbate C(s) to CH_4 and H_2O suggests that suitable combination of CH_4 and H_2O contents in the anode may mitigate the carbon deposition on the surface of Ni catalyst.

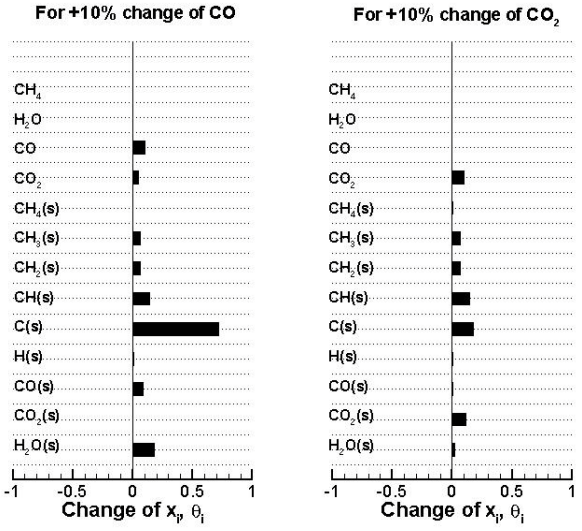

Figure 7.9 Sensitivity of 10% increase of the supplied CO and CO_2 on the molar fraction of species and the surface coverage of adsorbed species. The results are obtained at the intersect point between the anode/electrolyte interface and the axial-symmetric line of the cell.

The sensitivities of the bulk gas species and surface adsorbates to the variations of the CO and CO_2 contents in the anode are also studied. The results are illustrated in Figure 7.9. When 10% more CO is added to the supplied fuel gas, the surface adsorbed carbon C(s) increases significantly, indicating that increasing CO content may potentially intensify the carbon deposition effect. The concentrations of species CO_2, CH_3(s), CH_2(s), CH(s), CO(s) and H_2O(s) show different degree of sensitivities and increase with

increasing the CO content in the anode. When the CO_2 content increases, the bulk gas species are not affected; the surface adsorbed species show different sensitivities, including CH_4(s), CH_3(s), CH_2(s), CH(s), H(s), C(s), CO(s), CO_2(s) and H_2O(s), among which C(s), CH(s), and CO_2(s) show relatively high sensitivities to CO_2 variation.

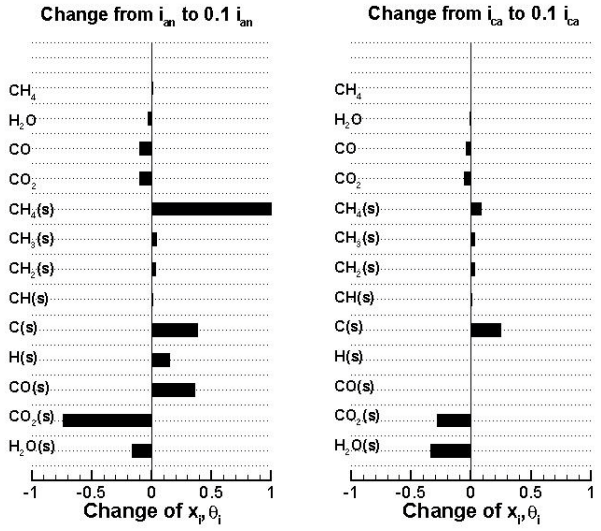

Figure 7.10 Effects of the exchange current density of both anode and cathode electrodes on the species molar fraction and the adsorbates surface coverage. The results are obtained at the intersect point between the anode/electrolyte interface and the axial-symmetric line of the cell.

7.5.5 Effect of surface exchange current density

Theoretically, the surface exchange current is the ongoing current of a redox reaction in both cathodic and anodic directions, which reflects the intrinsic rates of electrochemical processes. The surface exchange current density depends critically on the nature of the electrodes, such as physical structure and electrochemical properties. Since the surface exchange current density has great influence on the cell performance, the sensitivities of bulk gas species and surface adsorbates to the anode and cathode

exchange current densities are studied in this section. In particular the exchange current densities are reduced from the base value to the 10% of its base value for the anode (i_{an}) and cathode (i_{ca}) respectively. The corresponding concentration variations of bulk gas species and surface adsorbates are calculated. Here the operating temperature is 700^{o}C and the cell voltage is set at 0.5V. As shown in Figure 7.10, when the anodic exchange current density reduces to its 10% base value ($0.1i_{an}$), the bulk gas species H_2O, CO and CO_2 decrease, the surface adsorbates H_2O(s) and particularly CO_2(s) also show significant decrease. Other surface adsorbates, e.g., CH_4(s), CH_3(s), CH_2(s), CH(s), C(s), H(s), and CO(s) show different degree of increase with species CH_4(s), C(s), H(s), and CO(s) having relatively high sensitivities. When the cathodic exchange current density reduces to its 10% base value ($0.1i_{ca}$), the surface adsorbates CO_2(s) and H_2O(s) decrease significantly while the surface adsorbed carbon C(s) increases. The oxygen ions transport from the cathode side to the anode side, where ions react with the adsorbed species H(s), C(s) and CO(s), generating CO_2(s) and H_2O(s). Because the cathodic exchange current density decreases, the number of oxygen ions transported to the anode side also decreases, leading to the above observed surface species variations. Other species including the bulk gas species CO, CO_2 and the surface adsorbates CH_4(s), CH_3(s), CH_2(s) show relatively low sensitivities to the variation of cathodic exchange current density. The results also show that surface adsorbed carbon C(s) is very sensitive to the variations of both anode and cathode exchange current density. Thus it facilitates to mitigate the surface carbon deposition by developing high performance electrode materials.

7.6 CONCLUSION

A comprehensive direct methane-fueled SOFC model is developed based on a physical button cell test system. Both H_2-H_2O and CO-CO_2 electro-oxidation processes are considered and coherently integrated into the multi-transport processes of charge, mass, momentum, and energy with the detailed surface reaction processes. The model is validated using the experimental data under the temperatures of 600^{o}C, 650^{o}C and 700^{o}C respectively. Based upon the model validation, extensive simulations are performed to identify complicated transport interactions with the emphasis on surface reaction processes and surface adsorbates. Results show that the surface reactions of methane and electrochemical reactions are relatively intensive near the anode/electrolyte interface. The bulk gas species and surface adsorbates show different degree of sensitivities to operating conditions and electrode properties. The surface adsorbed carbon species is very sensitive to the exchange current density of anode and cathode electrodes and the fuel compositions including CH_4, H_2O, CO, CO_2. To mitigate potential surface carbon deposition, one may: (1) suitably increase H_2O content in the fuel; (2) reduce the content of CH_4, CO, CO_2 in the supplied fuel; (3) increase the operating temperature; (4) increase the cell operating current; (5) improve exchange current density of anode and/or cathode electrode by using high performance electrode materials.

CHAPTER 8

MULTIPHYSICAL MODELING OF SOLID OXIDE ELECTROLYSIS CELLS FOR SYNGAS GENERATION WITH DEATILED SURFACE CHEMISTRY

8.1 INTRODUCTION

The potential fossil fuel crisis and climate changes raise the need to develop renewable and clean energy technology[132]. The co-electrolysis of H_2O and CO_2 using the inverse process of solid oxide fuel cell (SOFC) is able to produce synthetic gas in a clean and efficient way[133,134]. Such a technique has been demonstrated experimentally and attracted much interest recently[135]. Since experimental technique is limited in probing complicated transport and surface chemistry particularly in porous electrodes, modeling method as a complementary technique has been resorted extensively.

There have been recent studies on numerical modeling of solid oxide electrolysis cell (SOEC), including H_2O electrolysis[136-139] and CO_2 electrolysis[80,140,141]. Usually such models are a global type of kinetic models, where the concentrations of bulk gas species are used for Butler-Volmer equation to couple electrochemical reactions with transport process in porous electrodes. As a consequence, the adsorbed species on electrode surface and surface reactions are neglected. To overcome this issue, the elementary kinetic modeling approach is recently investigated[64,74,84,85,128,142] to describe

the adsorption/desorption processes and the detailed surface chemistry via individual reaction steps. While elementary kinetic model is able to provide more precise electrochemical charge-transfer calculation, such model is limited to describe the reaction process at one individual point on the electrode surface. Currently there is a lack of coherent integration between macro-scale transport processes and local elementary kinetic reactions. On the other hand, the elementary kinetic models are mainly studied for SOFCs[64,74,84,85,128], there is little efforts for SOEC modeling[142].

In this study, a SOEC model for the simulation of synthetic gas generation is developed, bridging macro-scale transport processes with elementary kinetic reactions in a coherent way. A button cell test system is used as a physical base for modeling demonstration.

8.2 HETEROGENEOUS SURFACE CHEMISTRY IN ELECTRODES

In principle, the heterogeneous chemical/electrochemical processes take place on the SOEC electrode surface, which are affected by not only the applied catalysts and materials but also the porous structure of electrodes. For H_2-electrode supported Ni-YSZ/YSZ/LSM button cell, the surface chemical processes are usually more complicated on H_2 electrode side than those on O_2 electrode side due to both the active catalytic function of Ni and the complicated fuel/gas compositions. Table 8.1 provides twenty one reversible elementary reactions of syngas fuel on Ni surface proved by experiments, where two types of processes can be identified: the adsorption/desorption

process and surface reaction process. Basically, the adsorption/desorption process is the first step for syngas species to be adsorbed on the electrode surface, then the surface reactions take place among all adsorbates and reaction intermediates. According to molecular behavior, none of electrochemical reaction and charge transfer process takes place on the catalytic Ni surface, but on Ni-YSZ surface (triple phase boundary), several charge transfer pathways could exist simultaneously[84]. Since the kinetics of charge transfer (CT) steps are not directly available from experiments, Bessler et al.[64,84,85] have proposed several possible types of CT reactions and taken them as free fit parameters to compare model predictions with experimental results. It was found that all proposed CT mechanisms can fit the experiment results well except the double oxygen-spillover CT mechanisms which would fail to give correct predictions when the electrode was polarized under high steam partial pressures. Thus, in our modeling, a single-step reversible CT mechanism is assumed at the triple phase boundary, i.e., the adsorbed oxygen ions gain/release all electrons on the Ni-YSZ surface by one step reaction, and is expressed as,

CT reaction: $O(s) + (YSZ) + 2e^{-}(Ni) \Leftrightarrow O^{2-}(YSZ) + Ni(s)$

Conduction of oxygen ion: $O^{2-}(YSZ) + V^{\bullet\bullet}(YSZ) \Leftrightarrow O^{\times}(YSZ) + (YSZ)$

here, $O^{\times}(YSZ)$ is the lattice oxygen, $V^{\bullet\bullet}(YSZ)$ is the oxygen vacancy, $O(s)$ is the adsorbed oxygen ion on Ni surface. The elementary kinetic reaction rate can be formulated by,

$$i_{F,an} = nFl_{tpb}(k_f \theta_{O^{2-}(YSZ)} \theta_{Ni} - k_b \theta_{O(s)}) \tag{8.1}$$

where, $i_{F,an}$ is the source of the faradic current derived from electrochemical reactions in the H_2 electrode; n is the number of transferred electrons; l_{tpb} is the volume-specific triple phase boundary length; θ_i is the surface coverage of species i; k_f and k_b are the forward and backward reaction rates respectively, and can be described by Arrhenius expression[119],

$$k_f = AT^n \exp(\frac{-E_f^{act}}{RT}) \exp(\alpha \frac{nF}{RT}\eta), \qquad k_b = AT^n \exp(\frac{-E_b^{act}}{RT}) \exp(-(1-\alpha)\frac{nF}{RT}\eta) \tag{8.2}$$

where, A_i , n_i and $E^{act}{}_i$ are the Arrhenius parameters for reaction i and listed in Table 8.1; R is the gas constant; T is the reaction temperature; η is the potential difference formed by electrical double layer at H_2 electrode/electrolyte interface, i.e., $\eta = \phi_{anode} - \phi_{electrolyte}$.

In order to keep the consistence of electrochemical reaction and charge transfer process, oxygen production within O_2 electrode is formulated by two step elementary reactions, the first step is the charge transfer process:

$$O^{\times}(YSZ) + (LSM) \Leftrightarrow O(LSM) + V^{\bullet\bullet}(YSZ) + 2e^{-}$$

Subsequently, the adsorption/desorption process of oxygen on the O_2 electrode (LSM) surface takes place:

$$2O(LSM) \Leftrightarrow O_2(gas) + (LSM)$$

For the simplicity, a global Butler-Volmer equation is utilized to describe the reaction rate in the O_2 electrode[74],

$$i_{F,ca} = i_{ca}^{*} \frac{(p_{O_2} / p_{O_2}^{*})^{0.25}}{1+(p_{O_2} / p_{O_2}^{*})^{0.5}} (\exp(\frac{0.5F\eta_{act}}{RT}) - \exp(-\frac{0.5F\eta_{act}}{RT})) \tag{8.3}$$

where, $i_{F,ca}$ is the Faradic current of cathode; i_{ca}^{*} is the empirical parameter utilized to fit the simulation with experimental data; $p_{O_2}^{*} = 4.9\times10^{8}\exp(-200000/RT)$; p_{O_2} is the local oxygen partial pressure; η_{act} is the activation overpotential between O_2 electrode potential $\phi_{cathode}$ and equilibrium potential ϕ_{eq} [119]:

$$\phi_{eq} = -\frac{\Delta G}{nF} - \frac{RT}{nF}\ln\frac{a(O^{\times})}{a(O_2)^{0.5}a(V^{\bullet\bullet})} \tag{8.4}$$

where, ΔG is Gibbs free energy of the elementary reaction in the O_2 electrode; a is the dimensionless activity.

8.3 SURFACE DIFFUSION

According to the mean field approach, the concentration of surface species i can be normalized by the total available surface sites Γ, yielding a dimensionless item of surface coverage θ, ($\theta = c_i\sigma_i^{surf}/\Gamma$), then the surface mass action can be built by [85],

$$\frac{\sigma_i^{surf}}{\Gamma} R_n = -\nabla\bullet(D_i^{suf}\nabla\theta_i) \tag{8.5}$$

where, σ_i^{surf} is the number of surface sites occupied by species i; D_i^{suf} is the surface diffusivity of species i ($D_i^{suf} = D_i^0\exp(-E_i^{act}/RT)$); R_n is the net reaction rate for species n and is determined as,

$$R_n = \sum_n \nu_n (k_f \prod_i [c_i^{Ra}]^{n_i} - k_b \prod_j [c_j^{Pu}]^{m_j}) \tag{8.6}$$

where, ν_n is the pre-factor for elementary reaction; c_i^{Ra} and c_j^{Pu} are the concentrations of reactant and product respectively while n_i and m_j are the corresponding stoichiometric

factors.

Table 8.1 Surface reaction mechanism

Ni – surface		A	n	E
Adsorption/Desorption($f;b$)				
1	$H_2 + Ni(s) + Ni(s) \Leftrightarrow H(s) + H(s)$	10^{-2} ; 5.593×10^{19}	0 ; 0	0 ; 88.12
2	$O_2 + Ni(s) + Ni(s) \Leftrightarrow O(s) + O(s)$	10^{-2} ; 2.508×10^{23}	0 ; 0	0 ; 470.39
3	$CH_4 + Ni(s) \Leftrightarrow CH_4(s)$	8×10^{-3} ; 5.302×10^{15}	0 ; 0	0 ; 33.15
4	$H_2O + Ni(s) \Leftrightarrow H_2O(s)$	1×10^{-1} ; 4.579×10^{12}	0 ; 0	0 ; 62.68
5	$CO_2 + Ni(s) \Leftrightarrow CO_2(s)$	1×10^{-5} ; 9.334×10^{7}	0 ; 0	0 ; 28.80
6	$CO + Ni(s) \Leftrightarrow CO(s)$	5×10^{-1} ; 4.041×10^{11}	0 ; 0	0 ; 112.85
Surface Reactions				
7	$O(s) + H(s) \Leftrightarrow OH(s) + Ni(s)$	5×10^{22} ; 2.005×10^{21}	0 ; 0	97.9 ; 37.19
8	$OH(s) + H(s) \Leftrightarrow H_2O(s) + Ni(s)$	3×10^{20} ; 2.175×10^{21}	0 ; 0	42.7 ; 91.36
9	$OH(s) + OH(s) \Leftrightarrow O(s) + H_2O(s)$	3×10^{21} ; 5.423×10^{23}	0 ; 0	100 ; 209.37
10	$O(s) + C(s) \Leftrightarrow CO(s) + Ni(s)$	5.2×10^{23} ; 1.418×10^{22}	0 ; −3	148.1 ; 115.97
11	$O(s) + CO(s) \Leftrightarrow CO_2(s) + Ni(s)$	2×10^{19} ; 3.214×10^{23}	0 ; −1	123.6 ; 86.5
12	$HCO(s) + Ni(s) \Leftrightarrow CO(s) + H(s)$	3.7×10^{21} ; 2.338×10^{20}	0 ; −1	0 ; 127.98
13	$HCO(s) + Ni(s) \Leftrightarrow O(s) + CH(s)$	3.7×10^{24} ; 7.914×10^{20}	-3 ; 0	95.8 ; 114.22
14	$CH_4(s) + Ni(s) \Leftrightarrow CH_3(s) + H(s)$	3.7×10^{21} ; 4.438×10^{21}	0 ; 0	57.7 ; 58.83
15	$CH_3(s) + Ni(s) \Leftrightarrow CH_2(s) + H(s)$	3.7×10^{24} ; 9.513×10^{22}	0 ; 0	100 ; 52.58
16	$CH_2(s) + Ni(s) \Leftrightarrow CH(s) + H(s)$	3.7×10^{24} ; 3.008×10^{24}	0 ; 0	97.1 ; 76.43
17	$CH(s) + Ni(s) \Leftrightarrow C(s) + H(s)$	3.7×10^{21} ; 4.4×10^{22}	0 ; 0	18.8 ; 160.49
18	$CH_4(s) + O(s) \Leftrightarrow CH_3(s) + OH(s)$	1.7×10^{24} ; 8.178×10^{22}	0 ; 0	88.3 ; 28.72
19	$CH_3(s) + O(s) \Leftrightarrow CH_2(s) + OH(s)$	3.7×10^{24} ; 3.815×10^{21}	0 ; 0	130.1 ; 21.97
20	$CH_2(s) + O(s) \Leftrightarrow CH(s) + OH(s)$	3.7×10^{24} ; 1.206×10^{23}	0 ; 0	126.8 ; 45.42
21	$CH(s) + O(s) \Leftrightarrow C(s) + OH(s)$	3.7×10^{21} ; 1.764×10^{21}	0 ; 0	48.1 ; 129.08
Ni/YSZ- Surface (Charge transfer reactions)		A^0	α	E
1	$O^{\times}(YSZ)+(YSZ) \Leftrightarrow O^{2-}(YSZ)+V^{\bullet\bullet}(YSZ)$	1.6×10^{22}	0	90.9
2	$O^{2-}(YSZ)+Ni(s) \Leftrightarrow O(s)+(YSZ)+2e^{-}(Ni)$	4.9×10^{-6}	0.5	*c*

Rate constant of Arrhenius equation written as: $k = AT^n\exp(-E/RT)$, the unit of E is kJ/mol.
c - Calculated or estimated from references.

8.4 NUMERICAL SOLUTION AND MODEL VALIDATION

According to the schematic in Figure 8.1, 2D axial symmetric computational domain is considered to model the button cell test system. The corresponding boundary conditions are summarized in Table 8.2. The model parameters and boundary conditions are shown in Table 8.3 and Table 8.4 respectively. The mathematical model is solved using commercial package of COMSOL MULTIPHSICS V4.1. For a specified cell voltage at O_2 electrode boundary, the corresponding average cell current density and gas

species distributions are calculated. By specifying a series of cell voltages, the cell polarization curve can be obtained. Figure 8.2 illustrates the comparison between the model predictions and the experimental results at two temperatures of 850°C and 900°C, where 60% steam and 40% hydrogen is used as the supplied gas for H_2 electrode. The model predictions show reasonably good match with experimental data. This model is utilized for further simulation studies.

Table 8.2 Reaction rates and Source terms

Net reaction rate of adsorbates	Reaction source term	Energy source term
$r_{CH4(s)} = r_3 - r_{14} - r_{18}$	$R_{H_2} = -2r_1$	$R_{Ca} = Q_{ohm} + Q_{Elec/chem}$
$r_{CH3(s)} = r_{14} - r_{15} + r_{18} - r_{19}$	$R_{CH_4} = -r_2$	$R_{El} = Q_{ohm}$
$r_{CH2(s)} = r_{15} - r_{16} + r_{19} - r_{20}$	$R_{H_2O} = -r_4$	$R_{An} = Q_{ohm} + Q_{Elec/chem}$
$r_{CH(s)} = r_{16} - r_{17} + r_{20} - r_{21}$	$R_{CO_2} = -r_5$	$R_{Cl} = 0$
$r_{C(s)} = -r_{10} + r_{17} + r_{21}$	$R_{CO} = -r_6$	
$r_{CO(s)} = r_6 + r_{10} - r_{11} + r_{12}$		
$r_{CO2(s)} = r_5 + r_{11}$		
$r_{H(s)} = 2r_1 - r_7 - r_8 + r_{12} + r_{14} + r_{15} + r_{16} + r_{17}$		
$r_{OH(s)} = r_7 - r_8 - r_9 + r_{13} + r_{18} + r_{19} + r_{20} + r_{21}$		

8.5 RESULTS AND DISCUSSION

8.5.1 The distribution of gas species and local potential/current

Figure 8.3 shows the molar fraction distributions of various gas species within the SOEC system, where the gas composition at the inlet of H_2 electrode is composed of

25%H_2O, 25%H_2, 25%CO_2 and 25%CO, and the O_2 electrode is exposed to the ambient air. The operating temperature of the furnace is 850^{o}C and the cell voltage is set at 1.2V

Table 8.3 Operation parameters

	Value	Units
Cathode layer thickness, radius	4×10^{-5}, 2.5×10^{-3}	m
Electrolyte layer thickness, radius	2×10^{-5}, 6.5×10^{-3}	m
Anode layer thickness, radius	3.5×10^{-4}, 6.5×10^{-3}	m
Inlet fuel channel radius, wall radius	1×10^{-3}, 1.5×10^{-3}	m
Outlet fuel channel radius	6.5×10^{-3}	m
Faraday Constant	96500	$C\cdot mol^{-1}$
Gas constant	8.314	$J\cdot mol^{-1}K^{-1}$
Operating Temperature	700	^oC
Pressure	1	atm
Anode ionic conductivity	$3.34\times10^4\exp(-10300/T)$	$S\cdot m^{-1}$
Cathode ionic conductivity	$3.34\times10^4\exp(-10300/T)$	$S\cdot m^{-1}$
Anode electronic conductivity	2×10^6	$S\cdot m^{-1}$
Cathode electronic conductivity	$42\times10^6\exp(-1150/T)/T$	$S\cdot m^{-1}$
Electrolyte ionic conductivity	$3.34\times10^4\exp(-10300/T)$	$S\cdot m^{-1}$
Porosity(ε)	0.4	1
Particle diameter	2×10^{-6}	m
Tortuosity	$(\frac{3-\varepsilon}{2})^{0.5}$	1
Permeability	$\frac{\varepsilon^3 d^2}{150(1-\varepsilon)^2}$	1
Inlet velocity	0.2	$m\cdot s^{-1}$
Surface site density of Ni	6.1×10^{-9}	$mol\cdot cm^{-2}$
Specific three-phase boundary length	1.8×10^{12}	$m\cdot m^{-3}$

as an example. Obviously at H_2 electrode side, the molar fractions of H_2O and CO_2 decrease from the inlet toward the electrode/electrolyte interface while those of H_2 and CO increase. At the O_2 electrode side, O_2 is produced. Since the thickness of O_2 electrode is very thin, the molar fraction distribution of O_2 is relatively uniform. The corresponding distributions of electronic/ionic potential and current density are shown in Figure 8.4. It can be seen that the electronic potential is pretty uniform, which approaches to zero

within H_2 electrode and maintains at the specified voltage of 1.2V within the O_2 electrode. The ionic potential distribution in the H_2 electrode is not uniform with the highest potential at the electrode/electrolyte interface and decreases towards the electrode/channel interface and circumference. Accordingly the electronic current density decreases from channel/electrode interface towards electrode/electrolyte interface while the ionic current density decreases from the electrode/electrolyte interface towards channel/electrode interface.

Table 8.4 Boundary conditions

Interfaces(Ω)	$\Omega_{Ca/Cl}$	$\Omega_{Ca/El}$	$\Omega_{El/An}$	$\Omega_{An/Cl}$	Ω_{Cl}
Ionic charge	Insulation	Continuity	Continuity	Insulation	N/A
Electronic charge	Specified voltage	Insulation	Insulation	0	N/A
Mass	O_2/N_2 (Mass fractions)	Insulation	Insulation	Continuity	H_2O/CO_2 (Mass fraction)
Momentum	Pressure	Wall (no slip)	Wall (no slip)	Continuity	Flow rate, pressure
Energy	Temperature	Continuity	Continuity	Continuity	Temperature

8.5.2 The distribution of adsorbed species within H_2 electrode

In this section, the operating conditions for the simulation are the same as those in section 4.1. The distributions of adsorbed species within the H_2 electrode are shown in Figure 8.5. It can be seen that within the H_2 electrode the surface coverage of the adsorbed $H_2O(s)$, $OH(s)$, and $CO_2(s)$ ions decrease from the electrode/electrolyte interface towards the channel/electrode interface. The surface coverage of intermediate

products H(s) and CO(s) show opposite trends. The highest surface coverage gradient of

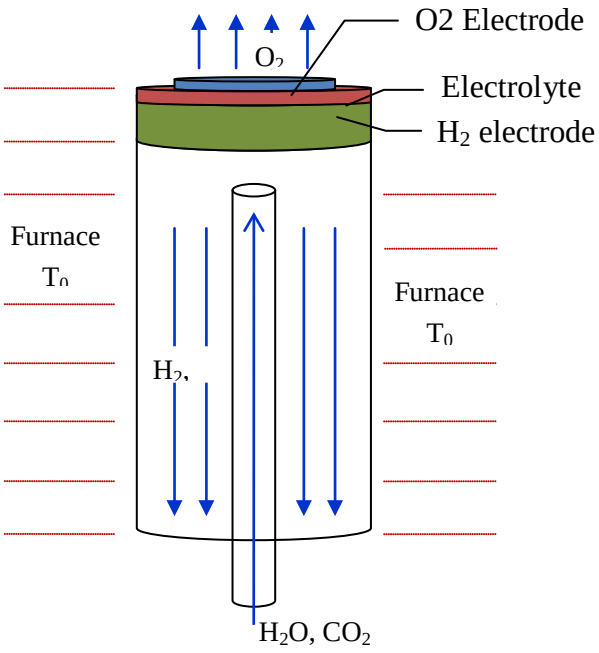

Figure 8.1 Schematic of the gas flow and SOEC operation

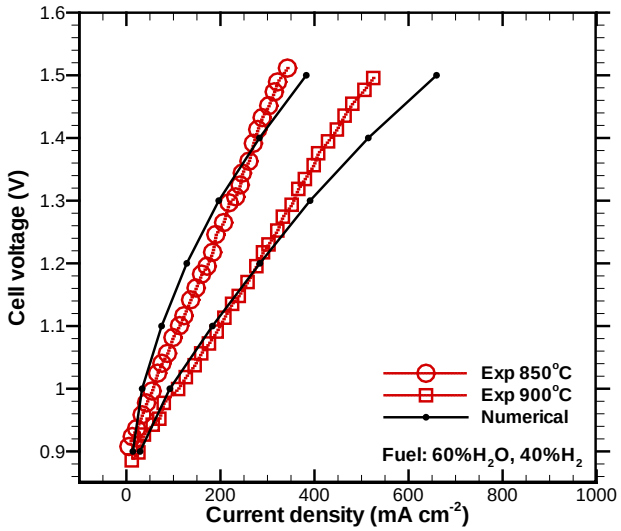

Figure 8.2 Comparison between numerical results and experimental data

adsorbates presents at the electrode/electrolyte interface. This observation indicates that the intensity of surface electrolysis processes is much higher at this interface than other places, which is consistent with the distributions of bulk species in Figure 8.3. The

surface coverage of the adsorbed O(s) ions decreases from the channel/electrode interface towards the electrode/electrolyte interface, indicating that more O(s) ions are

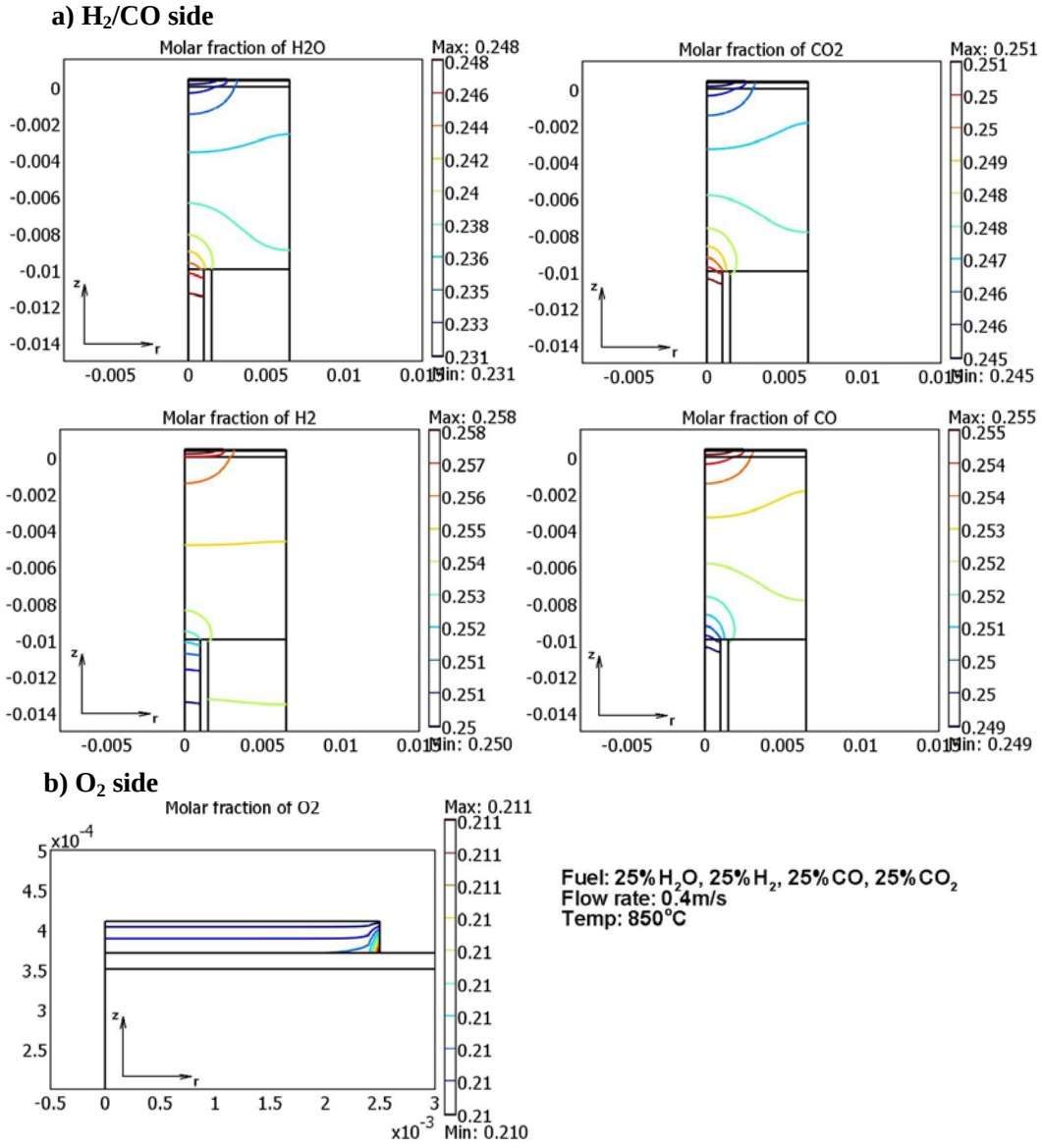

Figure 8.3 The distributions of gas species within gas supply tube and cell electrodes

converted into O^{2-}(s) ions and then conducted into electrolyte layer at the electrode/electrolyte interface. This result further confirms that electrolysis process is relatively intensive at the electrode/electrolyte interface. Theoretically, the CO can be

further electrolyzed to generate carbon. The generated carbon could be adsorbed onto the Ni surface. As shown in Figure 8.6, the carbon deposition effect could present around the electrode/electrolyte interface, where the most intensive electrolysis reactions take place.

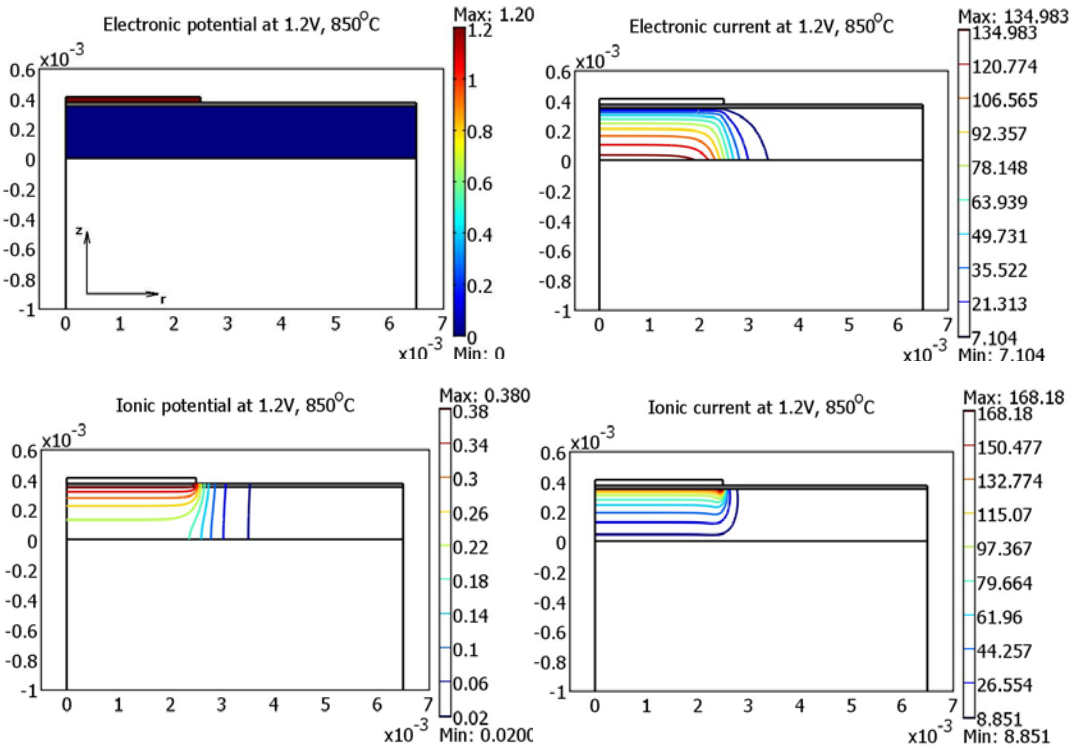

Figure 8.4 The distributions of local electronic/ionic potential and current within H_2 electrode

8.5.3 The effect of operating temperature

In this section, the operating conditions for the simulation are the same as those in section 4.1 except that three furnace temperatures of 800°C, 850°C, and 900°C are applied respectively. Figure 8.7 shows the distribution of surface adsorbed species, where the data are recorded along the axis-symmetrical line of the cell. It can be seen that increasing temperatures leads to the decrease of surface coverage of all intermediate adsorbates, including H_2O(s), O(s) and CO_2(s) ions as well as H(s), and CO(s) ions. In

other words, less $H_2O(s)$, $O(s)$, $CO_2(s)$, $H(s)$, and $CO(s)$ ions are adsorbed on the Ni surface when operating temperature increases. It is also noticed that less C(s) is generated, suggesting that high operating temperature may potentially mitigate carbon deposition on Ni surface. These observations indicate that operating temperature may effectively improve adsorption/desorption rate and enhance surface electrolysis process. The surface process in turn affects the consumption and production of bulk gas species. As shown in Figure 8.8. Higher temperature leads to the consumption of more H_2O and CO_2 while producing more O_2, H_2 and CO.

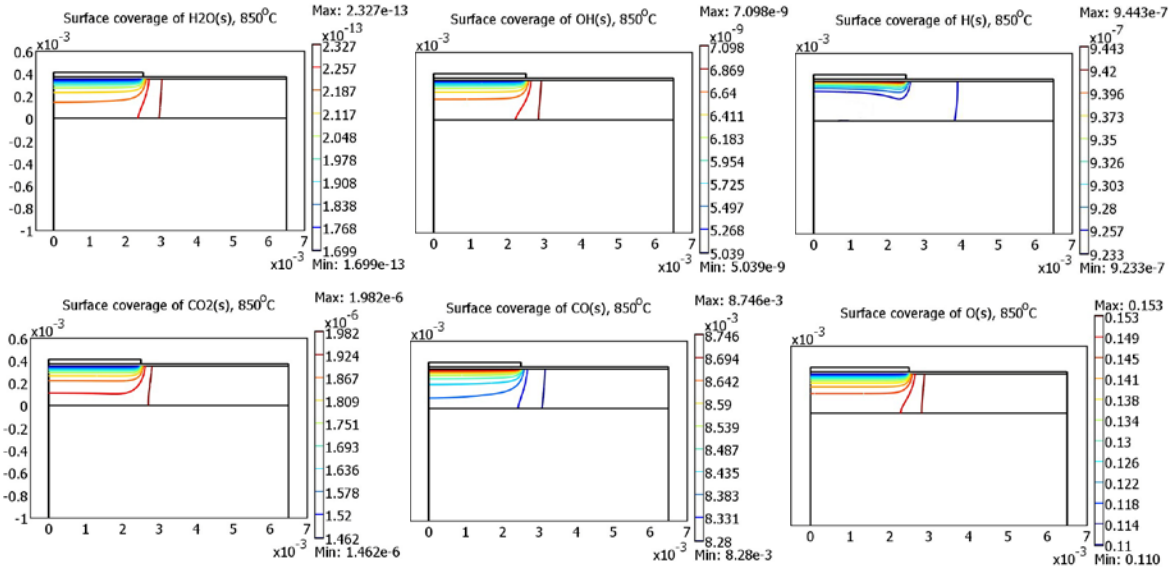

Figure 8.5 The distributions of adsorbed species within H_2 electrode

8.5.4 The effect of operating voltage

In this section, the operating conditions for the simulation are the same as those in section 4.1 except that different cell voltages are applied. As shown in Figure 8.9, increasing the applied cell voltage leads to the decrease of the adsorbed $H_2O(s)$, $O(s)$, $H(s)$ and $CO_2(s)$ ions; but it causes the enhancement of the surface coverage of CO(s) and C(s).

When the cell voltage increases the reaction rates of forward surface processes exceed those of backward processes, resulting in the improved surface electrolysis processes. Since the surface coverage of C(s) are significantly enhanced under high cell voltage conditions, more than likely the deposition of carbon on the surface of Ni catalyst might also be enriched. Figure 8.10 shows molar fraction distributions of bulk gas. Obviously more H_2O and CO_2 are consumed through adsorption/desorption process under higher cell voltage while more O_2, H_2 and CO are produced.

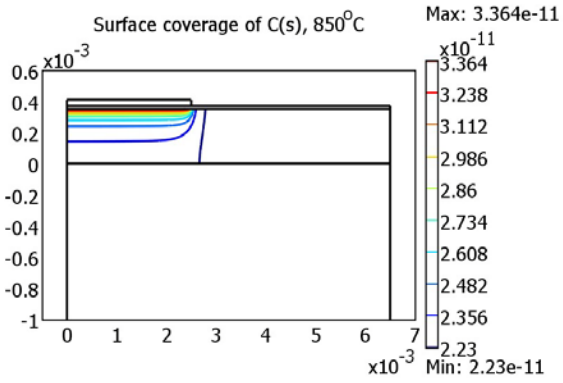

Figure 8.6 The distribution of adsorbed carbon generated by electrolysis process in H_2 electrode

8.5.5 The effect of supplied gas composition

H_2O and CO_2 are two major supplied gases for syngas production. The effects of supplied gas compositions on surface electrolysis performance are studied in this section. The operating conditions for the simulations are still the same as those in section 4.1 except that the supplied gas compositions are varied. In the first case study, the effect of H_2O content is investigated. The starting gas composition includes 20%CO_2, 20%CO, 20%H_2 and 5%H_2O with N_2 as a balance species. With increasing the H_2O from 5% to

35% (the N_2 content is reduced accordingly), the variations of intermediate adsorbates

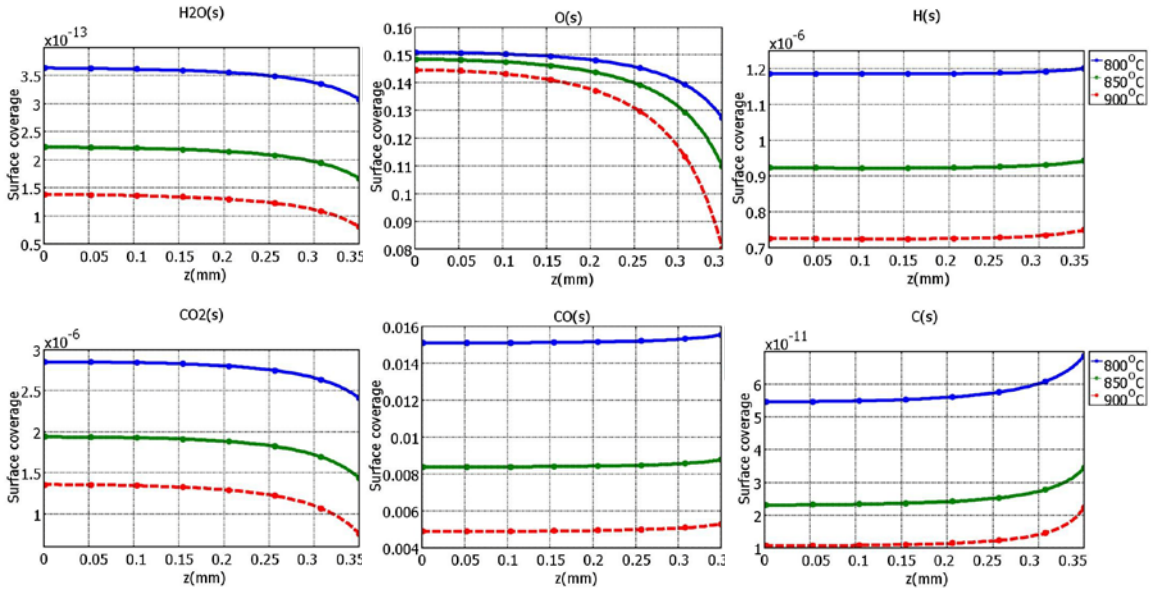

Figure 8.7 The effects of operating temperature on the distribution of adsorbates along the axis-symmetrical line of the cell

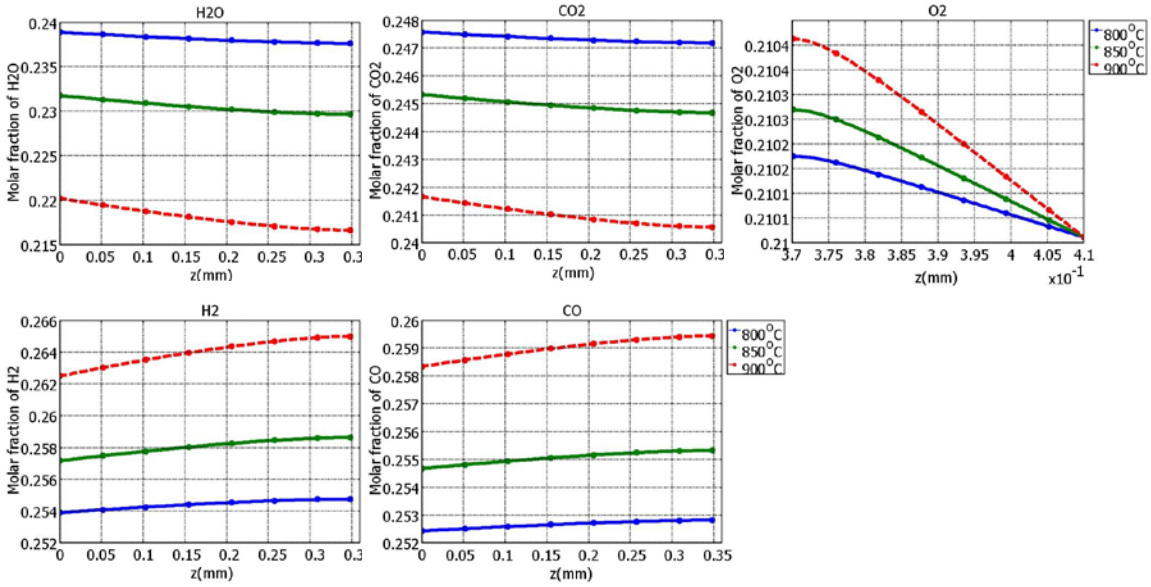

Figure 8.8 The effects of operating temperature on the distribution of gas species along the axis-symmetrical line of the cell

are shown in Figure 8.11. Obviously the adsorbed H_2O(s), OH(s) and H(s) ions are enhanced, however, the variations of the adsorbed CO_2(s), CO(s) and C(s) ions are

negligible. This result indicates that increasing the supplied H_2O content might not be able to effectively mitigate the carbon coking problem in H_2 electrode. In the second case

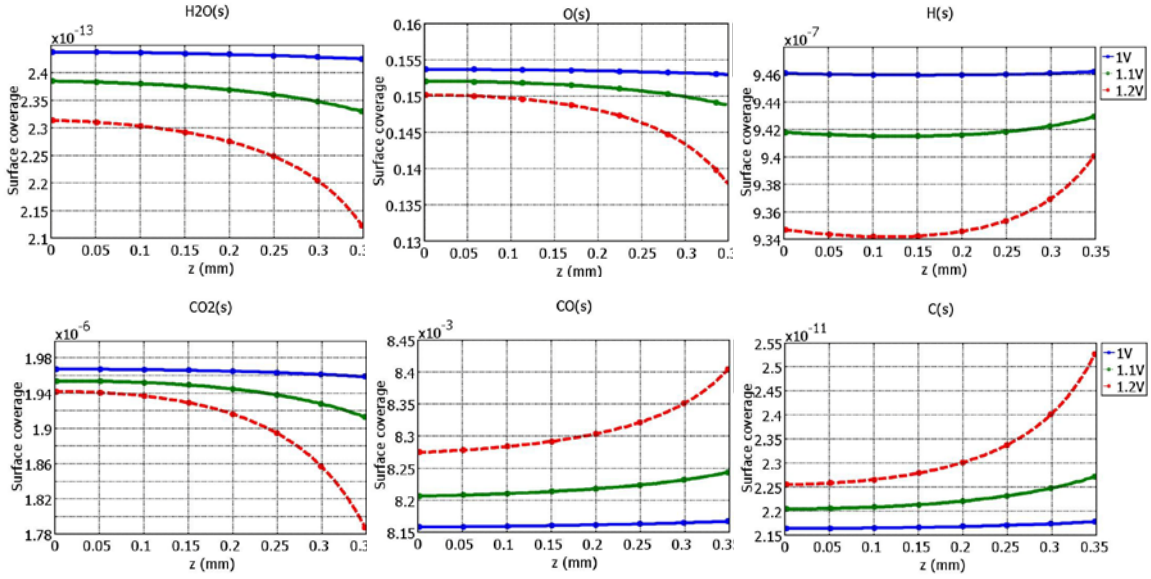

Figure 8.9 The effects of applied cell voltage on the distribution of adsorbates along the axis-symmetrical line of the cell

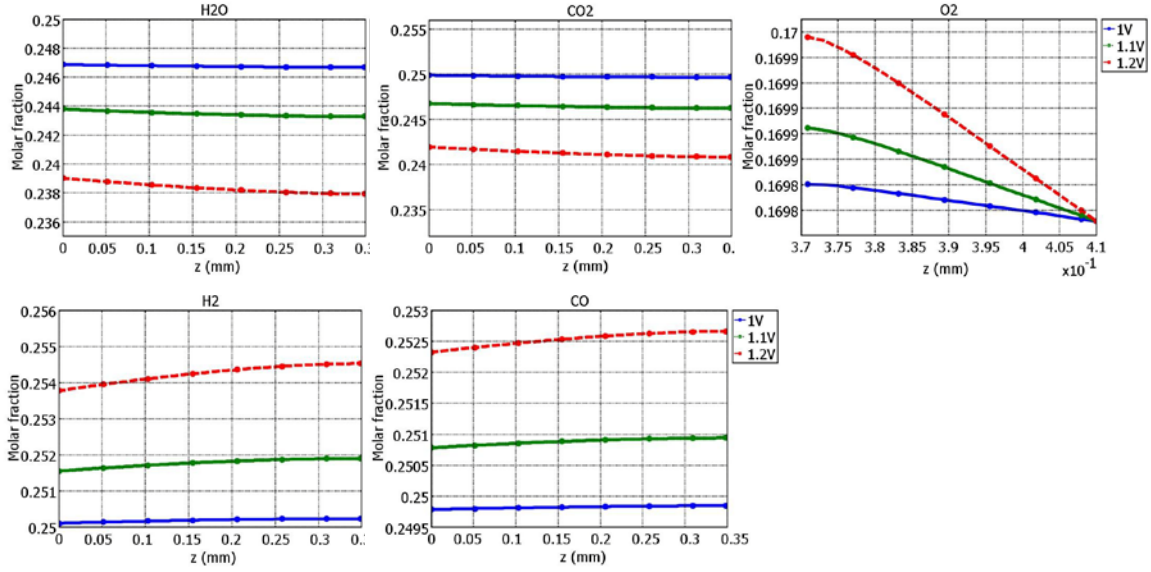

Figure 8.10 The effects of applied cell voltage on the distribution of gas species along the axis-symmetrical line of the cell

study, the effects of CO_2 content on surface electrolysis are investigated. The starting supplied gas composition consists of 20%H_2O, 20%CO, 20%H_2 and 5%CO_2 with N_2 as

the balance species. When the CO_2 content increases from 5% to 35% (the N_2 content is reduced accordingly), the variations of adsorbed surface ions are shown in Figure 8.12.

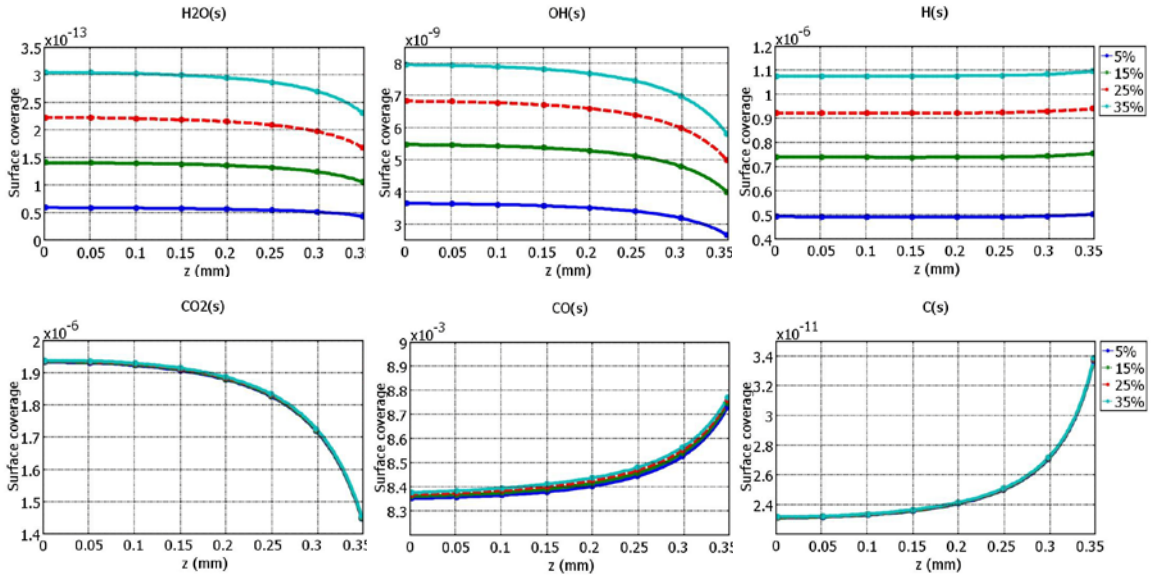

Figure 8.11 The effects of H_2O content on the distribution of adsorbates along the axis-symmetrical line of the cell

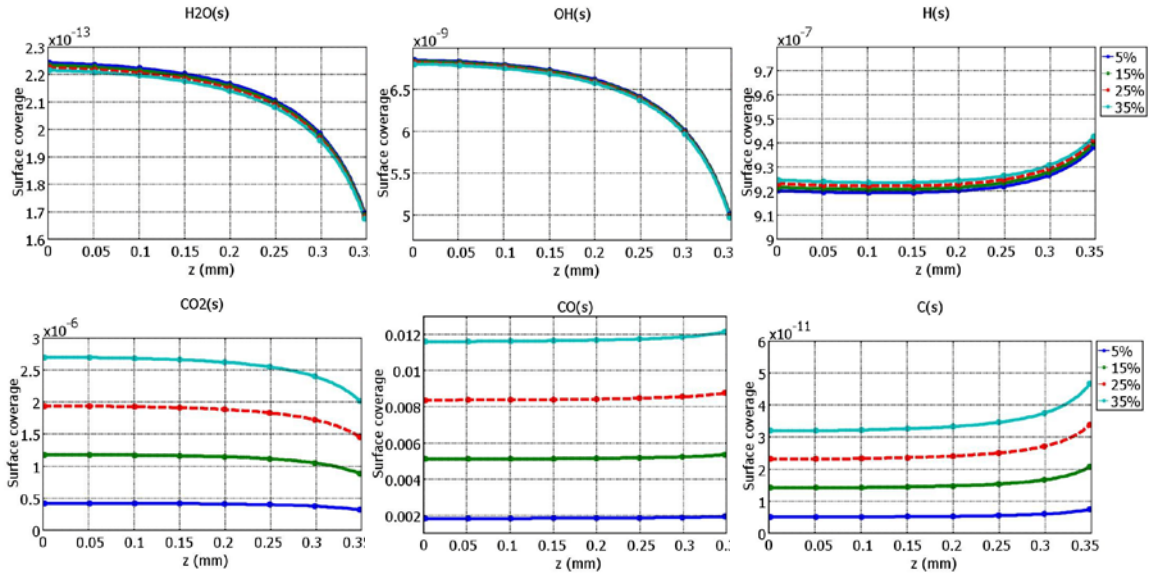

Figure 8.12 The effects of CO_2 content on the distribution of adsorbates along the axis-symmetrical line of the cell

With increasing the CO_2 content, the adsorbed CO_2(s), CO(s) and C(s) ions are obviously improved, there is little effect on the surface coverage of H_2O(s), OH(s) and H(s) ions.

The comparison of above two cases suggests that that the surface electrolysis processes of CO_2 and H_2O are pretty much independent with each other. The carbon coking effect is mainly determined by the fraction of CO_2 in the H_2 electrode.

8.6 CONCLUSION

A SOEC electrolysis model for syngas gas production is developed. The model integrates the multi-transport processes of charge, mass, momentum and energy with the detailed surface chemistry. The model is validated using the experimental data at 850^oC and 900^oC conditions. Upon the model validation, numerical simulations are extensively performed with emphasis on surface electrolysis processes. The major conclusions from this paper include: (1) the intensity of surface electrolysis processes appears to be strong at the H_2 electrode/electrolyte interface even though the composite electrode is assumed; (2) the surface electrolysis processes of CO_2 and H_2O are pretty much independent with each other; (3) The carbon coking effect is mainly determined by the fraction of CO_2 in the H_2 electrode; (4) high cell voltage conditions may cause the enhancement of the surface coverage of C(s) and the deposition of carbon on the surface of Ni catalyst; (5) high operating temperature may effectively improve adsorption/desorption rate, and enhance surface electrolysis process as well as potentially mitigate carbon deposition on Ni surface.

CHAPTER 9

SUMMARY AND OUTLOOK

9.1 SUMMARY

In this dissertation, multi-physicochemical models have been developed for solid oxide fuel cells and electrolysis cells. The models describe the complicated transport processes of charge (electron/ion) conservation, mass/species conservation, momentum conservation, and energy conservation. Transport processes are coherently coupled with chemical reforming processes, surface elementary reaction processes, as well as electro-oxidation processes of both hydrogen and carbon monoxide. The models are validated with experimental data and utilized for fundamental mechanism studies of SOFCs fueled with different type of fuels, such as hydrogen, hydrocarbon (methane), H_2S, and their mixtures. The fundamental mechanisms associated with syngas generation using electrolysis cell are also extensively investigated using the developed model.

In Chapter 3, a direct H_2S fueled SOFC model is developed by coupling the detailed chemical reforming process of H_2S with the multi-physics processes in button cell and fuel supply test stand. Similarly, Chapter 4 presents a direct methane fueled SOFC, in which in which the methane reforming processes are coherently integrated with the multi-transport processes, and it takes into account the two electrochemical reaction

processes of hydrogen and carbon monoxide oxidations. Results show that suitable increasing the H_2O content in H_2S or methane fuel is able to improve SOFC electrochemical performance and potentially mitigate the sulfur poisoning or carbon coking effect. The operating condition effects on chemical reforming processes and the cell electrochemical performance are discussed.

The practical hydrocarbon fuels could have contaminant such as sulfur-containing compound. In order to simulate the contaminants involved in practical hydrocarbon fuels, the model of SOFCs fueled with mixture of hydrocarbon and H_2S is presented in Chapter 5. The model considers the detailed reforming process of both methane and H_2S as well as their interactions and couples these reforming processes with the multi-physics transport processes of button cell and associated fuel supply test stand. Numerical results show that the Nernst potential E_{H2} shows a strong correlation with the cell voltage, increasing with increasing the cell voltage. The E_{CO} shows a weak dependence on the cell voltage, especially at the anode/electrolyte interface. Suitable H_2S content in CH_4 fuel is beneficial to improve the reforming of CH_4 and SOFC electrochemical performance particularly H_2-H_2O electro-oxidation process. Increasing the fuel flow rate may mitigate the carbon deposition and sulfur poisoning effects. The operating temperature and fuel composition show the conflicting roles on mitigating carbon deposition and sulfur poisoning effects. Increasing the temperature may mitigate the carbon deposition effects but potentially worsen the sulfur poisoning effect. Decreasing the H_2S content in the CH_4 fuel may significantly mitigate the sulfur

poisoning effect but increase the possibility of carbon deposition effect.

To incorporate the details of surface adsorption/desorption processes in porous electrodes and the associated surface chemistry, the models that link the detailed elementary reaction kinetics with multi-physics transport processes are developed. The hydrogen-fueled SOFC model is present in Chapter 6, followed by the methane-fueled multi-physicochemical model in Chapter 7. Simulation results indicate that very complicated interactions exist among fuel/gas transport in porous electrodes, adsorbed/desorbed species on the surface of porous electrodes, and charge transport through solid backbone, as well as elementary reactions. The adsorbed surface species are very sensitive to the variations of the supplied hydrogen and oxygen as well as the cell voltage. To mitigate potential surface carbon deposition, simulation results suggest several ways: (1) suitably increase H_2O content in the fuel; (2) reduce the content of CH_4, CO, CO_2 in the supplied fuel; (3) increase the operating temperature; (4) increase the cell operating current; (5) improve exchange current density of anode and/or cathode electrode.

Chapter 8 presents a multi-physicochemical model of solid oxide electrolysis cell for syngas generation. Upon the model validation with experimental data, numerical simulations are extensively performed with emphasis on surface electrolysis processes. The results indicate that: (1) the intensity of surface electrolysis processes appears to be strong at the H_2 electrode/electrolyte interface even though the composite electrode is assumed; (2) the surface electrolysis processes of CO_2 and H_2O are pretty much

independent with each other; (3) The carbon coking effect is mainly determined by the fraction of CO_2 in the H_2 electrode; (4) high cell voltage conditions may cause the enhancement of the surface coverage of C(s) and the deposition of carbon on the surface of Ni catalyst; (5) high operating temperature may effectively improve adsorption/desorption rate, and enhance surface electrolysis process as well as potentially mitigate carbon deposition on Ni surface.

9.2 OUTLOOK

The SOFC is one of the feasible technologies toward the clean and sustainable energy solutions. There are very complicated transport processes, chemical reforming processes and electrochemical processes in SOFC and electrolyzer systems. These processes are multi-scale in nature. Therefore it is envisioned that multi-scale multi-physicochemical models may provide more accurate predictions for SOFC/electrolyzer performance and associated processes. The model validation is critical step, upon which high fidelity simulations are performed. It is still a challenge issue on how to comprehensively validate the multi-physicochemical models.

`

REFERENCE

[1] Y. Katayama, Y. Tamaura, "Development of new green-fuel production technology by combination of fossil fuel and renewable energy", Energy, 30(11-12), 2005, 2179-2185;

[2] L. Liu, S.Y. Cheng, J.B. Li, "Mitigating environmental pollution and impacts from fossil fuels: the role of alternative fuels", Energy sources part A- Recovery utilization and environmental effects, 29(12), 2007, 1069-1080;

[3] NQ. Minh, "Ceramic fuel cells", Journal of The American Ceramic Society, 76(3), 1993, 563-588;

[4] SC. Singhal, "Solid oxide fuel cells for stationary, mobile, and military applications", Solid State Ionics, 152(2002), 405-410;

[5] G.F. Mclean, T. Niet, S.P. Richard, "An assessment of alkaline fuel cell technology", International Journal of Hydrogen Energy, 27(5), 2002, 507-526;

[6] J.R. Varcoe, RCT. Slade, "Prospects for alkaline anion-exchange membranes in low temperature fuel cells", Fuel Cells, 5(2), 2005, 187-200;

[7] C. Coutanceau, L. demarconnay, C. Lamy, "Development of electrocatalysts for solid alkaline fuel cell", Journal of Power Sources, 156(1), 2006, 14-19;

[8] J. Roziere, DJ. Jones, "Non-fluorinated polymer materials for proton exchange membrane fuel cells", Annual Review of Materials Research, 33(2003), 503-555;

[9] V. Gurau, HT. Liu, S.Kakac, "Two-dimensional model for proton exchange membrane fuel cells", Aiche Journal, 44(11), 1998, 2410-2422;

[10] TV. Nguyen, RE. White, "A water and heat management model for proton exchange membrane fuel cells", Journal of The Electrochemical Society, 140(8), 1993, 2178-2186;

[11] S. Wasmus, A. Kuver, "Methanol oxidation and direct methanol fuel cells: a selective review", Journal of Electroanalytical Chemistry, 461(1-2), 1999, 14-31;

[12] HS. Liu, CJ. Song, L. Zhang, "A review of anode catalysis in the direct methanol fuel cell", Journal of Power Sources, 155(2), 2006, 95-110;

`

[13] A. Hamnett, "Mechanism and electrocatalysis in the direct methanol fuel cell", Catalysis Today, 38(4), 1997, 445-457;

[14] S. Cavallaro, N. Mondello, S. Freni, "Hydrogen produced from ethanol for internal reforming molten carbonate fuel cell", Journal of Power Sources, 102(1-2), 2001, 198-204;

[15] NJ. Cherepy, R. Krueger, KJ. Fiet, "Direct conversion of carbon fuels in a molten carbonate fuel cell", Journal of The Electrochemical Society, 152(1), 2005, A80-A87;

[16] S. Cavallaro, S. Freni, "Ethanol steam reforming in a molten carbonate fuel cell: a preliminary kinetic investigation", International Journal of Hydrogen Energy, 21(6), 1996, 465-469;

[17] P. Stonehart, "Development of alloy electrocatalysts for phosphoric acid fuel cells", Journal of Applied electrochemistry, 22(11), 1992, 995-1001;

[18] M. Watanabe, K. Tsurumi, T. Mizukami, "Activity and stability of ordered and disordered Co-Pt alloys for phosphoric acid fuel cells", Journal of The Electrochemical Society, 141(10), 1994, 2659-2668;

[19] M. Razaq, A. Razaq, E. Yeager, "Perfluorosulfonimide as an additive in phosphoric acid fuel cell", Journal of The Electrochemical Society, 136(2), 1989, 385-390;

[20] O. Yamamoto, "Solid oxide fuel cells: fundamental aspects and prospects", 45(15-16), 2000, 2423-2435;

[21] SC. Singhal, "Advances in solid oxide fuel cell technology", Solid state ionics, 135(1-4), 2000, 305-313;

[22] S. Mclntosh, RJ. Gorte, "Direct hydrocarbon solid oxide fuel cells", Chemical Reveiws, 104(10), 2004, 4845-4865;

[23] SD. Park, JM.Vohs, RJ. Gorte, "Direct oxidation of hydrocarbons in solid oxide fuel cell", Nature, 404(6775), 2000, 265-267;

[24] ZP. Shao, SM. Haile, "A high-performance cathode for the next generation of solid oxide fuel cells", Nature, 431(7005), 170-173;

[25] SB. Adler, "Factors governing oxygen reduction in solid oxide fuel cell cathodes", Chemical Reveiws, 104(10), 2004, 4791-4843;

[26] J. Will, A. Mitterdorfer, C. Kleinlogel, "Fabrication of thin electrolytes for second generation solid oxide fuel cells", Solid State Ionics, 131(1-2), 2000, 79-96;

`

[27] YH. Huang, RI. Dass, ZL. Xing, "Double perovskites as anode materials for solid oxide fuel cells", Science, 312(5771), 2006, 254-257;

[28] RM. Ormerod, "Solid oxide fuel cells", Chemical Society Reviews, 32(1), 2003, 17-28;

[29] J. Vanherle, F. Marechal, S. Leuenberger, "Process flow model of solid oxide fuel cell system supplied with sewage biogas", Journal of Power Sources, 131(1-2), 2004, 127-141;

[30] A. Burke, L. Carreiro, "System modeling of an air-independent solid oxide fuel cell system for unmanned undersea vehicles", Journal of Power Sources, 158(1), 428-435;

[31] S.T. Won, S.J. Lak, K.J. Hwan, K.T. Seop, R.T. Sung, S.Kenjiro, "Performance analysis of a tubular solid oxide fuel cell/micro gas turbine hybrid power system based on a quasi-two dimensional model", Journal of Power Sources, 142(1-2), 2005, 30-42;

[32] A.Virkar, "A model for solid oxide fuel cell stack degradation", Journal of Power Sources, 172(2), 2007, 713-724;

[33] K.P. Recknagle, M.E. Ryan, J.B. Koeppel, "Modeling of electrochemistry and steam-methane reforming performance for simulating pressurized solid oxide fuel cell stacks", Journal of Power Sources, 195(19), 2010, 6637-6644;

[34] J. Yang, X. Li, J. Jiang, "Parameter optimization for tubular solid oxide fuel cell stack based on the dynamic model and an improved genetic algorithm", International Journal of Hydrogen Energy, 36(10), 2011, 6160-6174;

[35] H. Yakabe, M. Hishinuma, M. Uratani, "Evaluation and modeling of performance of anode-supported solid oxide fuel cell" Journal of Power Sources, 86(1-2), 2000, 423-431;

[36] D.J. Hall, R.G. Colclaser, "Transient modeling and simulation of a tubular solid oxide fuel cell", IEEE Transactions on Energy Conversion, 14(3), 1999, 749-753;

[37] S.H. Chan, Z.T. Xia, "Anode micro model of solid oxide fuel cell", Journal of The Electrochemical Society, 148(4), 2001, A338-A394;

[38] S. Kakac, A. Pramuanjaroenkij, X. Zhou, "A review of numerical modeling of solid oxide fuel cell", International Journal of Hydrogen Energy, 32(7), 2007, 761-786;

[39] C. Paola, C. Paolo, A. vincenzo, "Micro-modeling of solid oxide fuel cell electrodes", Electrochimica Acta, 43(3-4), 1998, 375-394;

[40] S.B. Adler, J.A. Lane, B.C.H. Steele "Electrode kinetics of porous mixed conducting

oxygen electrodes", Journal of The Electrochemical Society, 143(11), 1996, 3354-3564;

[41] Y. Shi, N. Cai, C.Li, "Numerical modeling of anode-supported SOFC button cell considering anodic surface diffusion", Journal of Power Sources, 164(2007), 639-648;

[42] A.C. King, J. Billingham, R.J. Cooper, "Performance modeling of solid oxide fuel cells", Combustion Theory and Modelling, 5(4), 2001, 639-667;

[43] P. Aguiar, D. Chadwick, L. Kershenbaum, "Modeling of an indirect internal reforming solid oxide fuel cell", Chemical Engineering Science, 57(10), 2002, 1665-1677;

[44] C. Colpan, I. Dincer, F. Hamdullahpur, "Thermodynamic modeling of direct internal reforming solid oxide fuel cells operating with syngas", International Journal of Hydrogen Energy, 32(7), 2007, 787-795;

[45] A. Bieberle, L.P. Meier, L.J. Gauckler, "The electrochemistry of Ni pattern anodes used as solid oxide fuel cell model electrodes", Journal of The Electrochemical Society, 148(6), 2001, A646-A656;

[46] V.M.Janardhanan, O. Deutschmann, "CFD analysis of a solid oxide fuel cell with internal reforming coupled interactions of transport, heterogeneous catalysis and electrochemical processes", Journal of Power Sources, 162(2006), 1192-1202;

[47] A.S. Loselevich, A.A. Kornyshev, "Phenomenological theory of solid oxide fuel cell anode", Fuel cells, 1(2001), 40-46;

[48] D.Sanchez, R. Chacartegui, A. Munoz, "On the effect of methane internal reforming modeling in solid oxide fuel cells", International Journal of Hydrogen Energy, 33(7), 2008, 1834-1844;

[49] P. Hofmann, K.D. Panopoulos, L.E. Fryda, "Comparison between two methane reforming models applied to a quasi two dimensional planar solid oxide fuel cell model", Energy, 34(12), 2009, 2151-2157;

[50] J.Zaman, A.Chakma, "Production of hydrogen and sulfur from hydrogen sulfide", Fuel Process Technology, 41(1995), 159-198;

[51] K.Sasakl, K.Susuki, A.Iyoshi, M.Uchimura, N.Imamura, H.Kusaba, Y.Teraoka, H.Fuchino, K.Tsujimoto, Y.Uchida, N.Jingo, " H_2S poisoning of solid oxide fuel cells", Journal of The Electrochemical Society, 153(11), 2006, A2023-A2029;

[52] L. Aguilar, Z. Shaowu, Z. Cheng, J. Winnick, M. Liu, "A solid oxide fuel cell operating on hydrogen sulfide and sulfur containing fuels", Journal of Power Sources,

`

135(2004), 17-24;

[53] N.M. Galea, E.S. Kadantsev, T. Ziegler, "Studying reduction in solid oxide fuel cell activity with density functional theory: effects of hydrogen sulfide adsorption on Ni anode surface", Journal of Physical Chemistry, 111(C), 2007, 14457-14468;

[54] F.P. Nagel, T.J. Schildhauer, J.Sfeir, A. Schuler, S.M.A. Biollaz, "The impact of sulfur on the performance of a solid oxide fuel cell system operated with hydrocarboneous fuel gas", Journal of Power Sources, 189(2009), 1127-1131;

[55] T. Hibino, A. Hashimoto, T. Inoue, J. Tokuno, S. Yoshida, M. Sano, "A low operating temperature solid oxide fuel cell in hydrocarbon air mixtures", Science, 288(5473), 2000, 2031-2033;

[56] C. Graves, S.D. Ebbesen, M. Mogensen, "Co-electrolysis of CO_2 and H_2O in solid oxide fuel cells: Performance and durability", Solid State Ionics, 192(1), 2010, 398-403;

[57] Z.L. Zhan, W. Kobsiriphat, J.R. Wilson, M. Pilai, I. Kim, S.A. Barnett, "Syngas production by co-electrolysis of CO_2/H_2O: the basis for a renewable energy cycle", Energy Fuels, 23(2009), 3089-3096;

[58] M. Ni, M.K.H. Leung, D.Y.C. Leung, "Parametric study of solid oxide steam electrolyzer for hydrogen production", International Journal of Hydrogen Energy, 32(2007), 2305-2313;

[59] M. Ni, M.K.H. Leung, D.Y.C. Leung, "Electrochemical modeling of hydrogen production by proton conducting solid oxide steam electrolyzer", International Journal of Hydrogen Energy, 33(2008), 4040-4047;

[60] G. Hawkes, J. O'Brien, C. Stoots, B. Hawkes, "3D CFD model of a multi-cell high temperature electrolysis stack", International Journal of Hydrogen Energy, 34(2009), 4189-4197;

[61] G. Tao, K.R. Sridhar, C.L. Chan, "Study of carbon dioxide electrolysis at electrode/electrolyte interface: part I. Pt/YSZ interface", Solid State Ionics, 175(2004), 615-619;

[62] G. Tao, K.R. Sridhar, C.L. Chan, "Study of carbon dioxide electrolysis at electrode/electrolyte interface: part II. Pt/YSZ cermet/YSZ interface", Solid State Ionics, 175(2004), 621-624;

[63] K.R. Sridhar, B.T. Vaniman, "Oxygen production on Mars using solid oxide electrolysis", Solid State Ionics, 97(1997), 147-152;

`

[64] V. Yurkiv, D. Starukhin, H.-R. Volpp, W. G. Bessler, "Elementary reaction kinetics of the CO/CO2/Ni/YSZ electrode", Journal of the Electrochemical Society, 158(1), 2011, B5-B10;

[65] E. S. Hecht, G. K. Gupta, H. Y. Zhu, A. M. Dean, R. J. Kee, L. Maier, O. Deutschmann, "Methane reforming kinetics within a Ni-YSZ SOFC anode support", Applied Catalysis A: General, 295(2005), 40-51;

[66] E.L.Cussler, Diffusion Mass Transfer in Fluid System, 3rd edition, 2007, Cambridge University;

[67] M.Andersson, J.Yuan, B.Sunden, "SOFC modeling considering electrochemical reactions at the active three phase boundaries", International Journal of Heat and Mass Transfer, 55(2012), 773-788;

[68] P.Ponticel, "Fueling the fuel cell", Automotive Engineering International, 3(2000), 170-172;

[69] W. G. Bessler, S. Gewies, M. Vogler, "A new framework for physical based modeling of solid oxide fuel cell", Electrochimica Acta, 53(2007), 1782-1800;

[70] W.G. Bessler, M. Vogler, H. Stormer, D. Gerthsen, A. Utz, A. Weber, E. Ivers-Tiffee, "Model anodes and anode models for understanding the mechanism of hydrogen oxidation in solid oxide fuel cell", Physical Chemistry Chemical Physics, 12(2010), 13888-13903;

[71] W. G. Bessler, S. Gewies, M. Vogler, "A new framework for physical based modeling of solid oxide fuel cell", Electrochimica Acta, 53(2007), 1782-1800;

[72] H.Y. Zhu, A.M. Colclasure, R.J. Kee, Y.B. Lin, S.A. Barnett, "Anode barrier layers for tubular solid oxide fuel cells with methane fuel streams", Journal of Power Sources 161 (2006) 413–419;

[73] N.Laosiripojana, S.Assabumrungrat, "Catalytic steam reforming of methane, methanol, and ethanol over Ni/YSZ: The possible use of these fuels in internal reforming SOFC", Journal of Power Sources, 163(2007), 943-951;

[74] H.Y. Zhu, R.J. Kee, V. M. Janardhanan, O. Deutschmann, D.G. Goodwin, "Modeling elementary heterogeneous chemistry and electrochemistry in solid oxide fuel cells", Journal of the Electrochemical Society, 152(2005), A2427;

[75] A. Kirubakaran, S. Jain, R. K. Nema, "A review on fuel cell technologies and power electronic interface", Renewable and Sustainable Energy Reviews, 13(2009), 2430-2440;

`

[76] X.W. Zhang, S.H. Chan, G. Li, H.K.Ho, J. Li, Z. Feng, "A review of integration strategies for solid oxide fuel cell", Journal of Power Sources, 195(2010), 685-702;

[77] D.S.Monder, K.T.Chuang, K.Nandakumar, "A fully coupled multiphysics model for a H_2S SOFC", Journal of The Electrochemical Society, 157(4), 2010, B542-B551;

[78] S.Zha, Z.Cheng, M.Liu, "Sulfur poisoning and regeneration of Ni-based anodes in solid oxide fuel cells", Journal of The Electrochemical Society, 154(2), 2007, B201-B206;

[79] L.Yang, Z.Cheng, M.Liu, L.Wilson, "New insights into sulfur poisoning behavior of Ni-YSZ anode from long-term operation of anode-supported SOFCs", Energy & Environmental Science, 3(2010), 1804-1809;

[80] E.M.Ryan, W.Xu, X.Sun, M.A.Khaleel, "A damage model for degradation in the electrodes of solid oxide fuel cells: modeling the effects of sulfur and antimony in the anode", Journal of Power Sources, 210(2012), 233-242;

[81] H.Kishimoto, T.Horita, K.Yamaji, M.E.Brito, Y.P.Xiong, H.Yokokawa, "Sulfur poisoning on SOFC Ni anodes: Thermodynamic analysis within local equilibrium anode reaction model", Journal of The Electrochemical Society, 157(2010), B802-B813;

[82] G.J.Offer, J.Mermelstein, E.Brightman, N.P.Brandon, "Thermodynamics and kinetics of the interaction of carbon and sulfur with solid oxide fuel cell anodes", Journal of the American Ceramic Society, 92(4), 2009, 763-780;

[83] A.L.Vincent, J.L.Luo, K.T.Chuang, A.R.Sanger, "Promotion of activation of CH_4 by H_2S in oxidation of sour gas over sulfur tolerant SOFC anode catalysts", Applied Catalysis B: Environmental, 106(2011), 114-122;

[84] W. G. Bessler, M. Vogler, H. Stormer, D. Gerthsen, A. Utz, A. Weber, E. Ivers-Tiffee, "Model anodes and anode models for understanding the mechanism of hydrogen oxidation in solid oxide fuel cell", Physical Chemistry Chemcial Physics, 12(2010), 13888-13903;

[85] M. Vogler, A. Bieberle-Hutter, L. Gauckler, J. Warnatz, W. G. Bessler, "Modeling study of surface reactions, diffusion and spillover at a Ni/YSZ patterned anode", Journal of the Electrochemical Society, 156(6), 2009, B663-B672;

[86] J.H. Wang, M.L. Liu, "Surface regeneration of sulfur-poisoned Ni surfaces under SOFC operation conditions predicted by first-principle-based thermodynamic calculations", Journal of Power Sources, 176(2008), 23-30;

[87] N.Thilak Raj, S.Iniyan, R.Goic, "A review of renewable energy based cogeneration

technologies", Renewable and Sustainable Energy Reveiws, 15(2011), 3640-3648;

[88] J.M Klein, M.Henault, C.Roux, Y.Bultel, S.Georges, "Direct methane solid oxide fuel cell working by gradual internal steam reforming: Analysis of operation", Journal of Power Sources, 193(2009), 331-337;

[89] N.Laosiripojana, S.Assabumrungrat, "Catalytic steam reforming of methane, methanol, and ethanol over Ni/YSZ: The possible use of these fuels in internal reforming SOFC", 163(2007), 943-951;

[90] C.Gaudillere, P.Vernoux, C.Mirodatos, G.Caboche, D.Farrusseng, "Screening of ceria-based catalysts for internal methane reforming in low temperature SOFC", Catalysis Today, 157(2010), 263-269;

[91] J.Macek, B.Novosel, M.Marinsek, "Ni-YSZ SOFC anodes: Minimization of carbon deposition", Journal of the European Ceramic Society, 27(2007), 487-491;

[92] Yakabe, H., Ogiwara, T.Hishinuma, M. Yasuda I., "3-D model calculation for planar SOFC", Journal of power sources, 102(1-2), 144-154;

[93] Campanari S., Iora P., "Comparision of finite volume SOFC models for the simulation of a planar cell geometry", Fuel cells, 5(1), 34-51;

[94] Meng Ni, "Modeling of a solid oxide electrolysis cell for carbon dioxide electrolysis", Journal of power sources, 164(2010), 246-254;

[95] Meng Ni, Michael K.H.Leung, Dennis Y.C.Leung, "Technological development of hydrogen production by solid oxide electrolyzer cell (SOEC)", International journal of hydrogen energy, 33(2008), 2337-2354;

[96] N.Akhtar, S.P.Decent, D.Loghin, K.Kendall, "Mixed-reactant, micro-tubular solid oxide fuel cells: an experimental study", Journal of power sources, 193(2009), 39-48;

[97] N.Akhtar, S.P.Decent, K.Kendall, "Cell temperature measurements in micro-tubular, single-chamber, solid oxide fuel cells(Mt-SC-SOFCs)", Journal of power sources, 195(2010), 7719-7854;

[98] Loselevich, A.S., Kornyshev A.A, "Phenomenological theory of solid oxide fuel cell anode", Fuel cells, 1(2001), 40-46;

[99] Luca Andreassi, Claudia Toro, Stefano Ubertini, "Modeling carbon monoxide direct oxidation in solid oxide fuel cells", Journal of fuel cell science and technology, 6(2009), 1-15;

`

[100] Y.Xie, X. Xue, "Transient modeling of anode-supported Solid oxide fuel cells", International journal of hydrogen energy, 34(16), 2009, 6882-6891;

[101] M.G. Catherine, G.G. Richard, B.G. Javier, "SOFC anodes for direct oxidation of hydrogen and methane fuels containing H2S", Journal of Power Sources, 179(2008), 317-328;

[102] E.P. Murray, T. Tsai, S.A. Barnett, "A direct-methane fuel cell with a ceria-based anode", Nature, 400(1999), 649-651;

[103] D.M. Bierschenk, J.R. Wilson, S.A. Barnett, "High efficiency electrical energy storage using a methane-oxygen solid oxide cell", Energy & Environmental Science, 3(4), 2011, 944-951;

[104] N.Akhtar, S.P.Decent, K.Kendall, "Numerical modeling of methane-powered micro-tubular, single-chamber solid oxide fuel cell", Journal of power sources, 195(2010), 7796-7807;

[105] E. Vakouftsi, G. Marnellos, C. Athanasiou, F.A. Coutelieris, "A detailed model for transport processes in a methane fed planar SOFC", Chemical Engineering Research & Design, 89(2A), 2011, 224-229;

[106] L. Aguilar, S.W. Zha, Z. Cheng, J. Winnick, M.L. Liu, "A solid oxide fuel cell operating on hydrogen sulfide and sulfur-containing fuels", Journal of Power Sources, 135(2004), 17-24;

[107] D.S.Monder, K.T.Chuang, K.Nandakumar, "A fully coupled multiphysics model for a H_2S SOFC", Journal of The Electrochemical Society, 157(4), 2010, B542-B551;

[108] C.P. Huang, T.R. Ali, "Liquid hydrogen production via hydrogen sulfide methane reformation", Journal of Power Sources, 175(2008), 464-472;

[109] Y. Matsuzaki, I. Yasuda, "Electrochemical oxidation of H_2 and CO in a H_2-H_2O-CO-CO_2 system at the interface of a Ni-YSZ cermet electrode and YSZ electrolyte", Journal of electrochemical society, 147(2000), 1630-1635;

[110] A. Luai, T. Claudia, U. Stefano, "Modeling carbon monoxide direct oxidation in solid oxide fuel cells", Journal of fuel cell science and technology, 6(2009), 1-15;

[111] Daniel J.L.Brett, Alan Atkinson, Nigel P.Brandon, Stephen J.Skinner, "Intermediate temperature solid oxide fuel cells", Chemical Society Reviews, 37(2008), 1568-1578;

[112] Chunshan Song, "Fuel processing for low-temperature and high-temperature fuel cells challenges and opportunities for sustainable development in the 21st century",

`

Catalysis Today, 77(2002), 17-49;

[113] S.Ahmad Hajimolana, M.Azlan Hussain, W.M.Ashri Wan Daud, M.Soroush, A.Shamiri, "Mathematical modeling of solid oxide fuel cells: A review", Renewable and Sustainable Energy Reviews, 15(2011), 1893-1917;

[114] D.A.Noren, M.A.Hoffman, "Clarifying the Butler-Volmer equation and related approximations for calculating activation losses in solid oxide fuel cell models", Journal of Power Sources, 152(2005), 175-181;

[115] J.O.M. Bockris, A.K.N.Reddy, Modern Electrochemistry, vol.2, Plenum Publishing Corporation, New York, 1973;

[116] W.G.Bessler, J.Warnatz, D.G.Goodwin, "The influence of equilibrium potential on the hydrogen oxidation kinetics of SOFC anodes", Solid State Ionics, 177(2007), 3371;

[117] Chen Li, Yixiang Shi, Ningsheng Cai, "Elementary reaction kinetic model of an anode-supported solid oxide fuel cell fueled with syngas", Journal of power sources, 195(2010), 2266-2282;

[118] Ph.Hofmann, K.D.Panopoulos, "Detailed dynamic solid oxide fuel cell modeling for electrochemical impedance spectra simulation", Journal of power sources, 195(2010), 5320-5339;

[119] Wolfgang G. Bessler, Stefan Gewies, Marcel Vogler, “A new framework for physically based modeling of solid oxide fuel cells”, Electrochimica Acta, 53(2007), 1782-1800;

[120] Connor J. Moyer, Neal P.Sullivan, Huayang Zhu, and Robert J.Kee, “Polarization characteristics and chemistry in reversible tubular SOFC operating on mixtures of H2, CO, H2O and CO2”, Journal of the electrochemical society, 158(2), 2011, B117-B131;

[121] W.G. Bessler, "A new computational approach for SOFC impedance from detailed electrochemical reaction-diffusion models", Solid State Ionics, 176(2005), 997;

[122] T. Kim, G. Liu, M. Boaro, S.-I. Lee, J. M. Vohs, R. J. Gorte, O. H. Al-Madhi, B.O.Dabbousi, "A study of carbon formation and prevention in hydrocarbon fueled SOFC", Journal of Power Sources, 155(2006), 231-238;

[123] H. Paradis, M. Andersson, J. Yuan, B. Sunden, "CFD modeling: Different kinetic approaches for internal reforming reactions in an anode-supported SOFC", Journal of Fuel Fell Science and Technology, 8(2011), 1-8;

[124] J. Park, S. Lee, S. Kim, J. Bae, "Numerical analysis of the heat and mass transfer

characteristics in an autothermal methane reformer", Journal of Fuel Fell Science and Technology, 7(2010), 1-7;

[125] N. E. McGuire, N.P. Sullivan, O. Deutschmann, H.Y. Zhu, R.J. Kee, "Dry reforming of methane in a stagnation-flow reactor using Rh supported on strontium-substituted hexaaluminate", Applied Catalysis A: General, 394(2011), 257-265;

[126] V.M.Janardhanan, O.Deutschmann, "CFD analysis of a solid oxide fuel cell with internal reforming coupled interactions of transport, heterogeneous catalysis and electrochemical processes", Journal of Power Sources, 162(2006), 1192-1202;

[127] G.M.Goldin, H.Zhu, R.J.Kee, D.Bierschenk, S.A.Barnett, "Multidimensional flow, thermal, and chemical behavior in solid oxide fuel cell button cells", Journal of Power Sources, 187(2009), 123-135;

[128] N. Laosiripojana, S. Assabumrungrat, "Catalytic steam reforming of methane, methanol, and ethanol over Ni/YSZ: The possible use of these fuels in internal reforming SOFC", Journal of Power Sources, 163(2007), 943-951;

[129] Y. Yang, X. Du, L. Yang, Y. Huang, H. Xian, "Investigation of methane steam reforming in planar porous support of solid oxide fuel cell", Applied Thermal Energineering, 29(2009), 1106-1113;

[130] R. J. Kee, M. E. Coltrin, P. Glarborg, Chemically Reacting Flow. Theory and Practice, John Wiley & Sons, 2003;

[131] Y. Xie, X. Xue, "Modeling of solid oxide electrolysis cell for syngas generation with detailed surface chemistry", Solid State Ionics, 224(2012), 64-73;

[132] G.Hawkes, J.O.Brien, C.Stoots, B.Hawkes, "3D CFD model of a multi-cell high-temperature electrolysis stack", International journal of Hydrogen energy, 34(2009), 4189-4197;

[133] M.Ni, "An electrochemical model for syngas production by co-electrolysis of H2O and CO2", Journal of Power Sources, 197(2011), 1-27;

[134] P.K.Lohsoontorn, J.Bae, "Electrochemical performance of solid oxide electrolysis cell electrodes under high-temperature co-electrolysis of steam and carbon dioxide", Journal of Power Sources, 196(2011), 7161-7168;

[135] S.D.Ebbesen, M.Mogensen, "Electrolysis of carbon dioxide in solid oxide electrolysis cells", Journal of Power Sources, 193(2009), 349-358;

[136] J.Laurencin, D.Kane, G.Delette, J.Deseure, F.Lefebvre-Joud, "Modeling of solid

`

oxide steam electrolyser: Impact of the operating conditions on hydrogen production", Journal of Power Sources, 196(2011), 2080-2093; [Steam-H2 production modeling]

[137] D.Grondin, J.Deseure, P.Ozil, J.P.Chabriat, B.G.Perez, A.Brisse, "Computing approach of cathodic process within solid oxide electrolysis cell: Experiments and continuum model validation", Journal of Power Sources, 196(2011), 9561-9567;

[138] J.S.Herring, J.E.OBrien, C.M.Stoots, G.L.Hawkes, J.J.Hartvigsen, M.Shahnam, "Process in high-temperature electrolysis for hydrogen production using planar SOFC technology", International Journal of Hydrogen Energy, 32(2007), 440-450; [H2 production]

[139] M.Ni, "Computational fluid dynamics modeling of a solid oxide electrolyzer cell for hydrogen production", International Journal of Hydrogen Energy, 34(2009), 7795-7806; [Hydrogen productioin]

[140] M.Ni, "An electrochemical model for syngas production by co-electrolysis of H_2O and CO_2", Journal of Power Sources, 202(2012), 209-216;

[141] M.Ni, "2D thermal modeling of a solid oxide electrolyzer cell(SOEC) for syngas production by H_2O/CO_2 co-electrolysis", International Journal of Hydrogen Energy, 2012, 1-11;

[142] C.J.Moyer, N.P.Sullivan, H.Zhu, R. J.Kee, "Polarization characteristics and chemistry in reversible tubular solid oxide cells operating on mixtures of H2, CO, H2O and CO2", Journal of the Electrochemical Society, 158(2), 2011, B117-B131.